AD_____

Award Number DAMD17-97-1-7079

TITLE: NMR Reconstructive Elasticity Imaging of Breast: Surrogate Remote Palpation Using Quantitative 3-D Displacement and Strain Estimations

PRINCIPAL INVESTIGATOR: Thomas L. Chenevert, Ph.D.

CONTRACTING ORGANIZATION: University of Michigan
                              Ann Arbor, Michigan 48109-1274

REPORT DATE: September 2000

TYPE OF REPORT: FINAL

PREPARED FOR: U.S. Army Medical Research and Materiel Command
                Fort Detrick, Maryland 21702-5012

DISTRIBUTION STATEMENT: Approved for Public Release;
                        Distribution Unlimited

The views, opinions and/or findings contained in this report are those of the author(s) and should not be construed as an official Department of the Army position, policy or decision unless so designated by other documentation.

20010327 046

REPORT DOCUMENTATION PAGE

Public reporting burden for this collection of information is estimated to average 1 hour per response, including the time for reviewing instructions, searching existing data sources, gathering and maintaining the data needed, and completing and reviewing this collection of information. Send comments regarding this burden estimate or any other aspect of this collection of information, including suggestions for reducing this burden to Washington Headquarters Services, Directorate for Information Operations and Reports, 1215 Jefferson Davis Highway, Suite 1204, Arlington, VA 22202-4302, and to the Office of Management and Budget, Paperwork Reduction Project (0704-0188), Washington, DC 20503

1. AGENCY USE ONLY (Leave blank)	2. REPORT DATE September 2000	3. REPORT TYPE AND DATES COVERED Final (11 Aug 97 – 10 Aug 00)

4. TITLE AND SUBTITLE	5. FUNDING NUMBERS
NMR Reconstructive Elasticity Imaging of Breast: Surrogate Remote Palpation Using Quatitative 3-D Displacement and Strain Estimations	DAMD17-97-1-7079

6. AUTHOR(S)
Thomas L. Chenevert, Ph.D.

7. PERFORMING ORGANIZATION NAME(S) AND ADDRESS(ES)	8. PERFORMING ORGANIZATION REPORT NUMBER
University of Michigan Ann Arbor, Michigan 48109-1274 E-MAIL: tlchenev@umich.edu	

9. SPONSORING / MONITORING AGENCY NAME(S) AND ADDRESS(ES)	10. SPONSORING / MONITORING AGENCY REPORT NUMBER
U.S. Army Medical Research and Materiel Command Fort Detrick, Maryland 21702-5012	

11. SUPPLEMENTARY NOTES

12a. DISTRIBUTION / AVAILABILITY STATEMENT	12b. DISTRIBUTION CODE
Approved for public release; distribution unlimited	

13. ABSTRACT (Maximum 200 Words)

The goal of this research program is to develop a sensitive diagnostic technique based on quantitative elasticity imaging permitting surrogate palpation of deep lying breast lesions. The remote measurement of elasticity in breast tissues may provide unique information which could increase detection and/or characterization of potentially malignant masses not accessible to manual palpation. The primary technical objective of this study is to refine and test an MRI method for the acquisition of high resolution 3-dimensional (3D) spatial displacement data through the imaged object for quantitative estimation of internal strain and elastic modulus. Proof-of-concept of the proposed 3D displacement-encoding, stimulated echo technique has been completed and published using two-dimensional test objects. A pneumatically-driven deformation device under acquisition sequence control has been designed, constructed, and demonstrated to produce highly reproducible deformations of the imaged object. The image acquisition sequence has been generalized to encode 3D displacements over a 3D volume using "classic" 3D and fast-spin-echo schemes. Volumetric datasets of 3D phantoms have been acquired and submitted for processing using newly developed 3D elasticity reconstruction algorithms. Comparisons between 2D and 3D elasticity reconstructions from simulated and experimental displacement data shows higher accuracy of the 3D elasticity reconstruction.

14. SUBJECT TERMS		15. NUMBER OF PAGES 66
Breast Cancer; Tissue Elasticity; Magnetic Resonance Imaging; Models		16. PRICE CODE

17. SECURITY CLASSIFICATION OF REPORT	18. SECURITY CLASSIFICATION OF THIS PAGE	19. SECURITY CLASSIFICATION OF ABSTRACT	20. LIMITATION OF ABSTRACT
Unclassified	Unclassified	Unclassified	Unlimited

FOREWORD

Opinions, interpretations, conclusions and recommendations are those of the author and are not necessarily endorsed by the U.S. Army.

NA Where copyrighted material is quoted, permission has been obtained to use such material.

NA Where material from documents designated for limited distribution is quoted, permission has been obtained to use the material.

NA Citations of commercial organizations and trade names in this report do not constitute an official Department of Army endorsement or approval of the products or services of these organizations.

N/A In conducting research using animals, the investigator(s) adhered to the "Guide for the Care and Use of Laboratory Animals," prepared by the Committee on Care and use of Laboratory Animals of the Institute of Laboratory Resources, national Research Council (NIH Publication No. 86-23, Revised 1985).

N/A For the protection of human subjects, the investigator(s) adhered to policies of applicable Federal Law 45 CFR 46.

N/A In conducting research utilizing recombinant DNA technology, the investigator(s) adhered to current guidelines promulgated by the National Institutes of Health.

N/A In the conduct of research utilizing recombinant DNA, the investigator(s) adhered to the NIH Guidelines for Research Involving Recombinant DNA Molecules.

N/A In the conduct of research involving hazardous organisms, the investigator(s) adhered to the CDC-NIH Guide for Biosafety in Microbiological and Biomedical Laboratories.

PI - Signature   Date

APPENDIX:

Publications supported by this grant

1. T.L. Chenevert, A.R. Skovoroda, M. O'Donnell, and S.Y. Emelianov, "Elasticity reconstructive imaging via stimulated echo MRI," Magnetic Resonance in Medicine, 39, pp. 482-490 (1998).

2. Chenevert, TL, Steele, DD, Emelianov, SY and Shovoroda, AR. "Three-Dimensional Static Displacement Stimulated-Echo NMR Strain Imaging". Proceedings of the International Society of Magnetic Resonance in Medicine 1999; 263.

3. Steel, DD and Chenevert, TL, Emelianov, SY, and O'Donnell, M. "Signal-to-Noise Consideration in Static Displacement, Stimulated Echo NMR Elasticity Imaging". Proceedings of the International Society of Magnetic Resonance in Medicine 1999; 1616.

4. A.R. Skovoroda, M.A. Lubinski, S.Y. Emelianov, and M. O'Donnell, "Reconstructive elasticity imaging for large deformations," IEEE Transactions on Ultrasonics, Ferroelectrics, and Frequency Control, 46, pp. 523-535 (1999).

5. Derek D. Steele, Thomas L. Chenevert, Andrei R. Skovoroda and Stanislav Y. Emelianov, "Three-dimensional static displacement, stimulated echo NMR elasticity imaging,". Physics in Medicine and Biology 45 (2000) 1633-1648.

Articles "In Preparation" supported by this grant:

(These can be viewed in PDF format at:
http://bul.eecs.umich.edu/research/emelian/army.html)

A.R. Skovoroda, D.D. Steele, T.L. Chenevert, M. O'Donnell and S.Y. Emelianov, "Three-dimensional reconstructive elasticity imaging using stimulated echo MRI," submitted for publication in the Magnetic Resonance in Medicine (2000).

A.R. Skovoroda, R.Q. Erkamp, S.Y. Emelianov, and M. O'Donnell, "Nonlinear elasticity reconstruction for clearly bounded inhomogeneities," submitted for publication in the IEEE Transactions on Ultrasonics, Ferroelectrics, and Frequency Control (2000).

INTRODUCTION

While manual palpation remains the first diagnostic line of defense against breast cancer[1-4], it is unfortunately limited to relatively large and superficial lesions. The central hypothesis of this work is that remote measurement of elasticity, or hardness, of breast tissues is possible and provides unique information which could increase detection and/or characterization of potentially malignant masses not readily accessible to manual exam. Our preliminary studies suggest that the proposed methods are capable of precisely measuring internal deformation and strain in three dimensions. These data are required to reconstruct the elasticity distribution within the object. Consequently, technologies developed within the scope of this project may have significant diagnostic value for the detection and management of breast cancer.

Most elastography to date has utilized ultrasound [5-14], although recently MRI is gaining considerable interest [15-22]. Usually an external static or dynamic deformation is applied while the resultant displacement or propagating shear wave is documented by imaging devices. In general, to reconstruct the tissue-specific property of Young's modulus in complex systems such as the breast, the 3-D displacement vector must be measured over a 3-D volume. In this project, we are developing techniques that measure the 3-D displacement vector over any volume in the object at high spatial resolution. These data are processed to produce 3-D strain images for submission to a 3D elasticity reconstruction routine to map the relative Young's modulus within the volume.

ACCOMPLISHMENTS IN RELATION TO STATEMENT OF WORK

The goal of this research program is to develop a sensitive diagnostic technique based on quantitative elasticity imaging for eventual surrogate palpation of deep lying breast lesions. To this end, specific technical objectives/tasks were adopted and summarized in the proposal Statement of Work. Each task is restated below along with descriptions of relevant Methods and Progress/Results.

Technical Objective I: Data Acquisition and Reconstruction

Task 1: Month 1-3
Construction of computer controlled hydraulic compression device capable of producing an incremental surface deformation of the mechanical body. This device will be triggered by NMR imaging system and have a simple timing/displacement control appropriate for phantom studies.

The proposed method requires that the imaged object experience a relatively minor externally-applied deformation force. Based on signal optimization simulations, differential deformations below 10% (e.g., <1cm deformation across a 10cm object) should be adequate for generation of elasticity maps. Design details of the mechanical deformation device were provided in Year 1 Progress Report, although are briefly summarized here with the device schematic is shown in Figure 1. Four neoprene bellows outside of the NMR coil (rf-coil) provide both upward and downward force to an acrylic plate on top of the phantom. The top bellows are on a common pressure circuit, likewise the bottom pair are pressurized together to yield uniform vertical displacement along the

top of phantom. Solid acrylic yolks at both ends of the device insure that only the top plate moves in response to pressurization. Pneumatic elements are driven by air-pressure solenoid values that are, in turn, controlled by a transistor-transistor-logic circuit triggered by the NMR imaging sequence.
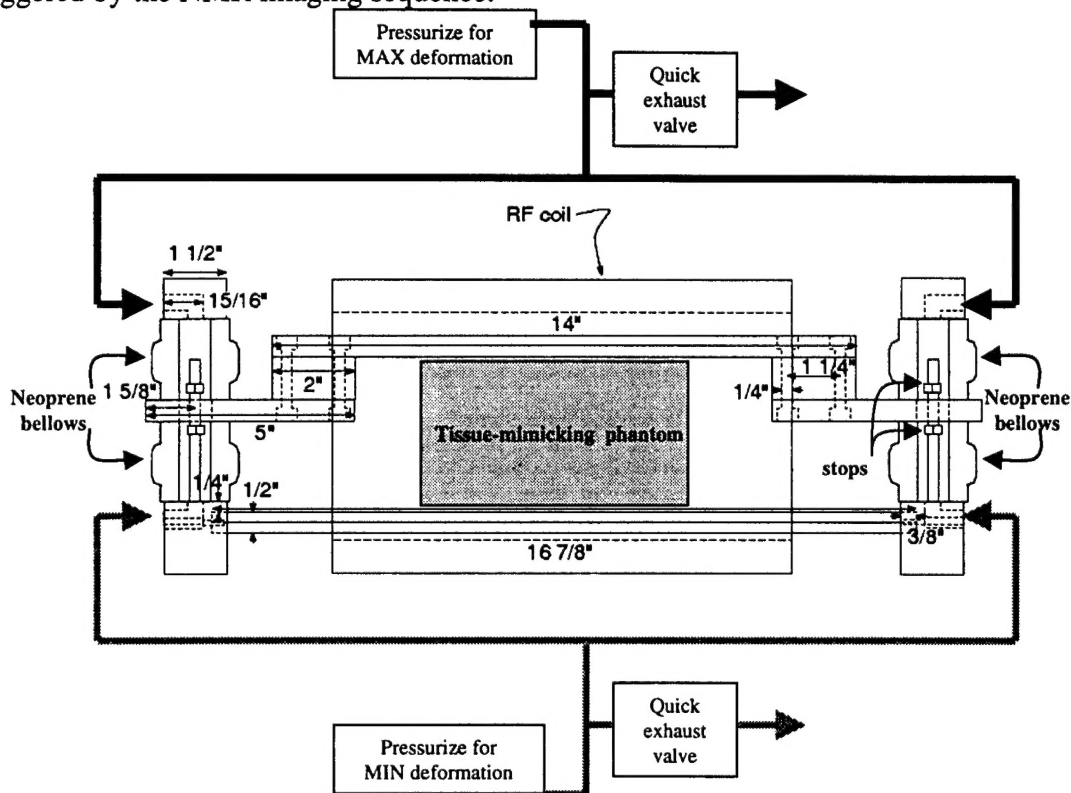

Figure 1. Side-view schematic of pneumatic deformation system.

Phase-encode MRI methods, as employed here, require that data are acquired in many segments over an extended period of time. Consequently the mechanical deformation must be highly reproducible for each segment. Mechanical stability tests of the device were performed using a slightly modified version of the 2D-displacement encoding MRI sequence. The upshot of these tests was that the system is extremely stable and reproducible in application of a 5mm differential deformation (mixing time, TM=350msec). The observed phase instabilities were barely above that allowed by NMR signal limits. These results suggest mechanical reproducibility within <20microns. One significant finding of these stability tests was that the mechanical response of the deformation device was significantly faster (~150ms) than the "settling time" of the tissue-mimicking phantoms (~350ms). That is, internal mechanical reflected waves persist beyond point the acrylic drive plates stop. We anticipate that breast tissue will have comparably long settling times, thus we will continue to use long mixing times (~350ms) in our experiments despite the SNR gains of shorter times. Immunity to long persistence mechanical waves was *the* main motivation to use the stimulated-echo approach as is done here. In addition, we propose a "motion-compensated" version of the sequence that may allow use of shorter mixing times even during residual motion. This concept is described in greater detail in Task 11.

Task 2: Month 1-6
Development of various phantoms to test NMR displacement and strain data acquisition and 3-D elasticity reconstruction algorithms.

Fabrication of phantoms to model the mechanical and NMR properties of human tissue is an important step in development and verification of optimized NMR displacement-encoded volume simulated-echo pulse sequence. Moreover, simple geometries of phantoms allow characterization of the elasticity reconstruction algorithms. The phantom materials should closely resemble relevant tissue properties. In addition, these materials should be stable (i.e. months) and permit the non-destructive embedding of lesion-equivalent targets within the phantom.

We have previously developed tissue-mimicking phantoms to test NMR elasticity imaging device. These phantoms were made of two materials: a) polymer produced by M-F Manufacturing Co., Inc. (Fort Worth, TX), and b) gelatin (Sigma-Aldrich Co., 3050 Spruce Street, St. Louis, MO 63103 USA). The first material, plastisol, consists of a liquid plastic combined with either softener (plasticizer) or hardener. By varying the proportion of these two components, it is possible to produce composite models of desired elasticity. The raw composite materials were stirred and heated to approximately 170°C. At that temperature the mixture was poured into molds producing a tissue-mimicking time-stable phantom of desired shape and elasticity distribution. However, two major deficiencies remain. First, plastisol does not have desired tissue equivalent NMR properties. Second, due to high temperature rise during phantom preparation, it is impossible to produce tissue-containing phantoms using plastisol.

Several different materials were further considered for NMR elasticity phantoms. These materials include Semicosil 921, Semicosil 905 and Silgel 612 (Wacker Silicones Co., Adrian, MI 49221), and Rhodorsil RTV 163 (Rhone-Poulenc, France). From all tested materials, the Semocosil 921 silicone gel appeared to mimic the tissue properties the best. The elasticity of silicone gel can be simply controlled by mixing ratio of two components. The composite material is then poured into the mold and cured at the room temperature enabling fabrication of tissue containing phantoms. These silicone gels have shown high SNR spin-echo signal over the range of hardness variations. In addition, the mechanical properties of silicone did not change over 60 days, as was measured by Instron-type mechanical system. Therefore, it is possible to fabricate tissue-mimicking phantoms of desired shape and elasticity distribution using Semicosil 921 silicone gel.

Based on favorable NMR and mechanical properties, phantoms were fabricated using the Semicosil materials. These phantoms were designed with simple geometries to assess spatial resolution and accuracy of 3D strain imaging 3D elasticity reconstruction algorithms, and include crossed bars of hard material (6x Young's modulus) with variable size and separation (for resolution) and simple spherical inclusions for comparison with theoretical results.

Task 3: Month 1-12
Development of the NMR displacement-encoded, volume stimulated-echo pulse sequence optimized for displacement/strain sensitivity and SNR.

Two, 3D displacement-encode, volume stimulated-echo pulse sequences have been developed. These are shown in Figure 2(a) using "classic" 3D spatial encoding, and (b) a fast-spin-echo (FSE) extension to more efficiently encode the 3rd dimension. The

classic 3D sequence, is simplest and implement but unfortunately it is clinically impractical due to very long scantimes. Incorporation of the FSE echo train permits a scantime reduction by a factor of 1/4, 1/8, to 1/16 dependent on echo train length. To date, we have implemented an 8-echo FSE sequence where the FSE phase-encoding is applied along the 3rd dimension (i.e. slice direction). Ideally, all slice encode steps are acquired in one-shot which greatly reduces scan time (to 13min). Unfortunately, it appears that poor gradient hardware performance is introducing eddy current effects that confound 3rd axis encoding on our 2T MRI system. Phase shifts from this artifact derail strain measurement based on phase. We are in the process of evaluating means to apply phase corrections to reduce imperfections in the FSE component of the sequence.
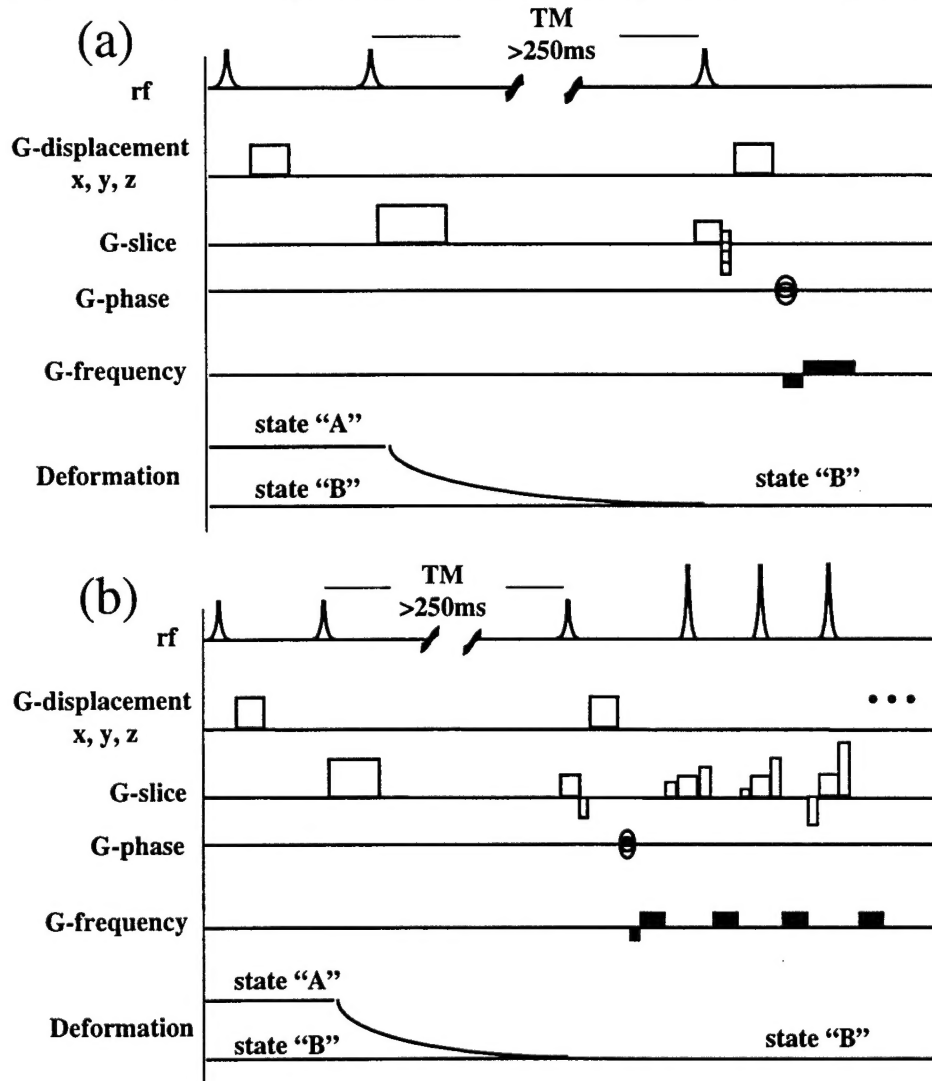
Figure 2. Volumetric displacement-encoding stimulated echo sequences using (a) classic 3D encoding and (b) fast-spin-echo encoding of the third dimension.
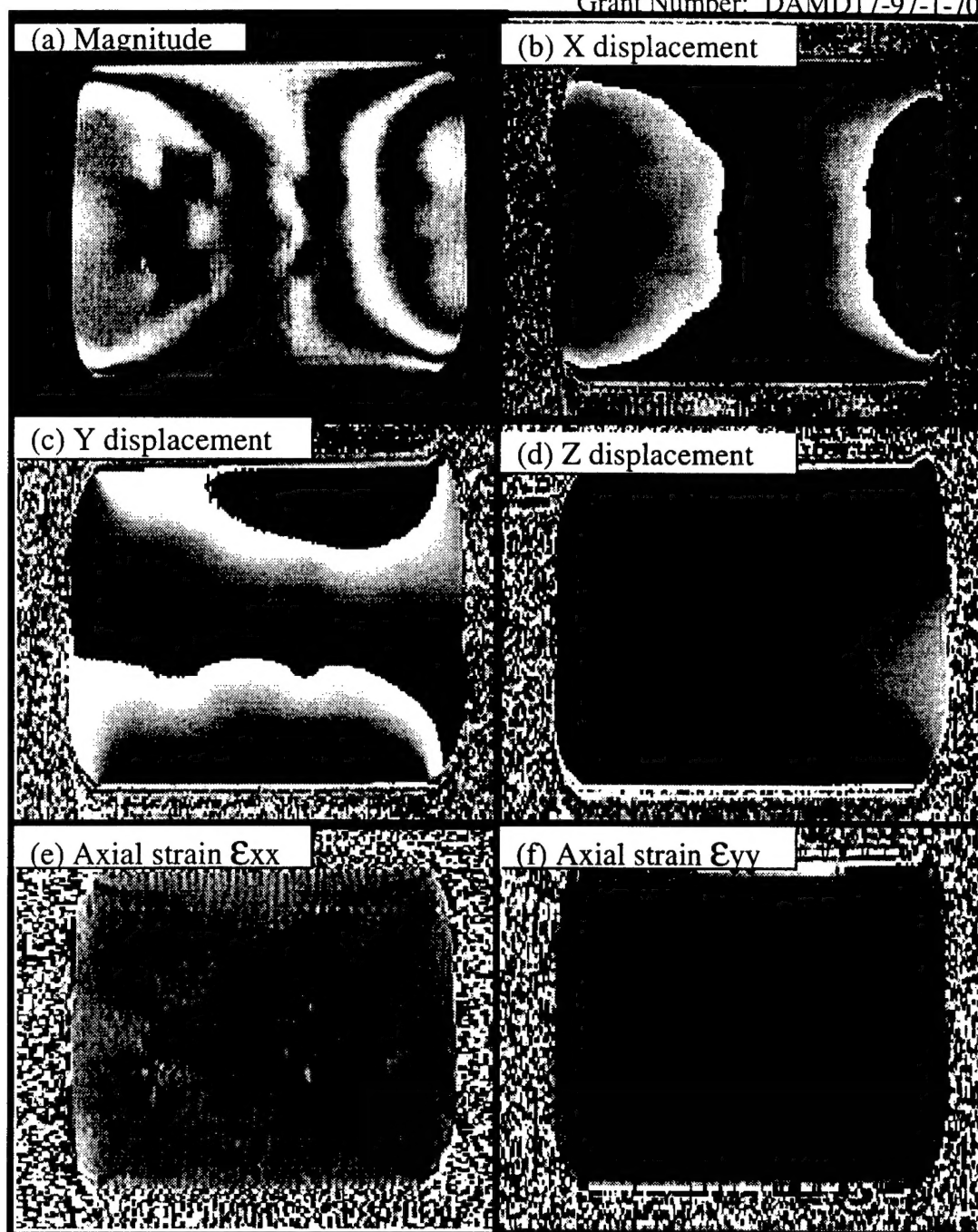
Figure 3. Volumetric displacement-encoding stimulated echo sequence applied to Semicosil rubber phantom containing crossed ramped bars of hard material. Shown are (a) magnitude image, displacement images in (b) X right-to-left, (c) Y top-to-bottom, and (d) Z through-plane. Strain images (i.e. spatial derivative of displacement) for X and Y displacements are shown in (e) and (f) respectively.

Images of tissue mimicking phantom containing ramped bars of harder material acquired via the 3D FSE stimulated echo sequence are shown in Figure 3. Spurious intensity modulations in the magnitude image (i.e. conventional MR image) in Figure 3(a) indicate an imperfect reconstruction along the 3rd dimension. That is, there is an interference of signal from adjacent slices. Despite this, derivative displacement and strain images display features of the object (Figure 3(b-f)), however, residual phase error prevent

acceptable elasticity reconstructions. Deformation and object symmetry meant the displacement and strain in the 3rd dimension (ie. perpendicular to the image) was small.

Computer simulations were performed to address the tradeoff between displacement sensitivity and NMR signal-to-noise (SNR) since optimization of one parameter comes at the expense of another. Key parameters that affect SNR and displacement sensitivity include: displacement gradient amplitude and duration; applied deformation amplitude; image resolution; mixing time, TM; and tissue water diffusion properties. Results of the optimization studies suggest greater SNR can be achieved through greater surface strain (i.e. deformation of the object by ~10%) with a corresponding reduction in displacement encoding (reduced from 4 to 1 gauss/cm). Increasing the applied deformation will have the added benefit to make the applied deformation more significant relative to background motions such as cardiac and respiratory. Yet higher deformation, however, introduce the need to consider non-linear elastic effects (see Task 5).

Task 4: Month 1-12
Expansion of previously developed linear elasticity reconstruction algorithms for volumetric displacement and strain NMR measurements.

Expansion of linear elasticity reconstruction algorithms were focused on the following two aspects: a) development of boundary detection methods to identify the regions of uniform elasticity (Young's modulus) distribution, and b) development of volumetric linear elasticity reconstruction algorithms for optimized NMR displacement-encoded, volume simulated-echo pulse sequence.

The boundary detection algorithm was developed for specifically NMR elasticity imaging. This algorithm is based on the stress continuity condition applicable for soft tissue deformations used in these studies. The relevant boundary definition methods were detailed in the Year 1 Progress Report.

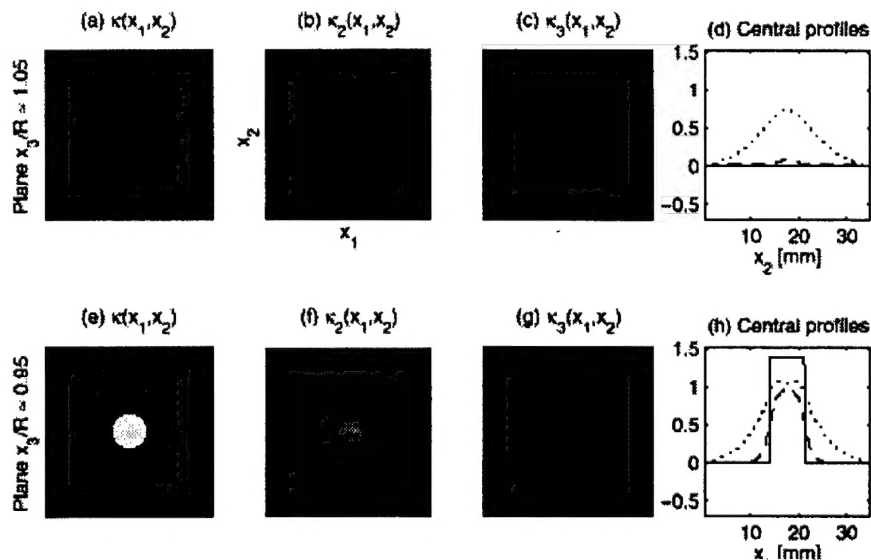The following relates to extensions to a 3D elasticity reconstruction algorithm

Figure 4. Simulated elasticity maps at planes just outside of (top row) and just within of (bottom row) a spherical hard inclusion. The 3D reconstruction, k3, (images on right) was a more faithful depiction of truth, k, (images on left), relative to the 2D reconstruction, k2, (images in middle).

wherein complete three-dimensional strain data are required to solve for a general, three-dimensional object. Previously, only 2D reconstruction algorithms have been applied, yet these are anticipated to lead to errors at planes where through-plane strain is significant. As an illustration, Figure 4 shows *simulated* elasticity distributions at a slice just within (z=0.95 radius) and just outside (z=1.05 radius) of a hard spherical inclusion. These data were used to test the 3D elasticity reconstruction algorithm and provide supportive evidence for the need of 3D reconstruction algorithms in general.

Task 5: Month 10-26
Development of the nonlinear elasticity reconstruction model capable to process high-strain NMR images.

Large external deformations increase the signal to noise ratio (SNR) of displacement and strain images. Unfortunately, large deformations of soft tissue and tissue-like materials cannot be described with a linear elastic model. A linear model can break down in two ways. First, for most soft tissues, the elastic modulus increases as a function of strain (i.e., strain hardening). This effect is often referred to as "material nonlinearity." Second, a more complete description of the equilibrium equation, including non-linear strain-displacement relations, must be used for large deformations. This effect is often referred to as "geometric nonlinearity." Due to the high order displacement derivatives resulting from this description, error propagation must be minimized in any reconstruction algorithm using measured displacement data with a finite signal to noise ratio.

First, we examined the geometric nonlinearities arising from large amplitude deformations. This is demonstrated on the rubber-based phantom with a single, hard spherical inclusion (see Figure 5). In general, the nonlinear relation between the strain tensor and the displacement vector, i.e. the expressions for the nonlinear Lagrangian strain tensor components are

$$\varepsilon_{ij} = \frac{1}{2}(u_{i},_{j}+u_{j},_{i}+u_{k},_{i}\,u_{k},_{j})\,,\quad i,j = 1,2,3\,,$$

and do not depend on mechanical properties of the object. In this equation and the rest of this report, the lower index after a comma means differentiation with respect to the corresponding spatial Lagrangian coordinate. In linear case, i.e., for small deformations, the last term in above equation is small and can be ignored. The linear and nonlinear shear components of the strain tensor are presented in Figure 5. Note that these studies were conducted on phantom with almost no material nonlinearities over the deformation range applied (average strain up to 15%). The specific purpose of the present study was to explore numerical methods minimizing the effects of higher order displacement derivatives needed to describe finite amplitude deformations on elasticity reconstruction.
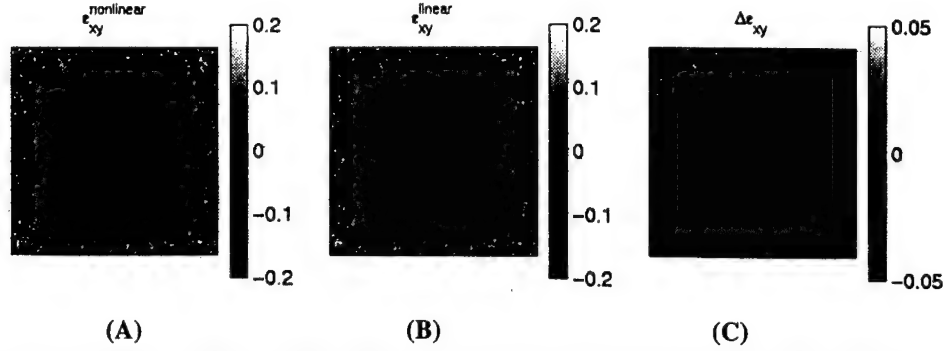
Figure 5: Nonlinear shear component (A) of the strain tensor is contrasted with the same component computed using linear model (B), i.e., under small deformation assumption. The difference can reach almost 25% of the dynamic range as indicated in image (C).

Previous algorithms for elasticity reconstruction were formulated using the set of equations describing mechanical equilibrium in a statically deformed, linear elastic medium. Independent of the specific elastic model, however, these equations can be posed in either differential or integral form. An integral representation is more appropriate for a nonlinear model given realistic measurement noise. Numerical methods have been developed for both linear and nonlinear models exploiting an integral representation of the reconstruction equations. Both plane strain state approach to approximate two-dimensional displacement and full three-dimensional formulation were considered.

Second, the nonlinear form of equilibrium equations using the nonlinear strain-displacement and stress-strain relationships were studied. Briefly, the most general nonlinear mechanical equilibrium equations for a three-dimensional (3-D) volume V of deformed media with the displacement vector $U=U(x_1,x_2,x_3)=(u_1,u_2,u_3)$ in Cartesian coordinates $X=X(x_1, x_2, x_3)$ are

$$\sum_{j=1}^{3}\{\sum_{n=1}^{3}[\sigma_{nj}(\delta_{in}+u_{i},_n)]\},_j = 0, \ i=1,2,3 \ .$$

Here σ_{nj} is a component of the 2nd ranked stress tensor and δ_{in} is the Kronecker delta symbol. This equation must be satisfied at every internal point of the body. If the magnitudes of the spatial derivatives of all displacement components are small, the last terms $u_i,_n$ can be omitted, producing the familiar linear equilibrium equations:

$$\sum_{j=1}^{3}\sigma_{ij},_j = 0, \ i=1,2,3 \ .$$

To complete the system of equations describing internal deformations, the relation between stress and strain tensors, as well as the relation between the strain tensor and the displacement vector, are needed. Here we will assume that the standard linear relation between the stress tensor σ_{ij} and the strain tensor ε_{ij} for incompressible media is still valid

$$\sigma_{ij} = p\delta_{ij} + 2\mu\varepsilon_{ij} \ ,$$

where p is the static, internal pressure and the shear elastic modulus μ is considered a constant independent of the strain magnitude. Computing the spatial distribution of the shear elastic modulus is the goal of reconstruction. Note in an incompressible material

Page9

such as soft tissue the shear and Young's moduli are simply proportional (i.e., $E = \mu/3$). Thus, shear modulus and Young's modulus reconstructions are equivalent.

For a general three-dimensional strain state described by nonlinear equilibrium equation and stress-strain relationship for incompressible material, the following system of equations can be obtained:

$$A\nabla(p) = -pB - F,$$

where

$$A(x,y) = \begin{pmatrix} 1+u_{1,1} & u_{1,2} & u_{1,3} \\ u_{2,1} & 1+u_{2,2} & u_{2,3} \\ u_{3,1} & u_{3,2} & 1+u_{3,3} \end{pmatrix}, \quad B(x,y) = (b_i) = \nabla^2 U,$$

$$F = (f_i) = 2\{A\Psi + \mu[\sum_{i=1}^{3} \varepsilon_{ii} U_{,ii} + \sum_{i,j=1}^{3} (1-\delta_{ij})\varepsilon_{ij} U_{,ij}]\},$$

$$\Psi = (\psi_i) = (\mu\varepsilon_{1i})_{,1} + (\mu\varepsilon_{2i})_{,2} + (\mu\varepsilon_{3i})_{,3}, \quad i=1,2,3;$$

$$\nabla = (\partial/\partial x_1, \partial/\partial x_2, \partial/\partial x_3), \quad \nabla^2 = \partial^2/\partial x_1^2 + \partial^2/\partial x_2^2 + \partial^2/\partial x_3^2;$$

Note that the nonlinear form of the strain tensor must be used here.

To solve this equation with respect to unknowns $\partial p/\partial x_1$, $\partial p/\partial x_2$, and $\partial p/\partial x_3$ we first compute the determinant of matrix A, which is

$$\det(A) = 1 + DivU + \det\begin{pmatrix} u_{,x} & u_{,y} \\ v_{,x} & v_{,y} \end{pmatrix} + \det\begin{pmatrix} v_{,y} & v_{,z} \\ w_{,y} & w_{,z} \end{pmatrix} + \det\begin{pmatrix} u_{,x} & u_{,z} \\ w_{,x} & w_{,z} \end{pmatrix} + \det\begin{pmatrix} u_{,x} & u_{,y} & u_{,z} \\ v_{,x} & v_{,y} & v_{,z} \\ w_{,x} & w_{,y} & w_{,z} \end{pmatrix} = \sqrt{g},$$

where $g = \det(g_{ij})$ is the determinant of the 2nd ranked metric tensor g_{ij}.

Note that for incompressible materials $g = 1$, and $\det(A) = 1$, which greatly simplifies the inversion of (A1):

$$\nabla(p) = \alpha p + \beta,$$

where $\alpha(x,y) = (\alpha_i) = -A^{-1}B$, $\beta(x,y) = (\beta_i) = -A^{-1}F$, $i=1,2,3$.

By integrating each component equation of this equation along its corresponding coordinate, we obtain:

$$p(x_1,x_2 x_3) = \varphi_1 p(x_1^0, x_2 x_3) + F_1 = \varphi_2 p(x_1, x_2^0, x_3) + F_2 = \varphi_3 p(x_1, x_2, x_3^0) + F_3$$

where

$$\varphi_i(x_1,x_2,x_3) = \exp[\int_{x_i^0}^{x_i} \alpha_i(x_1,x_2,x_3)dx_i], \quad F_i(x_1,x_2,x_3) = (\int_{x_i^0}^{x_i} \frac{\beta_i}{\varphi_i}dx_i)\varphi_i, \quad i=1,2,3.$$

Combining all of these equations, the three-dimensional case reduces to:

$$[(\varphi_2\varphi_3|_{x_2^0} + \varphi_3\varphi_2|_{x_3^0})p_0 + (\varphi_2 F_3|_{x_2^0} + \varphi_3 F_2|_{x_3^0}) + (F_2 + F_3)]|_{x_1^0}\varphi_1 + 2F_1 =$$

$$[(\varphi_1\varphi_3|_{x_1^0} + \varphi_3\varphi_1|_{x_3^0})p_0 + (\varphi_1 F_3|_{x_1^0} + \varphi_3 F_1|_{x_3^0}) + (F_1 + F_3)]|_{x_2^0}\varphi_2 + 2F_2 =$$

$$[(\varphi_1\varphi_2|_{x_1^0} + \varphi_2\varphi_1|_{x_2^0})p_0 + (\varphi_1 F_2|_{x_1^0} + \varphi_2 F_1|_{x_2^0}) + (F_1 + F_2)]|_{x_3^0}\varphi_3 + 2F_3,$$

where $p_0 = p(x_1^0, x_2^0, x_3^0)$.

The caveat here is that last equation does not contain high order spatial displacement derivatives, compared with equivalent differential equation, and therefore, elasticity reconstruction should be more stable. Again, this equation shows that spatial derivatives of all displacement components are needed in general for elasticity reconstruction in both linear and nonlinear cases, but any one of the three displacement components can be reconstructed using incompressibility processing based on the relation ($\det(A) = 1$).

Technical Objective II: Phantom Studies on 2T 18cm Bore MRI System

Task 6: Month 7-22
Development of gel- and rubber-based phantoms with tissue mimicking elastic properties. Time stable phantoms with non-palpable inclusions of various shapes and elasticity contrast positioned at different locations within the phantom will be produced.

During the first year of the project, we have identified and tested the materials for tissue mimicking phantoms. Our ultimate goal is to simulate the anatomical and geometrical features of the normal and pathologically transformed breast using these materials. The models of breast containing single or multiple inclusions were fabricated using plastisol material (M-F Manufacturing Co., Fort Worth, Texas, USA).

Our studies, however, suggest that silicone gels better simulate the mechanical and NMR relaxation properties of the tissue. Initially, silicone-gel based homogeneous phantoms were produced for mechanical and NMR testing (Semicosil 921, Wacker Silicones Co., Adrian, Michigan, USA). These tests showed the material had suitable NMR properties - like tissue. To control mechanical properties, the Semicosil 921 contains two components, A and B, wherein different ratios of these components are used to vary the mechanical properties of the gel. A tissue-mimicking phantom was constructed in several steps. First, background material was prepared by thoroughly mixing components A and B in a 1:1 ratio, and then pouring the mixture into a 154-mm by 80-mm rectangular mold. The mixture was degassed and cured for 24 hours at room temperature to produce a 22-mm thick layer. Then a 25-mm diameter hard sphere was prepared from a 1:2.5 mixture of A and B and was placed on top of the layer in the middle of the mold. Finally, another batch of background material (1:1 ratio) was poured into the mold resulting in a 64-mm by 80-mm by 154-mm phantom with a single, hard, spherical inclusion roughly in the center. At the same time, three samples of each batch were taken to independently assess the elasticity contrast between the inclusion and surrounding materials. These measurements were performed using the force-deformation system which showed that the inclusion was four times harder than the background, and that both background materials were elastically equivalent. These are highly stable and are still in use several months post-fabrication.

Task 7: Month 12-26
Investigation of the capabilities of 3-D NMR elasticity imaging, i.e., determine sensitivity, accuracy and resolution of NMR displacement and strain images, and reconstructed elasticity (Young's modulus) distribution.

As shown by *simulation* presented in Figure 4, elasticity maps reconstructed from 3-D strain data should be more accurate than a 2-D elasticity reconstructions. This should be particularly true near the edges of an object where the plane-strain-state is violated; that is where the strain along the "through-plane" direction in non-negligible. This concept was tested on silicone-gel based phantoms developed in Task 6 using the volume stimulated-echo pulse sequence (Task 3). A comparison of the *actual experimental* "2D" reconstruction and "3D" reconstructed elasticity maps for 2 of 32 planes through the
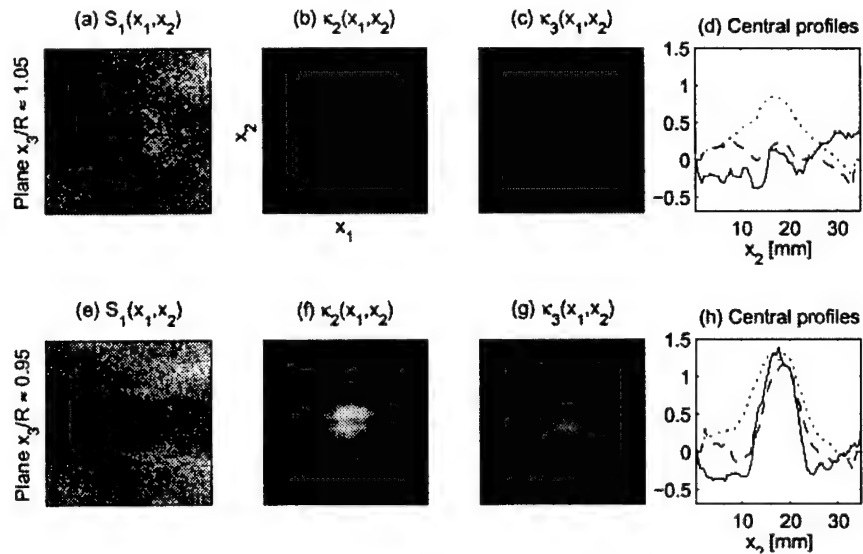

Figure 6. Reconstructed elasticity maps at planes just outside of (top row) and just within (bottom row) a spherical hard inclusion in a silicone-gel phantom. These results are consistent with the simulations (Figure 4) that show the 3D reconstruction, k3, (images on right) more faithfully depicts the size of the inclusion.

phantom data are shown in Figure 6. The planes selected through the phantom and general format of Figure 6 were chosen for direct comparison between the simulation (Figure 4) and experiment (Figure 6). Ideally, there would be no inclusion visible in the plane outside of the inclusion (ie. reconstructions in the top row of Figure 6 should be uniform). Violation of the non-negligible strain remote from the object, however, results in inaccuracies in 2D reconstructions. These errors are clearly reduced in the 3D reconstruction which confirms simulation results.

Technical Objective III: Translation to 1.5T Human MRI System
Task 8: Month 20-25
Design and construction of the compression device compatible with human breast NMR imaging system and capable to produce wide range of surface deformations. Development of sophisticated circuits to control surface deformations and time synchronization with human MRI system.

Translation to the 1.5T unit system has begun. We have a compressor pneumatic-drive system and constructed the deformation device suitable for operation on our 1.5T human MRI unit. Existing phantoms are used for testing on the 1.5T unit.

Task 9: Month 24-34
Development of appropriate for clinical studies 3-D displacement encoded, volume stimulated-echo pulse sequence on human MRI system with data acquisition time within or comparable to regular MRI examination.

Two- and three-dimensional fast-spin-echo (FSE) are still being modified for displacement-sensitive, stimulated-echo acquisitions. These sequences are inherently more complex on the clinical MRI system, and as such are requiring more time to debug. Nevertheless, these sequences will be completed outside of the funded project period.

Task 10: Month 22-34
Development of time efficient elasticity reconstruction algorithms more suitable for clinical applications.

Since the reconstruction is a numerical solution to invert high-order differential equations, reconstruction time scales with the acquired quantity of slices and the in-plane resolution. Previously, volumetric datasets, as generated in this project did not exist, thus not all practical issues related to 3D elasticity reconstruction were known. To date, most programming efforts have been directed to management of the acquired six-dimensional datasets (i.e. position in x,y,z, and displacement-sensitive u_x,u_y,u_z) which expand to and a "12-vector" per pixel (position, and 9-elements of the strain tensor). The 12-dimensional data is only the *input* to the reconstruction.

Both ultrasound and NMR imaging systems can be used for reconstructive elasticity imaging. Relative to ultrasound, NMR has the advantage in overall resolution and accuracy for three-dimensional motion estimation. This, in turn, does not constrain the mathematical models used for elasticity reconstruction. Elasticity imaging with NMR is therefore, volumetric if all components of the displacement and strain are measured.

The reconstruction of the unknown spatial distribution of shear elastic modulus in a region of interest (ROI) of three-dimensional volume V in Cartesian coordinates x_i, $i = 1,2,3$ under the assumption of linear elastic model can be written in following set of differential equations

$$(\mu\varepsilon_{12})_{,11}-(\mu\varepsilon_{12})_{,22}+[\mu(\varepsilon_{22}-\varepsilon_{11})]_{,12}+(\mu\varepsilon_{23})_{,13}-(\mu\varepsilon_{13})_{,23}=0,$$

$$(\mu\varepsilon_{13})_{,11}-(\mu\varepsilon_{13})_{,33}+[\mu(\varepsilon_{33}-\varepsilon_{11})]_{,13}+(\mu\varepsilon_{23})_{,12}-(\mu\varepsilon_{12})_{,23}=0,$$

$$(\mu\varepsilon_{23})_{,22}-(\mu\varepsilon_{23})_{,33}+[\mu(\varepsilon_{33}-\varepsilon_{22})]_{,23}+(\mu\varepsilon_{13})_{,12}-(\mu\varepsilon_{12})_{,13}=0.$$

Computing the spatial, 3-D distribution of the shear elastic modulus $\mu(X)$ is the goal of elasticity reconstruction.

Due to the finite noise in measured internal displacement fields, the computationally more stable integral-based approach to shear modulus reconstruction is used, where corresponding integral equations could be used to reconstruct spatial distribution of unknown shear modulus $\mu(X) = \mu(x_1, x_2, x_3)$ instead of partial differential equations. For example, the first equation can be written in integral form as follows

$$\delta(x_1, x_2, x_3) \equiv \mu(\varepsilon_{22} - \varepsilon_{11}) - [\mu(\varepsilon_{22} - \varepsilon_{11})]\big|_{x_1^0} -$$

$$[\mu(\varepsilon_{22} - \varepsilon_{11})]\big|_{x_2^0} + [\mu(\varepsilon_{22} - \varepsilon_{11})]\big|_{x_1^0, x_2^0} +$$

$$\int_{x_2^0}^{x_2} (G_{12}^2 - G_{12}^2\big|_{x_1^0}) dx_2 - \int_{x_1^0}^{x_1} (G_{12}^1 - G_{12}^1\big|_{x_2^0}) dx_1 = 0 ,$$

where

$$G_{12}^1 = (\mu\varepsilon_{12})_{,2} + (\mu\varepsilon_{13})_{,3}, \ \ G_{12}^2 = (\mu\varepsilon_{12})_{,1} + (\mu\varepsilon_{23})_{,3} .$$

The simplest and computationally least expensive way to solve this set of equations is to reduce any of those equations to the in-plane form, where only in-plane distribution of shear or Young's modulus is unknown at a time. It is possible, for example, if for any region $x_3 < x_3^0$ the distribution of shear modulus can be assumed as known. In this case last two terms in the first equation at the crossection $x_3 = x_3^0$ can be replaced by their finite-differences analogs and final equation for in-plane shear modulus distribution $\mu(x_1, x_2) = \mu(x_1, x_2, x_3^0)$ will be hyperbolic. Such numerical procedure will be absolutely stable for any ratio of grid steps H / h_i, $i = 1,2$ where $H = h_3$. Therefore, reconstructing volumetric elasticity distribution can be performed on a plane-by-plane basis. Note that the discretization step H in x_3 direction can be different from plane to plane.

A typical result of elasticity reconstruction is presented in Figure 7. The experiments were performed on the rubber-based block shaped phantom with a single, hard spherical inclusion located approximately in the middle of the phantom. In Figure 7, the elasticity distribution within planes crossing the center of the sphere (i.e., R=0) and the side of the sphere (x_3 = ¾ R_0) are presented in Figure 8. Also, 2-D and 3-D based reconstructions are contrasted. As expected, the 2-D and 3-D reconstructions are very similar for the central plane of the phantom, where out-of-plane strains are small. However, the 3-D reconstruction at the edge of the inclusion is far more accurate compared to 2-D model. The profile of the elasticity reconstruction throughout the longitudinal axis is presented in Figure 9, where again 2-D and 3-D results are contrasted. Clearly, 3-D reconstruction is required for accurate volumetric elasticity imaging.
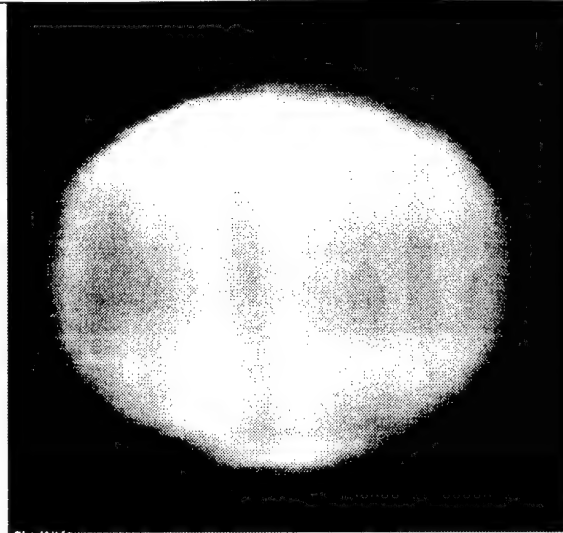
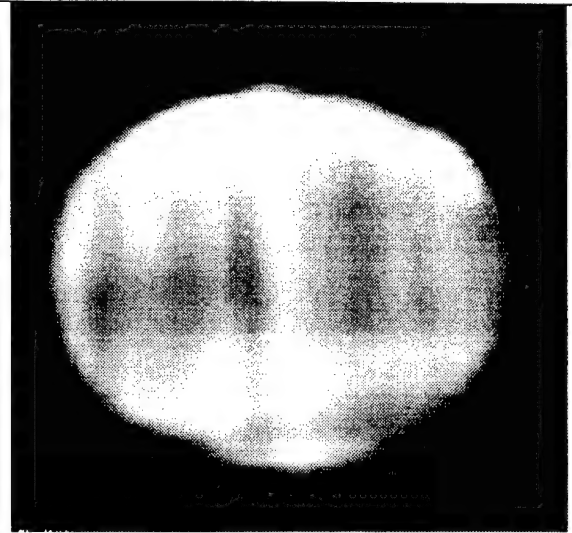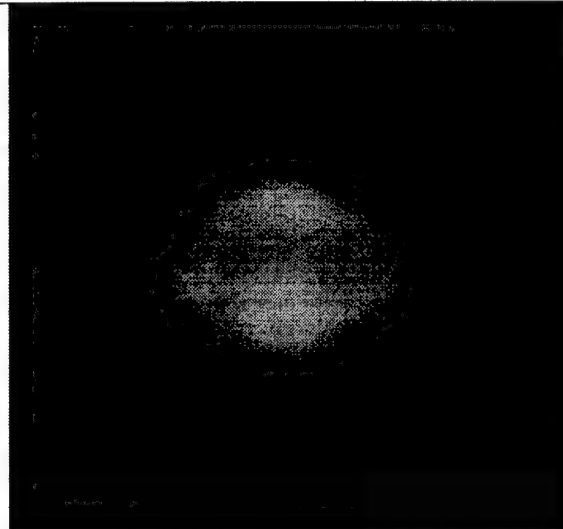| Figure 7 (A): 2-D elasticity reconstruction in the central plane of the phantom and inclusion | Figure 7 (B): 3-D Elasticity reconstruction in the central plane of the phantom and inclusion. |

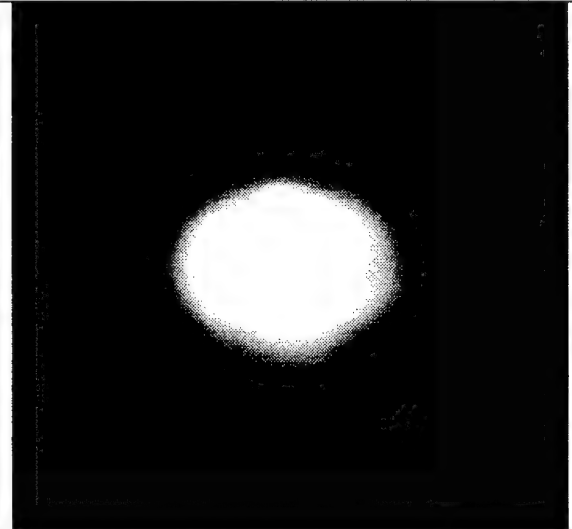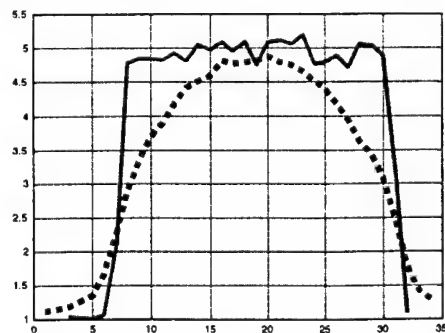| Figure 8(A): 2-D elasticity reconstruction in the plane ¾ of radius away from the inclusion center. | Figure 8 (B): 3-D elasticity reconstruction in the plane ¾ of radius away from the inclusion center. |

Figure 9: Longitudinal elasticity profile of inclusion using 2-D (dotted) and 3-D models (solid). Greater accuracy of the 3-D over the 2-D reconstruction is apparent.

Task 11: Month 20-30
Estimate the influence of the cardiac and respiratory motion to elasticity images and develop the approaches to reduce these artifacts.

The model used for reconstructing the elastic modulus of the imaged area assumes that the displacement measured is a static one. That is, that there is no residual internal motion of the object while the displacement encoding is taking place—it is either in a compressed or relaxed state. To date, all of our formalism assumed the object is static before and after displacement during position encoding pulses. Irreproducible mechanical ring-down of the deformation system, as well as extraneous physiologic motions however, will cause phase errors. Given this eventuality, formalism related to the displacement-encoding was generalized to include position, velocity, acceleration and all other higher-order terms. Mathematically, the encoded phase is expressed as:

$$\phi = \gamma \int_0^\tau G_d(t) \cdot r(t) = \gamma \int_0^\tau G_d(t) \cdot \left[r_0 + vt + \frac{1}{2}at^2 + \dots \right],$$

where phase (ϕ), the information accessed with the imaging sequence, depends on the absolute position of the object (r_0), its velocity (v), its acceleration (a) and ultimately all aspects of the object's internal motion. So, if the object is actually moving slightly during the experiment and we have data that contain information about this motion, the following question arises: if we use this data with a reconstruction that assumes no internal motion, what is the resulting error? Additionally, if we can reduce sensitivity to internal motions, can we improve the signal-to-noise ratio (SNR) of the map of the elastic modulus?

Because the encoding gradient waveform ($G_d(t)$) is controllable in the experiments, one is able to reduce or enhance sensitivity to different aspects of the imaged object's motion. To test if these questions would be of concern at all, we developed an encoding waveform to provide a phase image that is independent of velocity, but was otherwise essentially identical to the waveforms used in the past (in other words, the phase depended on all aspects of the object's motion). By comparing the phase obtained with the new waveform and that obtained with the old waveform, one can see if the internal velocity of the object contributes to the encoded phase in a significant way.
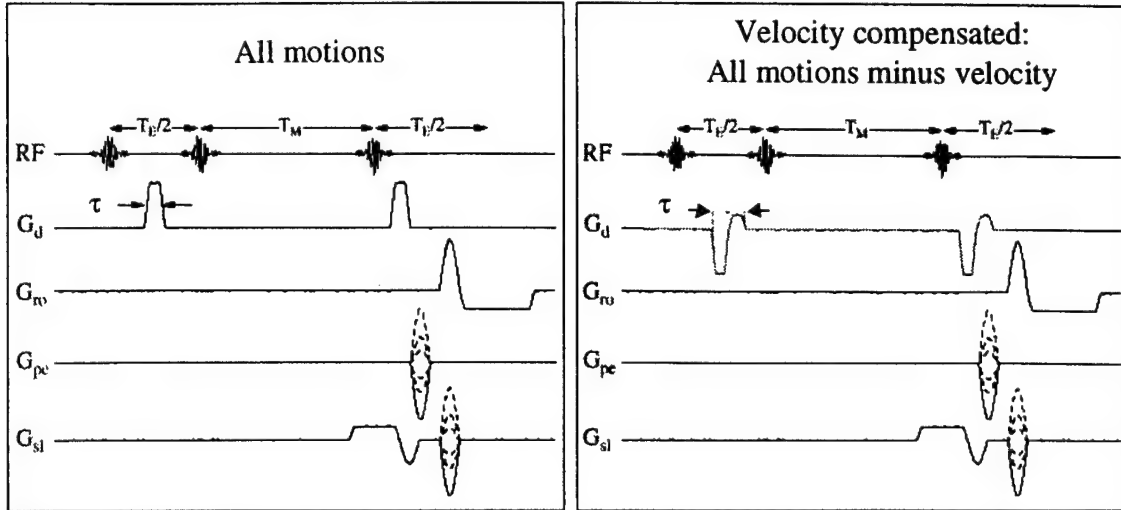
Figure 10: The original sequence (on left) is sensitive to all motions; the "velocity-compensated" displacement sensitive sequence (on the right) eliminates phase shift due to constant velocity motion during application of Gd.

Figure 11 shows the phase images resulting from both the old (velocity sensitive) and the new (velocity insensitive) encoding waveforms, as well as the average difference between them for two different mechanical transition times. The first transition time ($T_M = 270ms$) is that used in previous experiments, while the second ($T_M = 50ms$) is a transition in which we know that the object was still moving during the phase encoding process. These results point to several things. First, that the 270ms transition time is sufficiently long to allow internal motions to die out. Thus, elasticity maps obtained from data with this transition time should be reasonable. Secondly, we can shorten the mechanical transition period at least until the two waveforms provide different results, improving the SNR of the collected data and the reconstruction. Thirdly, it may be possible to shorten this transition more by using appropriate encoding waveforms, increasing the SNR and the sensitivity of this method to elasticity variations even further
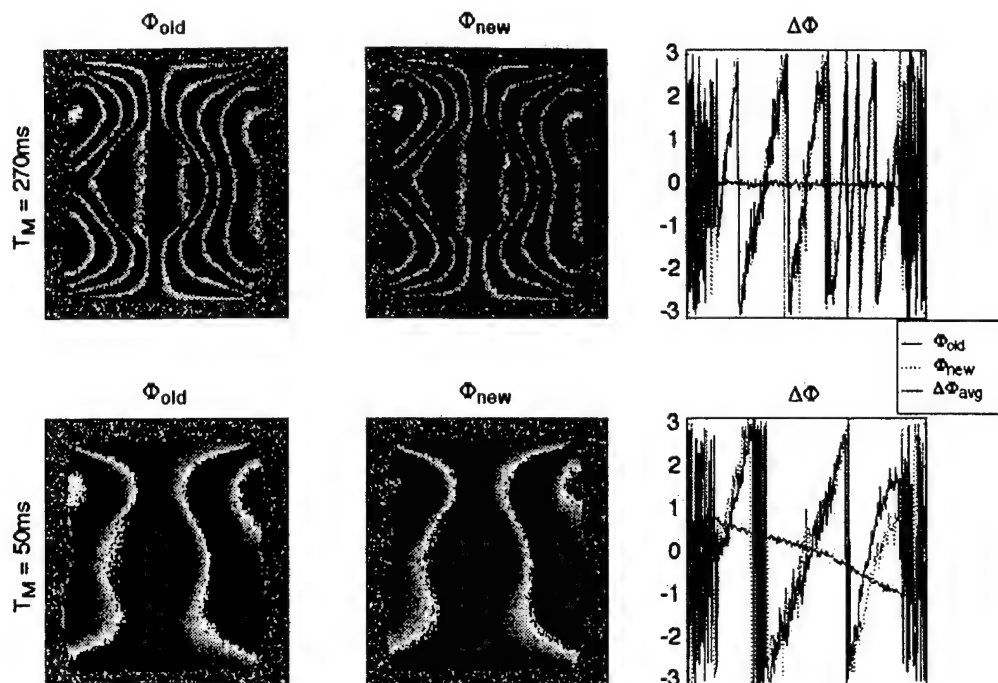
Figure 11: Comparison of original and velocity-compensated sequences on a phantom at short mixing time, TM=50ms (i.e. where residual velocity is present), and long mixing time TM=270ms (where residual motion is negligible. The non-zero phase difference between the two suggests that velocity phase contribution can be isolated, and thus be compensated.

Task 12: Month 30-36
Validation of clinical NMR data acquisition and elasticity reconstruction methods on breast tissue mimicking phantoms.
This task is still incomplete. Two- and three-dimensional fast-spin-echo (FSE) are being modified for displacement-sensitive, stimulated-echo acquisitions. These sequences are inherently more complex on the clinical MRI system, and as such are requiring more time to debug than originally anticipated. Nevertheless, these sequences will be completed outside of the funded project period.

CONCLUSIONS
Tasks to design, fabricate and refine the "deformation devices", essential for phantom studies, are complete. The MRI-compatible hardware, pneumatic components, and control circuitry are now fully operational. This device provides excellent control and stability in repetitive deformations of an tissue-mimicking objects. Significant effort was directed to develop suitable phantom materials. Requirements include: temporally stable (over months-years); adjustable mechanical properties to match a range of tissues; moldable to simple geometries; tissue-like NMR properties. The Semocosil 921 silicone gel generally meets these requirements (with the exception of tissue-like diffusion) and will be used in subsequent phantom studies. Three-dimensional, stimulated-echo acquisition sequences that have sensitivity to 3-dimensional displacement have been

written and applied to gather 3D strain data on simple objects. These data have been input in newly-designed 3D elasticity reconstruction routines to yield, to the best of our knowledge, the first elasticity reconstruction based on volumetric internal spatial/strain data. Methods to reduce data acquisition time, via stimulated-echo spatial encoding have not yet been satisfactory in terms of artifact control. Complexity of fast-spin-echo sequences on the human MRI unit have slowed our progress to translate these sequences to the human system, although these tasks will be completed outside of the scope of this project.

References

1. A. P. Sarvazyan, A. R. Skovoroda, S. Y. Emelianov, J. B. Fowlkes, J. G. Pipe, R. S. Adler, R. B. Buxton, P. L. Carson, "Biophysical Bases of Elasticity Imaging. Acoustical Imaging," 21, Plenum Press, New York, p. 223-240, 1995.

2. A. R. Skovoroda, A. N. Klishko, D. A.Gukasyan, E. I. Maevsky, V. D. Ermilova, G. A. Oranskaya, and A. P. Sarvazyan, Quantitative analysis of the mechanical characteristics of pathologically altered soft biological tissues. Biofizika, 40(6), 1335-1340, (1995).

3. D. Hill, V. White, D. Jolley, Mapperson, Self examination of the breast: is it beneficial? Meta-analysis of studies investigating breast self examination and the extent of disease in patients with breast cancer. Br J Med 297, 271-275 (1988).

4. P. A. Newcomb, S. Weiss, B. E. Storer, D. Scholes, B. E. Young, Breast self examination in relation to the occurrence of advanced breast cancer. J Natl Cancer Inst 83, 260-265 (1991).

5. R. J. Dickinson, C. R. Hill, Measurement of soft tissue motion using correlation between A-scans. Ultrasound Med Biol 8, 263-271 (1982).

6. M. Tristam, D. C. Barbosa, D. O. Cosgrove, D. K. Nassiri, J. C. Bamber, C. R. Hill, Ultrasonic study of in vivo kinetic characteristics of human tissue. Ultrasound Med Biol 12, 927-937 (1986).

7. M. Tristam, D. C. Barbosa, D. O. Cosgrove, J. C. Bamber, C. R. Hill, Application of Fourier analysis to clinical study of patterns of tissue movement. Ultrasound Med Biol 14, 695-707 (1988).

8. R. M. Lerner, S. R. Huang, K. J. Parker, "Sono-elasticity" images derived from ultrasound signals in mechanically vibrated tissues. Ultrasound Med Biol 16, 231-239 (1990).

9. K. J. Parker, S. R. Huang, R. A. Musulin, R. M. Lerner, Tissue reponse to mechanical vibrations for "sonoelasticity imaging". Ultrasound Med Biol 16, 241-246 (1990).

10. K. J. Parker, R. M. Lerner, Sonoelasticity of organs: shear waves ring a bell. J Ultrasound Med 11, 387-392 (1992).

11. J. Ophir, I. Cespedes, H. Ponnekanti, Y. Yazdi, X. Li, Elastography: a quantitative method for imaging the elasticity of biological tissues. Ultrason Imaging 13, 111-134 (1991).

12. B. S. Garra, E. I. Cespedes, J. Ophir, S. R. Spratt, R. A. Zuurbier, C. M. Magnant, M. F. Pennanen, Elastography of breast lesions: initial clinical results. Radiology 202, 79-86 (1997).

13. M. O'Donnell, A. R. Skovoroda, B. M. Shapo, S. Y. Emelianov, Internal displacement and strain imaging using ultrasonic speckle tracking. IEEE Transactions on Ultrasonic Ferroelectrics and Frequency Control 41, 314-325 (1994).

14. S. Y. Emelianov, M. A. Lubinski, W. F. Weitzel, R. C. Wiggins, A. R. Skovoroda, M. O'Donnell, Elasticity imaging for early detection of renal pathologies. Ultrasound Med Biol 21 (7), 871-883, (1995).

15. L. Axel, L. Dougherty, Heart wall motion: improved method of spatial modulation of magnetization for MR imaging. Radiology 169, 59-63 (1988).

16. E. A. Zerhouni, D. M. Parish, W. J. Rogers, A. Yang, E. P. Shapiro, Human heart: tagging with MR imaging - a method for noninvasive assessment of mycardial motion. Radiology 169, 164-172 (1988).

17. N. J. Pelc, M. Drangova, L. R. Pelc, Y. Zhu, D. C. Noll, B. S. Bowman, R. J. Herfkens, Tracking of cyclic motion with phase-contrast cine MR velocity data J Magn Reson Imaging, 5(3), 339-345 (1995).

18. J. B. Fowlkes, S. Y. Emelianov, J. G. Pipe, A. R. Skovoroda, R. S. Adler, P. L. Carson, A. P. Sarvazyan, Magnetic resonance imaging techniques for detection of elasticity variation. Med Phys 22(11) 1771-1778, (1995).

19. R. Muthupillai, D. J. Lomas, P. J. Rossman, J. F. Greenleaf, A. Manduca, R. L. Ehman, Magnetic resonance elastography by direct visualization of propagating acoustic strain waves. Science 269, 1854-1857 (1995).

20. R. Muthupillai, P. J. Rossman, J. F. Greenleaf, S. J. Riederer, R. L. Ehman, MR imaging of acoustic strain waves: initial in vivo results, in "Proc., International Society for Magnetic Resonance in Medicine, 1996," p. 475.

21. D. B. Plewes, I. Betty, S. N. Urchuk, I. Soutar, Visualizing Tissue Compliance with MR Imaging. J Magn Reson Imaging 5, 733-738 (1995).

22. D. B. Plewes, G. Poole, M. Leitch, S. N. Urchuk, MR assessment of the viscoelastic properties of tissue through the propagation of transient strain waves, in "Proc., International Society for Magnetic Resonance in Medicine, 1996," p. 476.

23. I. Cespedes, J. Ophir, H. Ponnekanti, N. Maklad, Elastography: elasticity imaging using ultrasound with application to muscle and breast in vivo. Ultrason Imaging 15, 73-88 (1993).

24. A. Skovoroda, S. Emelianov, M. Lubinski, A. Sarvazyan, M. O'Donnell, Theoretical analysis and verification of ultrasound displacement and strain imaging. IEEE Transactions on Ultrasonic Ferroelectrics and Frequency Control 41(3), 302-313 (1994).

25. A. Skovoroda, S. Emelianov, M. O'Donnell, Tissue elasticity reconstruction based on ultrasound displacement and strain images: IEEE Transactions on Ultrasonic Ferroelectrics and Frequency Control, 42(4), pp. 747-765 (1995).

26. S. Y. Emelianov, A. R. Skovoroda , M. A. Lubinski, M. O'Donnell, Reconstructive elasticity imaging. Acoustical Imaging," 21, Plenum Press, New York, p. 241-253, 1995.

27. T.L. Chenevert, S.Y. Emelianov, AR Skovoroda: Elasticity Reconstructive Imaging Using Static Displacement and Strain Estimations. Proceedings of the International Society of Magnetic Resonance in Medicine, p-461, 1997.

28. T.L. Chenevert, A.R. Skovoroda, M. O'Donnell, and S.Y. Emelianov, "Elasticity reconstructive imaging via stimulated echo MRI," Magnetic Resonance in Medicine, 39, pp. 482-490 (1998). See Appendix.

APPENDIX:

Publications supported by this grant

T.L. Chenevert, A.R. Skovoroda, M. O'Donnell, and S.Y. Emelianov, "Elasticity reconstructive imaging via stimulated echo MRI," Magnetic Resonance in Medicine, 39, pp. 482-490 (1998).

Chenevert, TL, Steele, DD, Emelianov, SY and Shovoroda, AR. "Three-Dimensional Static Displacement Stimulated-Echo NMR Strain Imaging". Proceedings of the International Society of Magnetic Resonance in Medicine 1999; 263.

Steel, DD and Chenevert, TL, Emelianov, SY, and O'Donnell, M. "Signal-to-Noise Consideration in Static Displacement, Stimulated Echo NMR Elasticity Imaging". Proceedings of the International Society of Magnetic Resonance in Medicine 1999; 1616.

A.R. Skovoroda, M.A. Lubinski, S.Y. Emelianov, and M. O'Donnell, "Reconstructive elasticity imaging for large deformations," IEEE Transactions on Ultrasonics, Ferroelectrics, and Frequency Control, 46, pp. 523-535 (1999).

Derek D. Steele, Thomas L. Chenevert, Andrei R. Skovoroda and Stanislav Y. Emelianov, "Three-dimensional static displacement, stimulated echo NMR elasticity imaging,". Physics in Medicine and Biology 45 (2000) 1633-1648.

Articles "In Preparation" supported by this grant:

(These can be viewed in PDF format at: http://bul.eecs.umich.edu/research/emelian/army.html)

A.R. Skovoroda, D.D. Steele, T.L. Chenevert, M. O'Donnell and S.Y. Emelianov, "Three-dimensional reconstructive elasticity imaging using stimulated echo MRI," submitted for publication in the Magnetic Resonance in Medicine (2000).

A.R. Skovoroda, R.Q. Erkamp, S.Y. Emelianov, and M. O'Donnell, "Nonlinear elasticity reconstruction for clearly bounded inhomogeneities," submitted for publication in the IEEE Transactions on Ultrasonics, Ferroelectrics, and Frequency Control (2000).

Elasticity Reconstructive Imaging by Means of Stimulated Echo MRI

Thomas L. Chenevert, Andrei R. Skovoroda, Matthew O'Donnell, Stanislav Y. Emelianov

A method is introduced to measure internal mechanical displacement and strain by means of MRI. Such measurements are needed to reconstruct an image of the elastic Young's modulus. A stimulated echo acquisition sequence with additional gradient pulses encodes internal displacements in response to an externally applied differential deformation. The sequence provides an accurate measure of static displacement by limiting the mechanical transitions to the mixing period of the simulated echo. Elasticity reconstruction involves definition of a region of interest having uniform Young's modulus along its boundary and subsequent solution of the discretized elasticity equilibrium equations. Data acquisition and reconstruction were performed on a urethane rubber phantom of known elastic properties and an *ex vivo* canine kidney phantom using <2% differential deformation. Regional elastic properties are well represented on Young's modulus images. The long-term objective of this work is to provide a means for remote palpation and elasticity quantitation in deep tissues otherwise inaccessible to manual palpation.

Key words: elastic Young's modulus; magnetic resonance imaging; elastography; strain imaging.

INTRODUCTION

It is well known that tissue elastic properties may be altered by tumors. Young's elastic moduli may differ by orders of magnitude in soft tissues in various physiologic states (1, 2). This finding is the physical basis behind manual palpation used to detect "hard" masses (3, 4). Indeed, physical examination is the first diagnostic line of defense against breast cancer, because nodule hardness raises suspicion of malignancy. Detection of a new breast mass by physical examination is often sufficient for surgical excisional biopsy, even when not corroborated by other diagnostic tests. Manual palpation of the prostate, superficial lymph nodes, and abdominal organs are also commonly performed. Unfortunately, sensitivity of palpation is relatively poor within deep, dense, or heterogeneous tissues. Although the touch of a skilled interpreter is considered a powerful diagnostic instrument, most lesions detected by palpation tend to be relatively large and superficial.

Scientists are attempting to electronically extend the touch of the physical examiner using a variety of image-based techniques that infer tissue elasticity. The essential element is measurement of internal motion and strain in tissue structures experiencing mechanical stress. To date, most "elastography" has used ultrasound to track the relative motion of targets by specular reflection (5–7), by Doppler techniques (8–10), by cross-correlation of raw or processed acoustic echoes (11, 12), or by tracking speckle patterns (13–15). Usually an external static or dynamic deformation is applied while internal displacements or propagating shear waves are documented by imaging.

MRI has also been used to measure internal displacement and strain components of the heart using spatial magnetization tagging (16, 17) and phase-based velocity encoding (18). Elasticity reconstruction of an externally deformed phantom was demonstrated using magnetization tagging, but this method has spatial resolution limited by the tagged grid size and only measures 2D motion (19). More recently, motion phase encoding by means of bipolar gradients was used to produce two-dimensional (2D) displacement and strain maps in media mechanically driven by external forces (20–23). Strain and displacement maps infer internal elasticity but are also strongly affected by the applied deformational geometry. Consequently, these maps do not uniquely reflect internal tissue properties (i.e., elastic Young's modulus). Maps of dynamic strain-wave propagation, however, do allow measurement of local strain wavelength or velocity from which the local elastic modulus can be derived (20). Shear-wave attenuation, interference from standing waves off multiple reflectors, and limited resolvable points over the shear wavelength are potential drawbacks of this approach.

Relative to ultrasound, MRI has an advantage in overall resolution and accuracy for multidimensional displacement and strain measurement needed for elasticity reconstruction. Ultrasound can accurately measure axial (i.e., along the beam axis) motion at high spatial resolution (≤millimeter), but lateral displacement is measured at much lower spatial resolution defined by the depth-dependent acoustic beam width. The third dimension is generally not even considered given the limitations of ultrasound. Consequently, reduced motion dimensionality and overall low motion resolution of the imaging system compromise the "elastogram." This shortcoming, in turn, constrains the mechanical model used in elasticity reconstruction. To date, only 1D motion models have been applied to ultrasound-derived elasticity images of tissues *in vivo* (12, 24). More accurate elasticity images are achieved by properly controlling external deforma-

tions, leading to 2D elasticity reconstruction within the imaging plane (25, 26).

In this work we present a method to spatially encode internal displacement of an object that has undergone an externally applied "static" deformation with subsequent reconstruction into elasticity maps. Unlike dynamic techniques designed to estimate elasticity from observations related to strain-wave propagation, static elasticity reconstruction involves estimation of local strain from displacement and numerical solution of differential elasticity equilibrium equations.

THEORY OF RECONSTRUCTIVE ELASTICITY IMAGING

The goal of elasticity imaging is to reconstruct the elastic modulus of a desired tissue region using available measurements of displacement and strain components. Indeed, the mechanical properties of tissue are ultimately linked to the patterns of internal deformations, but the deformational geometry can greatly affect these patterns as well. To uniquely image tissue elasticity, the Young's modulus must be reconstructed from estimates of internal displacement and strain.

In this paper, the general approach to elasticity reconstruction was based on a model of linear, elastic, isotropic, incompressible media (26, 27). The key equations and considerations are briefly presented here. A more detailed description of elasticity reconstruction is given in an earlier publication (26).

In linear elasticity, the components of the strain (ε_{ij}) and stress (σ_{ij}) tensors under static deformation are:

$$\varepsilon_{ij} = \frac{1}{2}\left(\frac{\partial u_i}{\partial x_j} + \frac{\partial u_j}{\partial x_i}\right) = \frac{1}{2}(u_{i,j} + u_{j,i}) \qquad [1]$$

$$\sigma_{ij} = p\delta_{ij} + \frac{2}{3}E\varepsilon_{ij} \qquad [2]$$

where u_i is a component of the displacement vector $\mathbf{U} = (u_1, u_2, u_3)$ in Cartesian coordinates $\mathbf{X} = (x_1, x_2, x_3)$, p is the static internal pressure, δ_{ij} is the Kronecker delta symbol, and $E = E(x_1, x_2, x_3)$ is the Young's elastic modulus. Note in Eq. [1], and the entire paper, the lower index after a comma means differentiation with respect to the corresponding spatial coordinate.

The static deformation of the medium can be described by the equilibrium condition:

$$\sum_{j=1}^{3} \sigma_{ij,j} + f_i = 0, \qquad i = 1,2,3 \qquad [3]$$

where f_i is the body force per unit volume acting in the x_i direction. In addition, volume conservation for an incompressible medium leads to the following relationship between displacement and strain components

$$\nabla \cdot U = \varepsilon_{11} + \varepsilon_{22} + \varepsilon_{33} = u_{1,1} + u_{2,2} + u_{3,3} = 0 \qquad [4]$$

Using Eqs. [1] and [2] for stress and strain components, and the incompressibility Eq. [4], the equilibrium condi-

tion with eliminated internal pressure p can be rewritten in the following form:

$$2\varepsilon_{12}(E_{,11} - E_{,22}) + 2(u_{2,2} - u_{1,1})E_{,12} + 2\varepsilon_{23}E_{,13}$$

$$- 2\varepsilon_{13}E_{,23} + (\nabla^2 u_2 + \omega_{12,1})E_{,1} - (\nabla^2 u_1 - \omega_{12,2})E_{,2}$$

$$+ \omega_{12,3}E_{,3} + \nabla^2\omega_{12}E + 3(f_{2,1} - f_{1,2}) = 0$$

$$2\varepsilon_{13}(E_{,11} - E_{,33}) + 2\varepsilon_{23}E_{,12} + 2(u_{3,3} - u_{1,1})E_{,13}$$

$$- 2\varepsilon_{12}E_{,23} + (\nabla^2 u_3 + \omega_{13,1})E_{,1} + \omega_{13,2}E_{,2} \qquad [5]$$

$$- (\nabla^2 u_1 - \omega_{13,3})E_{,3} + \nabla^2\omega_{13}E + 3(f_{3,1} - f_{1,3}) = 0$$

$$2\varepsilon_{23}(E_{,22} - E_{,33}) + 2\varepsilon_{13}E_{,12} - 2\varepsilon_{12}E_{,13} + 2(u_{3,3}$$

$$- u_{2,2})E_{,23} + \omega_{23,1}E_{,1} + (\nabla^2 u_3 + \omega_{23,2})E_{,2} - (\nabla^2 u_2$$

$$- \omega_{23,3})E_{,3} + \nabla^2\omega_{23}E + 3(f_{3,2} - f_{2,3}) = 0$$

$$\omega_{12} = u_{2,1} - u_{1,2}, \quad \omega_{13} = u_{3,1} - u_{1,3}, \quad \omega_{23} = u_{3,2} - u_{2,3}$$

Clearly, the elasticity reconstruction process based on Eq. [5] requires accurate measurements of the displacement vector, or, to be more precise, requires accurate estimation of up to third-order spatial derivatives of the displacement. Equation [5] can also be written in terms of spatial derivatives of strain tensor components. The unique solution of the system of coupled partial differential equations [5] is determined by the boundary conditions, i.e., the elastic modulus $E(\mathbf{X})$ must be given along the boundary of the reconstruction region of interest (ROI). It should also be noted here that the analytical solution of Eq. [5] is not generally possible, and numerical methods must be developed to solve this system of partial differential equations.

Based on the particular geometry of the phantoms and deformation system used in these experiments, Eq. [5] was simplified. A 2D approximation of Eq. [5] was used because the imaged plane was near the center of the
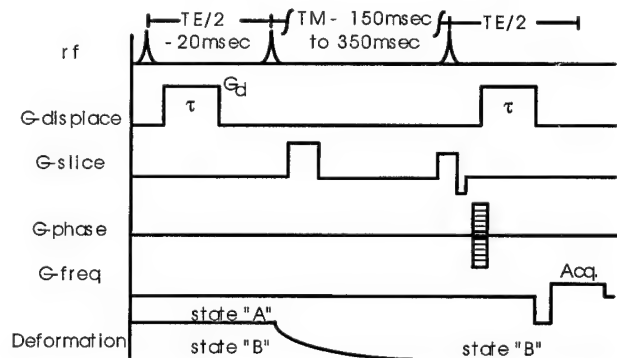

FIG. 1. Stimulated-echo data acquisition and object deformation sequence. Mechanical transitions occur during the long mixing time (TM) such that a static displacement equilibrium is achieved. Local displacement between deformation states "A" and "B" are encoded by phase shift proportional to "G-displace" amplitude G_d, and duration τ.
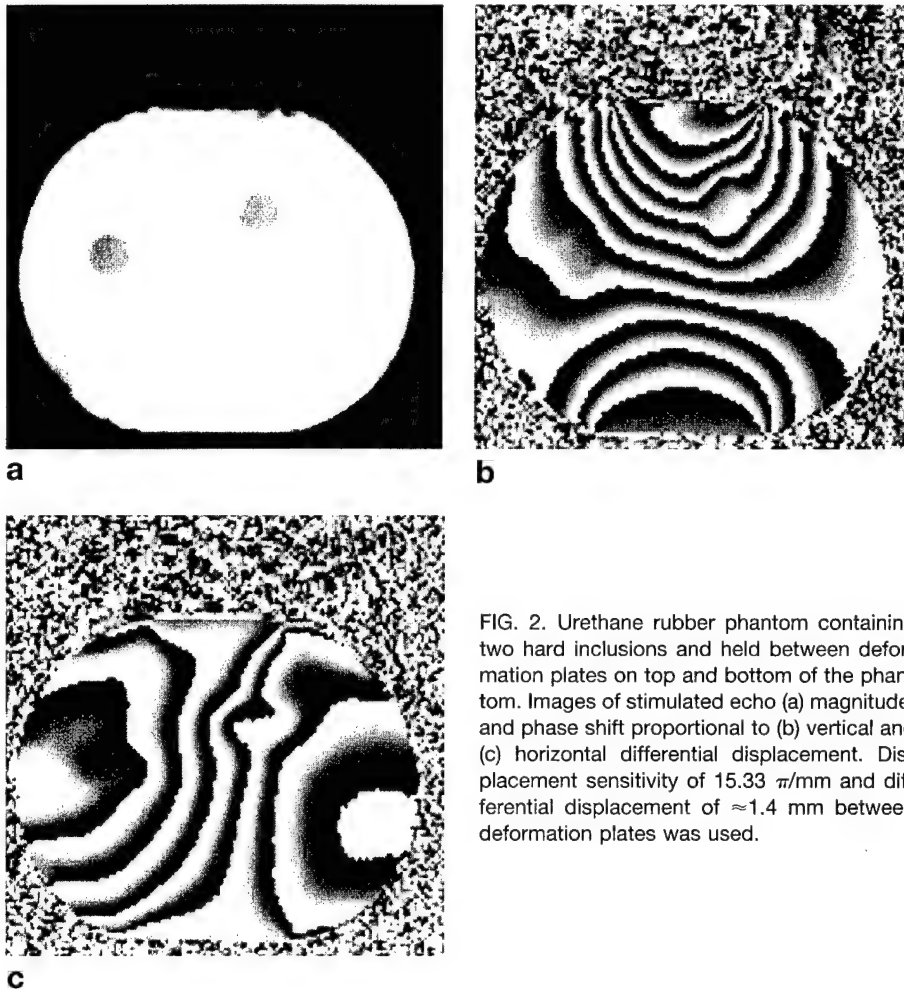
FIG. 2. Urethane rubber phantom containing two hard inclusions and held between deformation plates on top and bottom of the phantom. Images of stimulated echo (a) magnitude, and phase shift proportional to (b) vertical and (c) horizontal differential displacement. Displacement sensitivity of 15.33 π/mm and differential displacement of $\approx$1.4 mm between deformation plates was used.

founded by interference of the primary shear wave with reflected or standing shear waves. To avoid this condition, a "static" displacement encoding approach was adopted. It requires measurement of internal displacement between two or multiple deformations while the object is in mechanical equilibrium for each measurement. A stimulated echo sequence with displacement-encoding gradient pulses is used to achieve this, as shown in Fig. 1. Mechanical transition from state "A" to state "B" occurs during the stimulated echo mixing time, TM. A relatively long mixing time allows long-lived elastic vibrations to dampen before spatial encoding. Because the relevant magnetization during TM is longitudinal, it is unaffected by potentially ill-defined motions during the mechanical transition period. As a result, a more accurate static deformation measurement is achieved. Also note that precise synchronization of mechanical and pulsed gradient events is not critical as long as the mechanical transition begins after the second RF pulse and is complete before the third RF pulse. Similarly, a long delay in TE could be used, but this is done at the expense of signal lost to T_2 decay.

Local displacement is encoded by means of phase shift governed by pulsed-field gradient factors,

$$\vec{\Phi}_d = \gamma \, \vec{G}_d \, \tau \qquad [7]$$

where displacement sensitivity, Φ_d, is in units of (radians/distance). A phase reference acquisition is required for each displacement encode condition to remove preexisting phase shifts that are unrelated to displacement. Reference data are acquired using the same pulse sequence, including displacement encode gradient pulses, but with the object maintained in state B. Note that all spatial encoding occurs from the third RF pulse and beyond. That is, the object is in one deformation state (state B) for both displacement and phase reference acquisitions during all spatial encoding segments of the sequence. Consequently, image registration or feature tracking algorithms (14) are not required to estimate displacement. Instead, local displacement is encoded directly by local phase of a corrected dataset, S_{cor}, given by,

$$S_{cor}(\vec{r}) = \frac{S_A(\vec{r}) \, S_B(\vec{r})^*}{|S_B(\vec{r})|} \cong |S_A(\vec{r})| \, e^{i\varphi(\vec{r})} \qquad [8]$$

phantom. For such a plane (arbitrarily denoted as $x_3 = 0$), the displacement vector components do not vary significantly as a function of the out-of-plane x_3 coordinate, and therefore, the "plane strain state" condition is applicable. With this condition, Eq. [5] reduces to a single nontrivial equation:

$$(E_{,11} - E_{,22})(u_{1,2} + u_{2,1}) + 2E_{,12}(u_{2,2} - u_{1,1})$$
$$+ 2E_{,1}(u_{2,11} + u_{2,22}) - 2E_{,2}(u_{1,11} + u_{1,22}) \qquad [6]$$
$$+ E(u_{2,111} + u_{2,221} - u_{1,112} - u_{1,222}) + 3(f_{2,1} - f_{1,2}) = 0$$

Under conditions in which these assumptions are valid, only in-plane displacement u_1 and u_2 or their derivatives are needed to reconstruct the modulus in the plane $x_3 = 0$.

Static Displacement Measurement by Means of Stimulated Echo MRI

Shear-wave propagation speed in soft tissue is 1–20 m/s. Consequently, a shear wave imparted by a single-stroke or an oscillating deformation force may require tens of milliseconds to traverse an object $\approx$100 mm in size. The time for reflected waves to dampen may be much longer. "Dynamic" measurements, which encode displacement during shear-wave propagation, are potentially con-
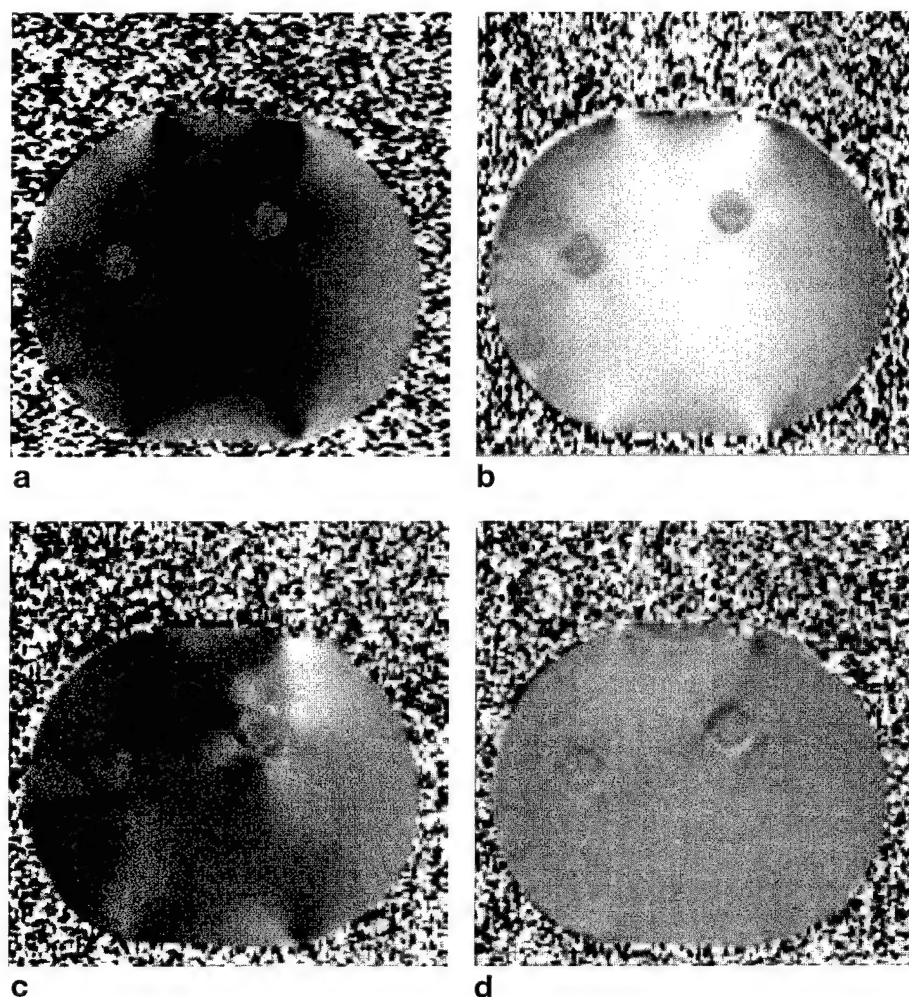
FIG. 3. Strain images calculated from first-order derivatives of the displacement images represented in Fig. 2. Normal strains (a) ε_{11} and (b) ε_{22}, and (c) shear strain $\varepsilon_{12} = \varepsilon_{21}$ reflect internal elastic properties and the externally applied deformation field. The plane strain state assumption and phantom incompressibility suggest $\varepsilon_{11} \approx -\varepsilon_{22}$ as is supported by the relatively featureless map of $\varepsilon_{11} + \varepsilon_{22}$ in (d).

10.5 ± 1.5 for 30% surface deformation (19). In the present study, smaller surface deformation was applied, and consequently, the elasticity contrast within this phantom should be less than the previously measured ratio. Whereas the mechanical properties of the rubber phantom mimic soft tissue, the phantom had inherently poor NMR signal. A more tissue-equivalent phantom in terms of NMR and mechanical properties was achieved by embedding a fresh canine dog kidney (<24 h *ex vivo*) into a 130 mm × 105 mm × 75 mm block of 5% gelatin. One hour before MRI, 10 ml of 5% glutaraldehyde solution was injected into kidney parenchyma to create a hard lesion(s).

Phantoms were held securely in place under moderate preload pressure by two parallel acrylic plates. When pressure to the top plate was released, the phantom recoiled vertically an amount constrained by physical stops. Maximum vertical displacement was <1.5 mm, which represented <2% differential between state "A" (greater deformation) and state "B" (less deformation). Deformation was actuated pneumatically by an air-filled bladder on top of the phantom holder. Pneumatic pressure was stepped by a remote solenoid valve with timing controlled by an external transistor transistor logic (TTL) gate circuit triggered by the pulse sequence.

where S_A and S_B are the data acquired with the object initially in state A and state B, respectively. The unwrapped phase of the corrected dataset and Eq. [7] provides a local measure of displacement, U, by means of;

$$\varphi(\vec{r}) = \vec{\Phi}_d \cdot [\vec{r}_A - \vec{r}_B] = \vec{\Phi}_d \cdot U(\vec{r}) \qquad [9]$$

Most sources of phase error, such as static field inhomogeneity, tend to be slowly varying functions of position. Therefore, the phase reference datasets may be acquired at relatively low spatial resolution to reduce scan time.

METHODS

Data Acquisition

Elasticity imaging was performed on two phantoms. One was an 85-mm diameter cylindrical urethane rubber phantom containing two 8-mm cylinders of hard material. Previously, the ratio of Young's modulus between the inclusion and background material was measured

Displacement encoding gradient pulse duration, $\tau = 4.5$ msec, and amplitude, Gd = 40 mT/m, provided a displacement sensitivity of $\Phi_d = 15.33 \ \pi/\text{mm}$ by means of Eq. [7]. The displacement encoding direction was alternated each pulse repetition between vertical and horizontal. For the urethane rubber phantom, acquisition parameters were $TR = 1.3$ s, TM = 350 msec, $TE = 50$ msec, 128 × 128 matrix, four signal averages, 100 mm field of view, and 10-mm section thickness. An additional 128 × 32 matrix acquisition was collected for phase-reference correction of vertical and horizontal encoded data. The kidney phantom acquisition parameters were $TR = 1$ s, TM = 200 msec, $TE = 76$ msec, 256 × 256 matrix, two signal averages, 150 mm field of view, and 5-mm section thickness; with a 256 × 32 dataset acquired for phase correction. All experiments were performed on a 2 T 18-cm bore MRI system (Bruker, formerly GE NMR
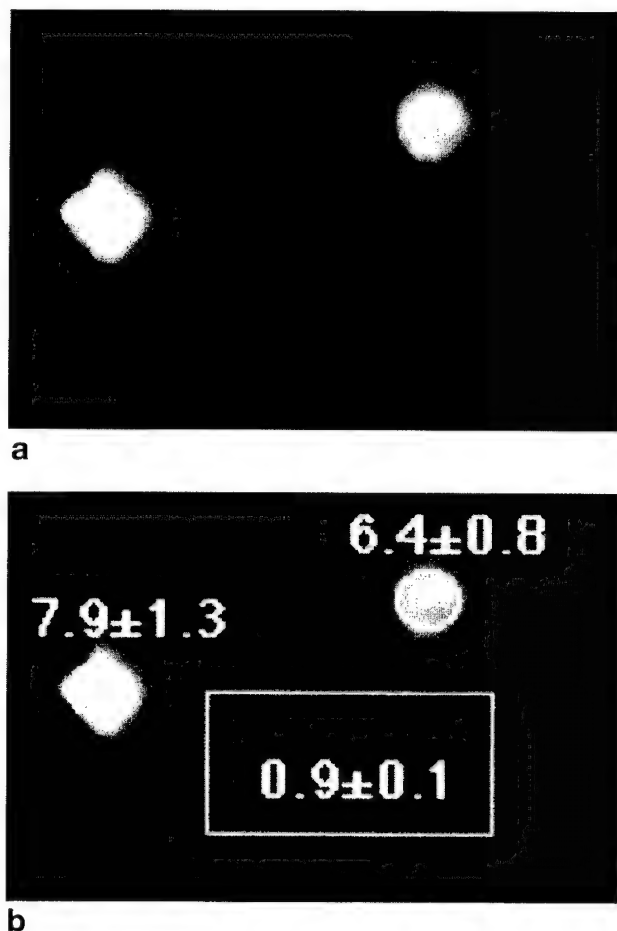
a

b

FIG. 4. (a) Reconstructed map of Young's modulus for the urethane rubber phantom within a 63 × 50 mm region. The boundary of the region is defined to have a Young's modulus = 1. Relative Young's moduli for inclusions and background material are shown in (b).

Instruments), using a 150-mm transmit/receive birdcage coil.

Data Processing

Time-domain data were transferred for off-line processing as follows. Phase reference datasets were zero-filled and 2D Fourier transformed to a 128 × 128 or 256 × 256 matrix for phase correction by means of Eq. [7]. The resulting phase maps were used to estimate the spatial derivatives of the in-plane displacements necessary for elasticity reconstruction (6). Note phase unwrapping is not strictly required because only phase derivatives are used. Assuming the displacement fields are continuous, resulting in small differential displacement at any pixel compared with the total displacement, the differential displacement between two neighboring pixels was directly computed from the angle of the complex multiplication of each pixel with the conjugate of the neighboring pixel, then scaled by $1/\Phi_d$.

Solving Eq. [6] for unknown E (x1, x2) performed the elasticity reconstruction, i.e., reconstruction of the spatial distribution of elastic Young's modulus. As was noted previously, the unique solution of a boundary value problem (Eq. [5] or [6]) is determined by the bound-

ary conditions. Therefore, a rectangular ROI was identified within the imaging planes for both phantoms. For the phantom with two hard inclusions, the ROI was a region of 63 × 50 mm positioned approximately in the center of the phantom and included both inclusions. For the canine kidney phantom, the rectangular 94 × 51 mm ROI included the whole kidney cross-section. In both cases, the Young's modulus value along the ROI boundary was set to "one" resulting in reconstruction of relative Young's modulus. More detailed analysis and discussion of defining the ROI was considered previously (26).

Elasticity reconstruction Eqs. [5] and [6] assume that spatial derivatives of the Young's modulus are continuous functions. To ensure continuous elasticity distribution, the spatial derivatives of the displacement were low-pass filtered before elasticity reconstruction, resulting in mild spatial resolution reduction.

After defining the boundary conditions, Eq. [6] was discretized over the ROI with the same grid spacing as the MR images, where all spatial derivatives of the displacement/strain (i.e., coefficients in Eq. [6] for unknown Young's modulus distribution) were approximated by finite differences. The linear set of equations resulting from discretization of Eq. [6] was solved iteratively, where the error in each step was estimated by averaging the left-hand side of Eq. [6] over the ROI using the current estimate of the elasticity distribution. From step to step, the Young's modulus distribution was updated based on the changes in the average error.

RESULTS

Magnitude and corrected phase images of the urethane rubber phantom are shown in Fig. 2. Given that $\Phi_d = 15.33 \pi/\text{mm}$, the number of 2π phase bands in Fig. 2b indicates that the vertical excursion of the phantom top relative to the bottom was ≈1.4 mm; similarly, the relative lateral displacement between left and right edges of the phantom was ≈0.8 mm (Fig. 2c). Reduced phase slopes in the regions of the hard inclusions are clearly visible on the phase images. Normal strain, ε_{11} and ε_{22}, and shear strain, $\varepsilon_{12} = \varepsilon_{21}$, maps are illustrated in Figs. 3a–3c, respectively. The observed contrast reversal between ε_{11} and ε_{22} is a result of phantom incompressibility (like soft tissue), which yields $\varepsilon_{11} = -\varepsilon_{22}$ assuming negligible out-of-plane strain. Consequently, the sum ($\varepsilon_{11} + \varepsilon_{22}$) is relatively "flat" as shown at equivalent gray-scale settings in Fig. 3d. Also note, whereas the strain maps clearly exhibit object-specific detail (i.e., inclusions), features related to the applied external deformation are quite conspicuous. This fact demonstrates why an elasticity reconstruction is needed. The Young's modulus was reconstructed for a 63 × 50 mm region as presented in Fig. 4a. The boundary of the elasticity reconstruction area was defined to have value "1." The relative elastic moduli for select regions are indicated in Fig. 4b and are consistent with the known elasticity of these materials (19).

The canine kidney phantom is shown in Fig. 5 as magnitude (Fig. 5a), vertical (Fig. 5b), and horizontal (Fig. 5c) phase shift images. It is apparent from the vertical phase image (Fig. 5b) that although ≈1.24-mm rel-
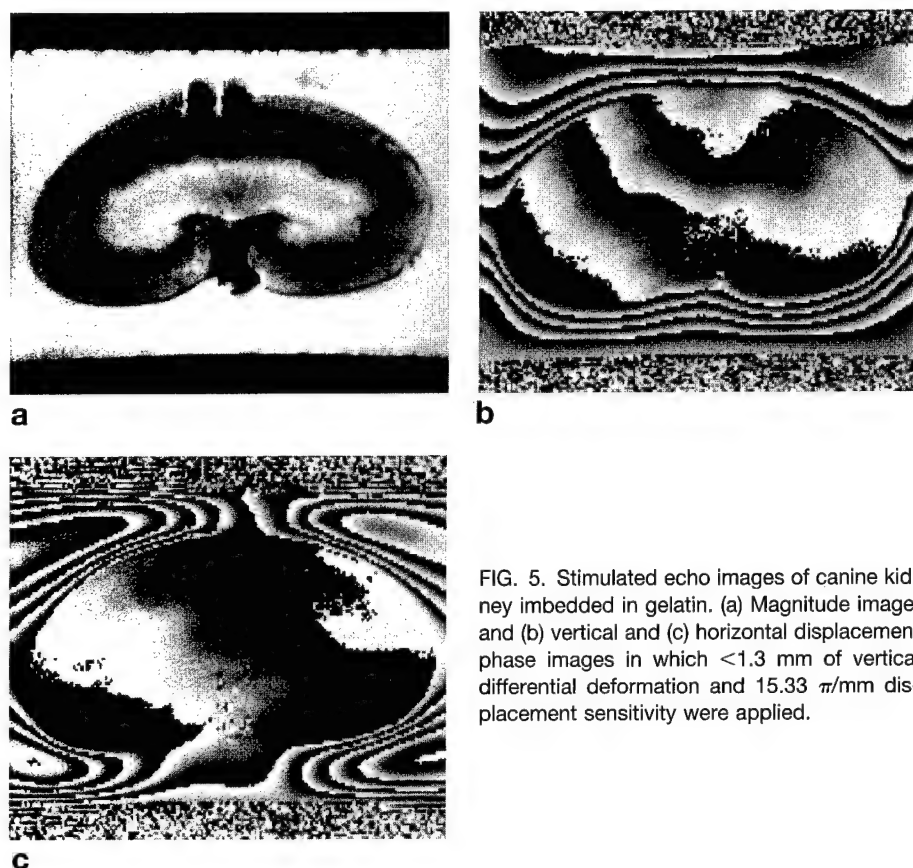
a   **b**

FIG. 5. Stimulated echo images of canine kidney imbedded in gelatin. (a) Magnitude image, and (b) vertical and (c) horizontal displacement phase images in which <1.3 mm of vertical differential deformation and 15.33 π/mm displacement sensitivity were applied.

c

phase using a stimulated echo sequence. Internal displacements occur in response to an external deformation force synchronized to the acquisition sequence. By timing control, mechanical motion occurs while the relevant magnetization is longitudinal. The stimulated echo allows extension of the mechanical transition period to avoid potentially long-lived or ill-defined oscillations within the object such that an estimate of "static" displacement is achieved. Image registration or feature tracking (14) is not required because the object is in one deformation state for all spatial encoding. T_1 relaxation and diffusion, which erode signal, ultimately set practical limits on this period. In these experiments, 200 to 350 msec was sufficient to allow static displacement measurement of rubber and gelatin/tissue phantoms using a simple air-bladder pneumatic system. This arrangement required the object to "passively" recoil during the TM period. Clearly, a faster deformation system can be built using external forces to "actively" deform the object during the stimulated echo mixing period. A shorter mixing time would then be used yielding a larger signal.

ative displacement spans the full phantom, only ≈0.26 mm of it is within the kidney. Consequently, there is a high concentration of strain near the gel-kidney interface, as is clear on the strain maps (Fig. 6). As noted before, strain images exhibit contrast related to a combination of internal structure and the externally applied deformation. Elasticity reconstruction, however, reduces the ambiguity and exhibits contrast dominated by internal elastic properties (Fig. 7a). It is also encouraging to note that whereas there was only moderate strain contrast within the kidney, elasticity contrast within renal parenchyma and central sinus are well distinguished on the Young's modulus image. Moreover, the site of glutaraldehyde injection (top-right quadrant of images) exhibited the highest relative Young's modulus. Approximately 20 h after MRI, the kidney phantom was sliced at a plane corresponding to that studied by MRI. An optical image of this slice is shown in Fig. 7c. The freshly cut surface was palpated such that areas of relatively "hard" parenchyma could be noted. Arrows in Fig. 7c mark the most conspicuous areas of hardness; the largest area corresponds to the high Young's modulus region in the upper-right quadrant of the kidney.

DISCUSSION

In this work we introduce a method to image and quantify internal elastic properties of an object by means of displacement-sensitive MRI with associated elasticity reconstruction. The data acquisition segment employs gradient pulses to encode internal displacement by means of

To date, two approaches are present in elasticity imaging: static reconstructive elasticity imaging (25, 26) and dynamic shear-wave elasticity imaging (20, 21, 23). In both, an external static or dynamic deformation is applied while the resulting displacement/strain or propagating shear wave is detected using an imaging modality. In reconstructive elasticity imaging, the elasticity distribution must be reconstructed from static displacement and strain images. The ability to control the internal deformation pattern by varying the externally applied load, and high SNR displacement and strain estimates are the benefits of this method, although numerical reconstruction algorithms are required. Wherein the modeled assumptions are valid, these algorithms exist. For more general applications, they must be refined further. In shear-wave elasticity imaging, local shear wavelength measurements allow direct and simple calculation of the shear elastic modulus. However, the interference of shear waves reflected from any elasticity inhomogeneities within the tissue, along with attenuation of shear waves, and conversion between shear and bulk waves are challenges of this method.

In these experiments a displacement sensitivity of Φ_d = 15.33 π/mm was achieved using moderate gradient factors. The ultimate quality of Young's modulus reconstruction depends on the induced phase shift, equal to
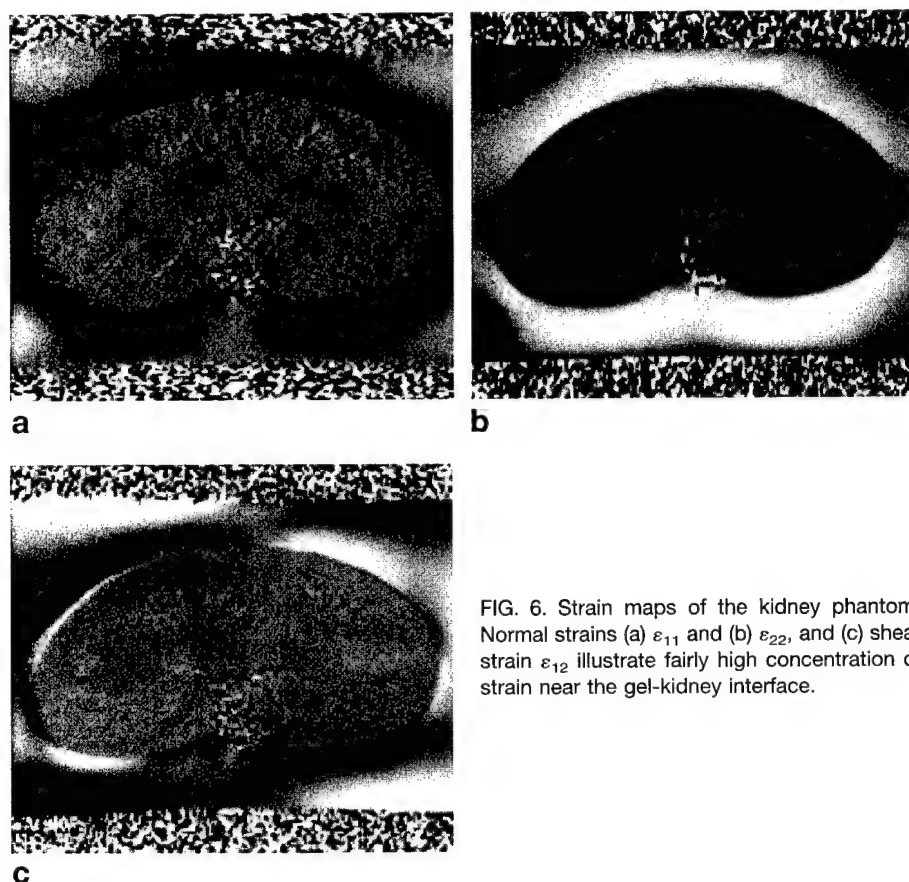
a

b

c

FIG. 6. Strain maps of the kidney phantom. Normal strains (a) ε_{11} and (b) ε_{22}, and (c) shear strain ε_{12} illustrate fairly high concentration of strain near the gel-kidney interface.

the product of Φ_d and local displacement. There is a limit, however, to the advantages gained by increasing phase shift. As spatial phase gradients become large, the phase distribution within a given voxel reduces signal amplitude. Assuming a linear phase distribution of range β with a voxel, the signal modulation function is given by $\text{sinc}(\beta)$. For illustration, consider the vertical phase excursion of $21\ \pi$ observed across the 80-mm phantom in Fig. 2b. If the vertical phase excursion was evenly distributed across voxels, the phase range within each 0.78-mm voxel would be approximately $0.2\ \pi$. This implies a signal reduction factor of $\text{sinc}(0.2\ \pi) = 0.94$ (i.e., signal loss of 6%). Clearly phase gradients can be more concentrated depending on object geometry, elastic heterogeneity, and deformation geometry. This concentration can lead to regions of significant signal loss in a manner analogous to flow dephasing in conventional MRI. Under such conditions, a smaller voxel size can (paradoxically) yield higher signal. In addition, inspection for significant signal loss within the displacement-sensitive magnitude image can identify high-strain regions near soft/hard interfaces of a lesion.

Water diffusion in the presence of displacement encoding gradients is another source of signal attenuation. We estimate the signal reduction factor for freely diffusing water was ≈ 0.24 in these experiments (i.e., 76% signal lost to diffusion effects). Diffusion effects are lessened by reducing Φ_d, or alternatively by shortening TM without affecting Φ_d. In either case, diffusion effects are assumed independent of the deformation state, and

therefore are ignored in the elasticity reconstruction. Because displacement phase shift is the product of local displacement and Φ_d, the selection of Φ_d is somewhat arbitrary as long as the applied differential deformation is adequate for elasticity reconstruction. In these preliminary experiments, the differential deformation was <1.5 mm across the imaged object. For multi-step acquisitions, as done here, good reproducibility of deformation is essential. Significant variation in deformation magnitude over the acquisition will lead to phase instability, motion-like artifact in base images, and errors that propagate through the elasticity reconstruction. It is a minor technical challenge to achieve relatively high displacement reproducibility in the deformation apparatus. Irreproducible motions that originate within the imaged object, however, can be problematic and are analogous to undesired physiologic motion artifacts in *in vivo* diffusion MRI. Fortunately, unlike diffusion and physiologic motions, the targeted motion in elasticity imaging is externally driven. As such, the displacement amplitude in response to an external differential deformation can be significantly greater than irreproducible or asynchronous displacement. For many *in vivo* applications including the breast, increasing the differential deformation severalfold relative to that applied in these phantom studies can reduce motion artifact. Gradient factors and Φ_d would be reduced accordingly, which would yield the added benefit of increased signal otherwise lost to diffusion effects.

In practice, the definition of a closed contour of constant Young's modulus within the tissue can be a challenge. A hybrid procedure can be used as detailed elsewhere (26) and summarized as follows. The strain images are first processed to highlight boundaries between regions of different elastic modulus. This procedure is based on the stress continuity property of continuous media such as tissue and can define regions of very small modulus variations. After this boundary detection, closed contours of small elasticity variations are defined. The modulus along the contours is considered constant, thereby providing the boundary condition for complete reconstruction of the elasticity within the region of interest based on numerical solution of Eq. [6]. The elasticity distribution reconstructed in this way is the modulus relative to the modulus along the boundary. For breast elasticity imaging, it is anticipated that such a contour can be defined *a priori* within the subcutaneous fat that surrounds breast parenchyma. As-
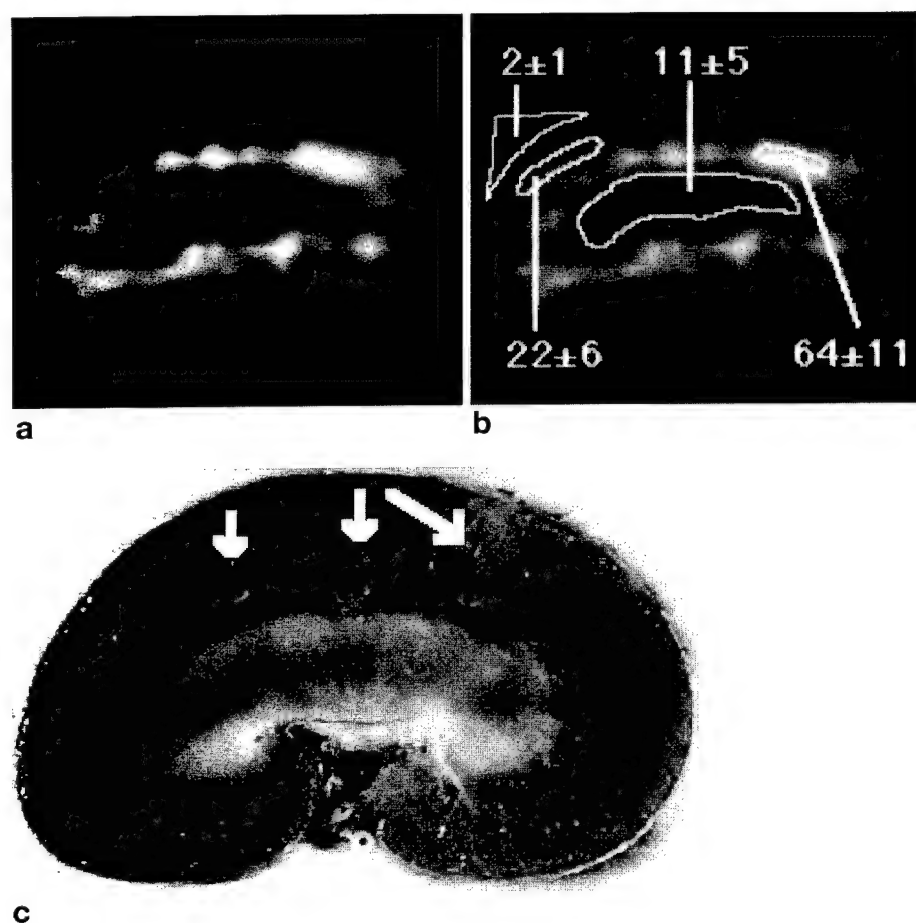
FIG. 7. (a) Reconstructed Young's modulus image within a rectangular 94 × 51 mm region encompassing the kidney. (b) Relative Young's modulus for the scribed ROIs indicate high elastic modulus at the glutaraldehyde injection site in the upper-right quadrant of the kidney parenchyma. (c) The optical image of the kidney phantom approximately 20 h after MRI. Areas marked by arrows were noticeably harder as assessed by sense of manual touch.

range to include deep lying lesions. One application would be measurement of elasticity in breast tissue not accessible to manual palpation. *In situ* studies of Young's elastic modulus performed on samples of breast tissue indicate that there is a large difference in elastic modulus between normal and pathologically transformed breast tissues. Others have analyzed the Young's modulus differences between different soft tissues and have found 1–2 orders of magnitude difference in Young's elastic moduli of a tissue in different physiologic states (1). If elastic changes predate formation of calcifications, elasticity imaging could potentially increase detection and/or characterization of malignant breast masses and thus be an important addition to existing clinical diagnostic tools. Practical issues such as the relatively high cost of MRI may hinder use of this approach as a screening test. Nevertheless, additional work to define the role of this technique as a primary diagnostic tool or supplemental problem-solving modality in the management of soft-tissue disease is well justified.

suming the Young's modulus of the fat boundary is constant, the relative Young's modulus image of parenchyma can be reconstructed. Alternatively, the breast can be surrounded by a high-signal cuff of known elastic modulus and imaged. An image of absolute Young's modulus can then be reconstructed if the boundary contour is defined within the cuff material.

Some artifacts present in elasticity images (Figs. 4 and 7) are due to violation of the plane strain state approximation in these experiments. Indeed, if a plane strain state is not present, the reconstruction based on Eq. [6] will be in error. The elasticity reconstruction, however, does not have to be limited by a plane strain assumption if all 3D components of the displacement vector are available. Fortunately, such information would be available using 3D displacement encoding within a volumetric imaging sequence. The issue of long scan time could be resolved by incorporating echoplanar imaging or fast-spin-echo segments for spatial encoding. Correspondingly, an elasticity reconstruction based on Eq. [5] would be applied to produce volumetric elasticity maps.

The long-range goal of quantitative elasticity imaging is to provide remote palpation thus expanding its limited

REFERENCES

1. A. P. Sarvazyan, A. R. Skovoroda, S. Y. Emelianov, J. B. Fowlkes, J. G. Pipe, R. S. Adler, R. B. Buxton, P. L. Carson, Biophysical Bases of Elasticity Imaging, *in* "Acoustical Imaging," volume 21, p. 223–240, Plenum Press, New York, 1995.
2. A. R. Skovoroda, A. N. Klishko, D. A. Gukasyan, E. I. Maevsky, V. D. Ermilova, G. A. Oranskaya, A. P. Sarvazyan, Quantitative analysis of the mechanical characteristics of pathologically altered soft biological tissues. *Biofizika* **40**, 1335–1340, (1995).
3. D. Hill, V. White, D. Jolley, K. Mapperson, Self examination of the breast: is it beneficial? Meta-analysis of studies investigating breast self examination and the extent of disease in patients with breast cancer. *Br. J. Med.* **297**, 271–275 (1988).
4. P. A. Newcomb, S. Weiss, B. E. Storer, D. Scholes, B. E. Young, Breast self examination in relation to the occurrence of advanced breast cancer. *J. Natl. Cancer Inst.* **83**, 260–265 (1991).
5. R. J. Dickinson, C. R. Hill, Measurement of soft tissue motion using correlation between A-scans. *Ultrasound Med. Biol.* **8**, 263–271 (1982).
6. M. Tristam, D. C. Barbosa, D. O. Cosgrove, D. K. Nassiri, J. C. Bamber, C. R. Hill, Ultrasonic study of *in vivo* kinetic characteristics of human tissue. *Ultrasound Med. Biol.* **12**, 927–937 (1986).
7. M. Tristam, D. C. Barbosa, D. O. Cosgrove, J. C. Bamber, C. R. Hill, Application of Fourier analysis to clinical study of patterns of tissue movement. *Ultrasound Med. Biol.* **14**, 695–707 (1988).
8. R. M. Lerner, S. R. Huang, K. J. Parker, "Sono-elasticity" images derived from ultrasound signals in mechanically vibrated tissues. *Ultrasound Med. Biol.* **16**, 231–239 (1990).

9. K. J. Parker, S. R. Huang, R. A. Musulin, R. M. Lerner, Tissue response to mechanical vibrations for "sonoelasticity imaging." *Ultrasound Med. Biol.* **16**, 241–246 (1990).

10. K. J. Parker, R. M. Lerner, Sonoelasticity of organs: shear waves ring a bell. *J. Ultrasound Med.* **11**, 387–392 (1992).

11. J. Ophir, I. Cespedes, H. Ponnekanti, Y. Yazdi, X. Li, Elastography: a quantitative method for imaging the elasticity of biological tissues. *Ultrason. Imaging.* **13**, 111–134 (1991).

12. B. S. Garra, E. I. Cespedes, J. Ophir, S. R. Spratt, R. A. Zuurbier, C. M. Magnant, M. F. Pennanen, Elastography of breast lesions: initial clinical results. Radiology **202**, 79–86 (1997).

13. R. Adler, J. M. Rubin, P. Bland, P. Carson, Characterization of transmitted motion in fetal lung: quantitative analysis. *Med. Phys.* **16**, 333–337 (1988).

14. M. O'Donnell, A. R. Skovoroda, B. M. Shapo, S. Y. Emelianov, Internal displacement and strain imaging using ultrasonic speckle tracking. *IEEE Trans. Ultrason. Ferroelectrics and Frequency Control* **41**, 314–325 (1994).

15. S. Y. Emelianov, M. A. Lubinski, W. F. Weitzel, R. C. Wiggins, A. R. Skovoroda, M. O'Donnell, Elasticity imaging for early detection of renal pathologies. *Ultrasound Med. Biol.* **21**, 871–883 (1995).

16. L. Axel, L. Dougherty, Heart wall motion: improved method of spatial modulation of magnetization for MR imaging. *Radiology* **169**, 59–63 (1988).

17. E. A. Zerhouni, D. M. Parish, W. J. Rogers, A. Yang, E. P. Shapiro, Human heart: tagging with MR imaging - a method for noninvasive assessment of myocardial motion. *Radiology* **169**, 164–172 (1988).

18. N. J. Pelc, M. Drangova, L. R. Pelc, Y. Zhu, D. C. Noll, B. S. Bowman, R. J. Herfkens, Tracking of cyclic motion with phase-contrast cine MR velocity data. *J. Magn. Reson. Imaging* **5**, 339–345 (1995).

19. J. B. Fowlkes, S. Y. Emelianov, J. G. Pipe, A. R. Skovoroda, R. S. Adler, P. L. Carson, A. P. Sarvazyan, Magnetic resonance imaging techniques for detection of elasticity variation. *Med. Phys.* **22**, 1771–1778 (1995).

20. R. Muthupillai, D. J. Lomas, P. J. Rossman, J. F. Greenleaf, A. Manduca, R. L. Ehman, Magnetic resonance elastography by direct visualization of propagating acoustic strain waves. *Science* **269**, 1854–1857 (1995).

21. R. Muthupillai, P. J. Rossman, J. F. Greenleaf, S. J. Riederer, R. L. Ehman, MR imaging of acoustic strain waves: initial *in vivo* results, *in* "Proc., ISMRM, 4th Scientific Meeting and Exhibition, 1996," New York, p. 475.

22. D. B. Plewes, I. Betty, S. N. Urchuk, I. Soutar, Visualizing tissue compliance with MR imaging. *J. Magn. Reson. Imaging* **5**, 733–738 (1995).

23. D. B. Plewes, G. Poole, M. Leitch, S. N. Urchuk, MR assessment of the viscoelastic properties of tissue through the propagation of transient strain waves, *in* "Proc., ISMRM, 4th Scientific Meeting and Exhibition, 1996," New York, p. 476.

24. I. Cespedes, J. Ophir, H. Ponnekanti, N. Maklad, Elastography: elasticity imaging using ultrasound with application to muscle and breast *in vivo*. *Ultrason. Imaging* **15**, 73–88 (1993).

25. A. Skovoroda, S. Emelianov, M. Lubinski, A. Sarvazyan, M. O'Donnell, Theoretical analysis and verification of ultrasound displacement and strain imaging. *IEEE Trans. Ultrason. Ferroelectrics and Frequency Control* **41**, 302–313 (1994).

26. A. Skovoroda, S. Emelianov, M. O'Donnell, Tissue elasticity reconstruction based on ultrasound displacement and strain images. *IEEE Trans. Ultrason. Ferroelectrics and Frequency Control* **42**, 747–765 (1995).

27. S. Y. Emelianov, A. R. Skovoroda, M. A. Lubinski, M. O'Donnell, Reconstructive Elasticity Imaging, *in* "Acoustical Imaging," volume 21, p. 241–253, Plenum Press, New York, 1995.

Three-dimensional static displacement stimulated-echo NMR strain imaging

THOMAS L. CHENEVERT, DEREK D. STEELE*, STANISLAV Y. EMELIANOV*§, AND ANDREI R. SKOVORODA§

Department of Radiology and Department of Biomedical Engineering; The University of Michigan, Ann Arbor, MI 48109-0553
Institute of Mathematical Problems of Biology, Russian Academy of Sciences; Pushchino, Russia §

INTRODUCTION

Elasticity MRI is the reconstruction of the elastic modulus in media using local displacement measurements of an object under static deformation [1], or directly from measurements of shear wave propagation [2]. Often it is assumed out of plane strain is approxiamtely zero. However, this plane strain state approximation does not hold in general. Estimates of the full 3D displacement and strain fields are required to accurately reconstruct elasticity. Here we describe such a method based on static displacement, stimulated-echo imaging [3]. As previously described, this approach encodes local displacement in response to an externally-applied deformation. A relatively long STE mixing time (200-300msec) allows ill-defined mechanical vibrations to dampen to where equilibrium conditions apply. The approach uses pulsed-field gradients (PFG) to encode displacement and is, in principle, readily extended to measure the full 3D displacement field.

METHODS

Features of the displacement-encoding STE technique have been described previously [3] but are summarized here. The initial spatial configuration of an elastic object is encoded by application of a PFG between the first two non-selective 90° rf pulses. An externally-applied deformation force transforms the object to a new configuration during the mixing time, TM, of the STE. The differential surface deformation can be relatively subtle ($\leq$5mm) and is chosen to complement the applied PFG area which defines displacement sensitivity (~3-16π/mm). Mixing time must be sufficient for the object to come to rest by the 3rd slice/slab-selective 90° rf pulse. A second PFG prior to signal readout yields a phase directly proportional to local displacement between initial and final object configuration. To achieve 3D, a fast-spin-echo train was appended to the STE with an additional centric-ordered z-slab phase-encode echo train (8-16 ETL on kz). Conventional phase-encoding was used for the remaining spatial dimension. Acquisition of data sets with inteleaved PFG gradients applied along X, Y, and Z axes: TR=1"; 256 x 128 x 8; 4ave; 3.8π/mm sensitivity. Phase correction was done via a sparse reference dataset (32 ky lines).

A tissue-mimicking block phantom containing ramped bars of harder material ($\approx$ 6x Young's modulus) was held between two pneumatic deformation plates. These parallel plates released a 5mm differential surface deformation during TM=270ms.

RESULTS

Images of the phantom shown in figure 1 are (a) magnitude and phase (i.e. displacement) images along (b) X, (c) Y and (d) Z directions. Corresponding strain images illustrated in figure 2 are (a) ε_{xx} , (b) ε_{yy} , (c) ε_{xy}, and (d) ($\varepsilon_{xx}+\varepsilon_{yy}$). Note, ($\varepsilon_{xx}+\varepsilon_{yy}$) should be zero if the plane-strain condition holds. Apparent structure in figure 2(d) indicates there is out of plane strain.

DISCUSSION

Extension of elasticity MRI to 3D is essential to implement a general elasticity reconstruction. 3D elasticity reconstruction algorithms have been described [1], but have not been implemented due to lack of suitable 3D data acquisition schemes. The method presented here represents an initial step toward that end.
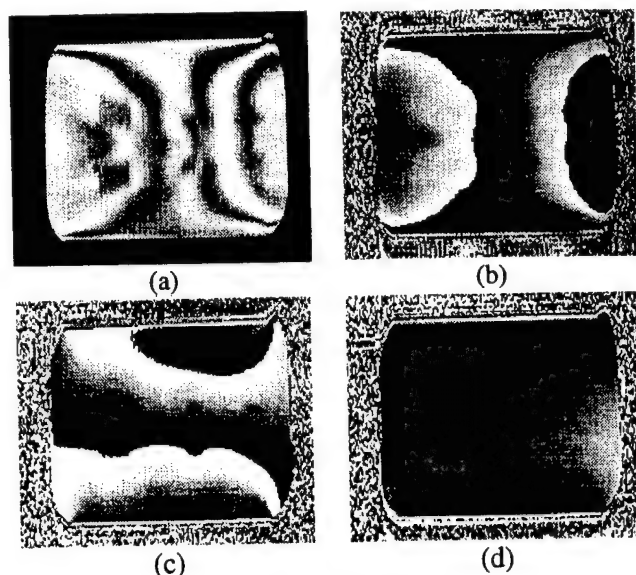

(a)   (b)   (c)   (d)

Figure 1

(a) ε_{xx} (b) ε_{yy} (c) ε_{xy} (d) $\varepsilon_{xx}+\varepsilon_{yy}$
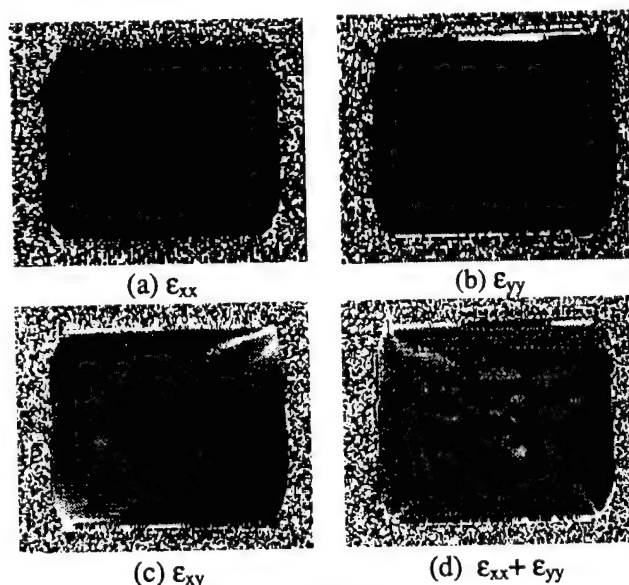
Figure 2

REFERENCES

1. A. Skovoroda, S. Emelianov, M. O'Donnell, Tissue elasticity reconstruction based on ultrasound displacement and strain images: IEEE Transactions on Ultrasonic Ferroelectrics and Frequency Control 1995; 42(4), pp747-765.

2. R. Muthupillai, D. J. Lomas, P. J. Rossman, J. F. Greenleaf, A. Manduca, R. L. Ehman, Magnetic resonance elastography by direct visualization of propagating acoustic strain waves. Science 269, 1854-1857 (1995).

3. Chenevert TL, Skovoroda AR, O'Donnell M, Emelianov SY. Elasticity reconstructive imaging by means of stimulated echo MRI. Magn Reson Med 1998; 39(3):482-490.

Three-dimensional static displacement, stimulated echo NMR elasticity imaging

Derek D Steele†, Thomas L Chenevert‡§, Andrei R Skovoroda‖ and
Stanislav Y Emelianov†‖

† Department of Biomedical Engineering, University of Michigan Medical Center,
3310 Kresge III, Ann Arbor, MI 48109-0553, USA
‡ Department of Radiology, University of Michigan Hospitals, 1500 E. Medical Center Drive,
Ann Arbor, MI 48109-0030, USA
‖ The Institute of Mathematical Problems of Biology, Russian Academy of Sciences, Pushchino,
Russia 142292

Abstract. This article presents a method for measuring three-dimensional mechanical displacement and strain fields using stimulated echo MRI. Additional gradient pulses encode internal displacements in response to an externally applied deformation. By limiting the mechanical transition to the stimulated echo mixing time, a more accurate static displacement measurement is obtained. A three-dimensional elasticity reconstruction within a region of interest having a uniform shear modulus along its boundary is performed by numerically solving discretized elasticity equilibrium equations. Data acquisition, strain measurements and reconstruction were performed using a silicone gel phantom containing an inclusion of known elastic properties. A comparison between two-dimensional and three-dimensional reconstructions from simulated and experimental displacement data shows higher accuracy from the three-dimensional reconstruction. The long-term objective of this work is to provide a method for remotely palpating and elastically quantitating manually inaccessible tissues.

1. Introduction

1.1. Motivation

Palpation has long been used by physicians as a means to detect disease. The underlying basis for this detection is the presence of 'hard' tissue. Evidence suggests that Young's (or shear) elastic moduli may differ by orders of magnitude within soft tissues in various physiological states (Sarvazyan *et al* 1995, Skovoroda *et al* 1995b). In addition, manual self-examination is the first diagnostic line of defence against both breast (Hill *et al* 1988, Newcomb *et al* 1991) and testicular cancers. With breast cancer, manual detection of a new mass often merits excisional biopsy, even if uncorroborated by other tests, as nodule hardness raises suspicion of malignancy (Foster 1996). Palpation of superficial lymph nodes and abdominal organs is also routinely performed. Although the touch of a skilled physician is a powerful diagnostic tool, palpation sensitivity is relatively poor within deep, dense or heterogeneous tissue. Thus, most manually detected lesions are either superficial, relatively large or both.

§ Author to whom correspondence should be addressed.

1.2. Elasticity imaging

Currently, many scientists are working on extending the range and sensitivity of palpation by using various methods to image tissue elasticity. The basic method for creating an elasticity map involves two steps. First, the internal displacements within tissue under an applied mechanical stress are measured. The (usually externally) applied deformation may be either dynamic or static. Then, from these data, a reconstruction of regional variations in tissue elasticity is performed, either directly or after calculating internal strains. Although both internal displacements and strains are related to the elastic properties of tissue, they are also strongly affected by geometry. Thus, some form of reconstruction is necessary to uniquely determine the elasticity distribution.

To date, two major medical imaging modalities have been used to measure tissue displacement: ultrasound and magnetic resonance imaging (MRI). The phase sensitivity of these methods lends itself to tracking tissue motion. Most elasticity imaging has been carried out using ultrasonically measured tissue displacements. These data have been obtained by tracking specular reflections (Dickinson and Hill 1982, Tristam *et al* 1986, 1988), by Doppler techniques (Lerner *et al* 1990, Parker *et al* 1990, Parker and Lerner 1992), by cross-correlation of acoustic echoes (Ophir *et al* 1991, Garra *et al* 1997) and by speckle tracking (Adler *et al* 1989, O'Donnell *et al* 1994, Emelianov *et al* 1995). Other efforts employ MRI for measuring tissue motion, as discussed below.

1.3. MRI measurement of tissue displacement

In the past, myocardial motion and strain have been measured using spatial magnetization tagging (Axel and Dougherty 1989, Zerhouni *et al* 1988), and phase-based velocity encoding (Pelc *et al* 1995). More recently, methods have been devised to measure tissue displacement specifically for elasticity imaging. These measurements can be separated based upon the nature of the applied deformation.

1.3.1. Dynamic deformation.   With these methods, a periodic excitation is applied to the tissue near the region of interest, and the entire system may be allowed to reach steady state. One or several 'snapshots' of mechanical wave propagation within the object are produced by controlling the relative phase between the mechanical excitation and the motion-encoding gradients. The local displacement information in these images is then used as an input for an elasticity reconstruction algorithm. Initial experiments used a shear excitation, and the elasticity reconstruction was performed assuming the recorded image contained only shear waves (Muthupillai *et al* 1995). If only shear waves are present in a purely elastic medium, local elastic modulus variations are determined via the relation $\mu = \nu^2 \lambda^2 \rho$, where μ is the local shear modulus, ν is the frequency of the applied deformation, λ is the measured local strain-wave wavelength and ρ is the density of the medium. Although attractive in its simplicity, this approach is compromised by frequency-dependent viscoelastic effects and strain-wave wavelength, interference from reflections off of elastic inhomogeneities and the possible presence of longitudinal mechanical waves in the medium. Despite these limitations, this method has been applied *in vivo* (Dresner *et al* 1999, Lawrence *et al* 1999). Recently, a more general elasticity reconstruction from a series of 'instantaneous' steady state mechanical wave images has been developed (Sinkus *et al* 1999, 2000). This and another technique (Van Houten *et al* 1999, Weaver *et al* 1999) rely on a more complete viscoelastic tissue model than that presented in Muthupillai *et al* (1995).

1.3.2. Static deformation. Another method of producing an internal strain field in an object is to deform it and allow the material to relax to equilibrium before measuring the displacement field. The displacement field has been accessed using spatial magnetization tagging, but this method suffers from spatial resolution limited by the tagged grid size and typically measures only two-dimensional (2D) motion (Fowlkes *et al* 1995). A quasistatic method using bipolar gradient phase encoding of 2D motion is presented by Plewes *et al* (1995, 1996). Stimulated echo MRI has also been used to measure 2D displacement fields (Reese *et al* 1996), from which elasticity images have been reconstructed (Chenevert *et al* 1998). This method has been extended to study myocardial motion (Aletras *et al* 1999b). With these techniques, viscoelastic effects are generally ignored, making the reconstruction more straightforward. Care must be taken, however, to justify the use of a static model, especially when repeated deformations are needed to acquire a complete data set.

In general, MRI has several advantages over ultrasound with respect to elasticity imaging. Although ultrasound accurately measures motion along the beam axis, lateral motion is measured with a resolution given by the depth-dependent beam width. Out-of-plane motion is generally not considered, given the problems with three-dimensional (3D) image registration in ultrasound. These restrictions compromise the quality of displacement data available and constrain the type of model used to produce an elasticity image. Ultrasound does, though, offer the advantages of low-cost and real-time imaging. MRI, on the other hand, gives one the ability to measure 3D displacements within an object, and does this at a higher overall resolution than clinical ultrasound.

In this paper we present a method for encoding the full 3D displacement field within an object undergoing an externally applied static (or quasistatic) deformation. Local strain estimates are calculated from the measured displacements, and the strain tensor is used to numerically solve differential elasticity equilibrium equations, ultimately producing a 3D elasticity image.

2. Reconstructive elasticity imaging from static displacement fields

The goal of elasticity imaging is to produce a map of the tissue elastic modulus in a region of interest using available measurements of displacement components. In this work, the reconstruction approach taken is based upon a model of linear, elastic, isotropic media (Skovoroda *et al* 1995a, 1999). The central equations and concepts are covered briefly here. A more detailed discussion can be found in the references mentioned. Note that some tissues, such as skeletal muscle, exhibit anisotropic elasticity (Fung 1993). For anisotropic media, a more generalized reconstruction method is needed.

2.1. Linear elasticity and reconstruction

In linear elasticity, the components of the strain (ε_{ij}) and stress (σ_{ij}) tensors in a medium undergoing small deformations are given by

$$\varepsilon_{ij} = \frac{1}{2}\left(\frac{\partial u_i}{\partial x_j} + \frac{\partial u_j}{\partial x_i}\right) \tag{1}$$

$$\sigma_{ij} = p\delta_{ij} + 2\mu\varepsilon_{ij} \tag{2}$$

where u_i is a component of the displacement vector $U = (u_1, u_2, u_3)$ in Cartesian coordinates $r = (x_1, x_2, x_3)$, p is the product $\lambda\nabla \cdot U$ for compressible media or the static internal pressure for incompressible media, δ_{ij} is the Kronecker delta function, λ and μ are the Lamé coefficients and $\mu = \mu(r)$ is the shear elastic modulus.

A medium undergoing static deformation obeys the equilibrium condition:

$$\sum_{j=1}^{3} \frac{\partial \sigma_{ij}}{\partial x_j} + f_i = 0 \qquad i = 1, 2, 3 \tag{3}$$

where f_i is the body force per unit volume acting in the x_i direction. In addition, if a medium is incompressible, volume conservation leads to the following relation:

$$\nabla \cdot U = \varepsilon_{11} + \varepsilon_{22} + \varepsilon_{33} = \frac{\partial u_1}{\partial x_1} + \frac{\partial u_2}{\partial x_2} + \frac{\partial u_3}{\partial x_3} = 0. \tag{4}$$

Although not necessary in the development that follows, soft tissue is approximately incompressible (Sarvazyan *et al* 1995).

Using equations (1) and (2) in (3), the unknown $p(r)$ can be eliminated to yield a set of differential equations depending only on U, first- and higher-order spatial derivatives of U, and the elasticity distribution, $\mu(r)$. This set of equations is then numerically solved to estimate the unknown shear elasticity distribution.

2.2. Importance of three-dimensional reconstruction methods

Several approaches have been proposed to estimate tissue elasticity from the experimentally measured spatial distribution of internal displacements within an object. The simplest method is a one-dimensional (1D) estimation of normalized tissue elasticity, expressed as

$$\kappa_1 = 1/\varepsilon \tag{5}$$

where ε is longitudinal strain (Ophir *et al* 1991, Garra *et al* 1997). Indeed, a loaded object generally exhibits low longitudinal strain in relatively hard regions and high longitudinal strain in relatively soft regions.

A 2D elasticity reconstruction, based on a plane-strain assumption and all necessary in-plane strain components, provides a more accurate representation of the object's elasticity (Skovoroda *et al* 1995a, 1999). The theory of reconstructing clearly bounded and spatially distributed tissue inhomogeneities has been demonstrated by Skovoroda *et al* (1995a) as well. However, inaccurate estimates may result by using either a 1D or 2D reconstruction of a 3D object.

To demonstrate these inaccuracies, consider a spherical inclusion of radius R in a uniaxially, uniformly loaded, infinite, homogeneous medium (Goudier 1933). For an incompressible medium, the distribution of longitudinal strain along the x_3 axis (orthogonal to the applied deformation), is (Skovoroda *et al* 1994):

$$\varepsilon = \begin{cases} \dfrac{5\beta}{3 + 2\kappa_0} & x_3 \leqslant R \\[2ex] \beta \left\{ 1 + \dfrac{\kappa_0 - 1}{2(3 + 2\kappa_0)} \left[5\left(\dfrac{R}{x_3}\right)^3 - 9\left(\dfrac{R}{x_3}\right)^5 \right] \right\} & x_3 > R. \end{cases} \tag{6}$$

Here β is the magnitude of the applied strain and $\kappa_0 = \mu/\mu_0$ is the ratio of the inclusion to background shear moduli. Normalizing (6) by β, which corresponds to the axial strain in the tissue far from the inclusion, and substituting into (5) we obtain

$$\kappa_1 = \begin{cases} \dfrac{3 + 2\kappa_0}{5} & x_3 \leqslant R \\[2ex] (3 + 2\kappa_0) \left\{ 3 + 2\kappa_0 + \dfrac{\kappa_0 - 1}{2} \left[5\left(\dfrac{R}{x_3}\right)^3 - 9\left(\dfrac{R}{x_3}\right)^5 \right] \right\}^{-1} & x_3 > R. \end{cases} \tag{7}$$

Note that $\kappa_1/\kappa_0 = (3 + 2\kappa_0)/5\kappa_0$ within the inclusion. That is, for a very hard inclusion (κ_0 large), the relative modulus obtained from a 1D reconstruction will only be 40% of
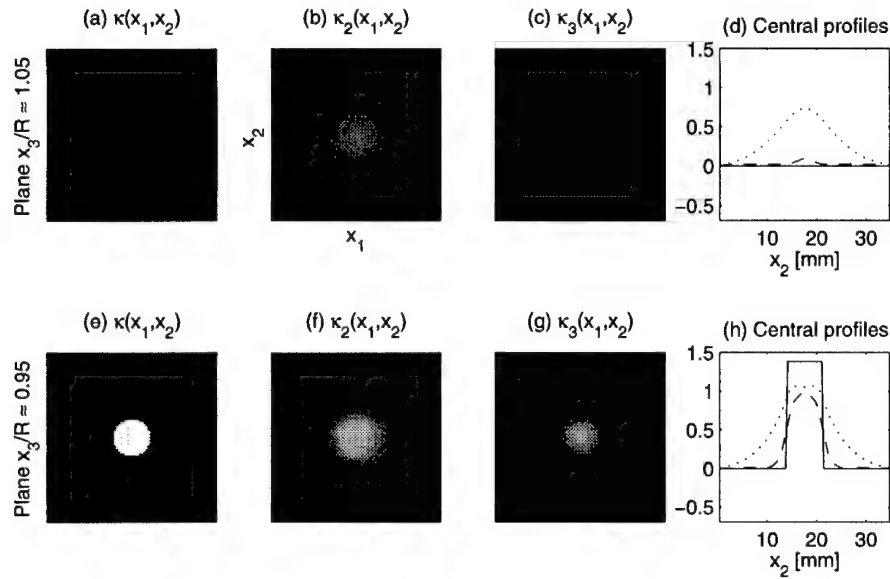
Figure 1. Simulated elasticity distributions, $\kappa(x_1, x_2)$, and corresponding 2D, $\kappa_2(x_1, x_2)$ and 3D, $\kappa_3(x_1, x_2)$, elasticity reconstructions from the $x_3/R \approx 1.05$, (*a*)–(*d*), and $x_3/R \approx 0.95$, (*e*)–(*h*), planes of a phantom with a single hard, spherical inclusion of radius R. Also presented are the central vertical profiles of each distribution, where (———) is κ, ($\cdots\cdots$) is κ_2, and (- - - -) is κ_3. All are presented on a log scale where black corresponds to a relative shear modulus of 0.5 and white to 4.5. The background has a relative shear modulus of 1, and the inclusion, 4.

its actual value. On the other hand, for a soft inclusion (κ_0 small), the relative modulus estimate will approach $\frac{3}{5}$, *no matter how much softer the inclusion is than the background*. Obviously, the inaccuracy of a 1D elasticity estimation may not be acceptable for many applications.

Now consider a 2D reconstruction. Figures 1(*a*) and (*e*) show the exact relative elasticity distribution, $\kappa(x_1, x_2)$, for two infinitesimal planes in our pedagogic phantom with $\kappa_0 = 4$. Figure 1(*a*) presents κ for $x_3/R \approx 1.05$, that is, outside of the inclusion, while figure 1(*e*) is the $x_3/R \approx 0.95$ plane. The corresponding relative 2D reconstructions, $\kappa_2(x_1, x_2)$, are shown in figures 1(*b*) and (*f*). The reconstructions were performed using the algorithm presented by Skovoroda *et al* (1999). For comparison with experimental results (see section 5), an analytic model was used to generate displacement data which were sampled with the x_2 resolution of the experimental displacement encoded data discussed in section 4.2. The strains used as input for the reconstructions were calculated as described in section 4.3, and the reconstructions were performed over a region of interest identical to the one discussed in that same section. The positions of the two reconstructed planes were selected to approximately correspond to the experimental planes considered in section 5. As evidenced here, neglecting out-of-plane strain components in the reconstruction produces geometrical distortions in the elasticity image. Specifically, the spherical inclusion is reconstructed as a prolate spheroid. The inaccuracy of a plane-strain based reconstruction is small near the central plane, and increases with the distance between the imaging plane and the centre of the inclusion. Far from the inclusion, a 2D reconstruction would again be accurate.

It is clear that a 1D or 2D reconstruction may lead to significant inaccuracies in tissue elasticity estimations, especially when complicated *in vivo* geometries influence displacement and strain measurements. This points to the need for an accurate 3D elasticity reconstruction. A general unknown shear elasticity distribution, $\mu(x_1, x_2, x_3)$, must satisfy the equation (Skovoroda *et al* 1995a, 1999):

$$\frac{\partial^2(\mu\varepsilon_{12})}{\partial x_1^2} - \frac{\partial^2(\mu\varepsilon_{12})}{\partial x_2^2} + \frac{\partial^2[\mu(\varepsilon_{22} - \varepsilon_{11})]}{\partial x_1 \partial x_2} + \frac{\partial^2(\mu\varepsilon_{23})}{\partial x_1 \partial x_3} - \frac{\partial^2(\mu\varepsilon_{13})}{\partial x_2 \partial x_3} = 0. \quad (8)$$

Thus, in order to compute all the necessary components of the strain tensor, ε_{ij}, in (8), all of the displacement components (u_1, u_2, u_3) must be measured as a function of spatial coordinates (x_1, x_2, x_3). This requirement exists in both the differential-based 3D reconstruction (8), as well as in the more stable integral based 3D approach (Skovoroda *et al* 1999).

The 3D elasticity reconstructions from the two planes previously discussed are shown in figures 1(c) and (g). The reconstruction was performed as discussed in section 4.3. Although not perfect due to the relatively large x_3 step size, the 3D reconstructions clearly exhibit fewer geometric distortions than the 2D estimates. This is particularly well illustrated by the central vertical profiles through the analytic, 2D, and 3D shear distributions presented in figures 1(d) and (h). In the $x_3/R \approx 1.05$ plane, the 2D reconstruction estimates that an inclusion is present, when indeed it is not, while the 3D reconstruction shows little evidence of the presence of an inclusion. The estimate of the extent of the inclusion in the $x_3/R \approx 0.95$ plane is also improved over the 2D estimate. As with the 2D reconstructions, the strain data and reconstruction parameters used for the 3D reconstruction were identical to those of the experimental parameters described in sections 4.2, 4.3 and 5.

3. Static displacement measurement via stimulated echo MRI

Static displacement measurements for elasticity imaging avoid several confounding factors that may be present if dynamic displacement measurements are used. Since shear wave propagation speed in soft tissue is approximately $1–20$ m s^{-1}, shear waves launched into a medium by an applied deformation may require tens of milliseconds to traverse an object approximately 100 mm in size. Reflected waves may take much longer to dampen. To appropriately measure an object's internal static displacements, the object must be in mechanical equilibrium—that is, it must satisfy (3)—during both the pre- and post-deformation measurements. A stimulated echo MRI sequence using displacement encoding gradient pulses is employed to achieve this (Reese *et al* 1996, Chenevert *et al* 1998). Figure 2 presents a schematic of this pulse sequence. The mechanical transition from the pre- to post-deformational states occurs during the stimulated echo mixing time, T_M. Because the relevant magnetization is longitudinal during T_M, it is unaffected by the object's motion during the mechanical transition period. This allows a more accurate measurement of static internal displacement. Additionally, precise synchronization of the motion and applied gradients is not necessary as long as the mechanical deformation begins after the second radio-frequency pulse, and internal motion stops before the third. A long delay in the echo time, T_E, could also be used to let the object reach equilibrium, but this would likely lead to prohibitive signal loss from T_2 decay.

Local displacements are encoded in the magnetization's phase via pulsed-field gradients. The displacement sensitivity, in radians/distance, of the sequence is

$$\Phi_d = \gamma \int_0^\tau G_d(t) \, dt = \gamma G_d \tau \quad (9)$$

where γ is the gyromagnetic ratio of the proton, $G_d(t)$ is the encoding gradient waveform and τ is the duration of the encoding gradient. However, for accurate displacement measurements,
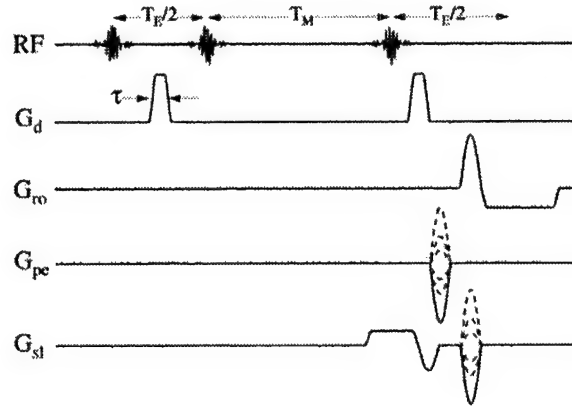
Figure 2. Displacement encoding, stimulated echo pulse sequence waveforms. RF = radio frequency, G_d = displacement encoding gradient, and G_{ro} = read-out (x_1), G_{pe} = phase-encode (x_2) and G_{sl} = slice (x_3) directed gradient waveforms. T_M is the mixing time, T_E is the echo time and τ is the duration of the displacement encoding gradient. Note that the displacement encoding gradient may be applied to any of the directional waveforms.

phaseshifts unrelated to the applied deformation must be removed. This is done by acquiring a phase reference data set using the same pulse sequence, but with the object maintained in the post-deformational state for the entire experiment. Note that all spatial encoding takes place with the object in the post-deformational state for both the displacement encoded and reference acquisitions. Therefore no image registration or tracking algorithms are required to use the reference data, S_r, to correct the displacement encoded data, S_d. The corrected data set, S_c, is then:

$$S_c(r) = \frac{S_d(r)S_r(r)^*}{|S_r(r)|} \approx |S_d(r)|\, e^{i\phi(r)}. \tag{10}$$

Most sources of phase error, such as static field inhomogeneities, tend to be slowly varying functions of position. Thus the phase reference data may be acquired at relatively low spatial resolution to reduce scan time.

The unwrapped phase of (10) is related to the local displacement vector, U, via

$$\phi(r) = \Phi_d \cdot \Delta r = \Phi_d \cdot U(r) \tag{11}$$

where Δr is the local displacement from pre- to post-deformational states. The displacement sensitivity, Φ_d, may be made sensitive to motion in an arbitrary direction based upon appropriate combination of displacement encoding gradients in the read-out, phase-encode and slice directions. Hence, this pulse sequence readily extends to acquiring three-dimensional displacement data.

4. Methods

4.1. Phantom

Elasticity imaging experiments were performed on a phantom with a spherical hard inclusion. Semicosil 921 silicone gel (Wacker Silicones Corporation, Adrian, MI) was used to construct a phantom qualitatively simulating the mechanical properties of soft tissue. The Semicosil 921

consists of two components, A and B, wherein different ratios of these components are used to vary the mechanical properties of the gel. A tissue-mimicking phantom was constructed in several steps. First, background material was prepared by thoroughly mixing components A and B in a 1:1 ratio, and then pouring the mixture into a 154 mm by 80 mm rectangular mould. The mixture was degassed and cured for 24 h at room temperature to produce a 22 mm thick layer. Then a 25 mm diameter hard sphere was prepared from a 1:2.5 mixture of A and B and was placed on top of the layer in the middle of the mould. Finally, another batch of background material (1:1 ratio) was poured into the mould resulting in a 64 mm by 80 mm by 154 mm phantom with a single, hard, spherical inclusion roughly in the centre. At the same time, three samples of each batch were taken to independently assess the elasticity contrast between the inclusion and surrounding materials. These measurements were performed using the force-deformation system described in Erkamp *et al* (1998), and showed that the inclusion was four times harder than the background, and that both background materials were elastically equivalent.

4.2. Data acquisition

To provide repeatable deformation, the phantom was placed under moderate pre-load pressure between two acrylic plates in a pneumatically driven device. Air-filled neoprene boots in a push–push configuration provided the necessary force to the top plate to keep the phantom in this pre-load state, and aided the vertical recoil of the phantom to the post-deformation state. Pneumatic pressure was delivered via two solenoid valves whose timing was controlled by an external transistor–transistor logic circuit triggered by the pulse sequence. Quick-release valves aided in depressurizing the boots. Both the pre-load and recoil positions of the top acrylic plate were set by adjustable stops; the bottom plate's position was fixed. The applied vertical deformation was approximately 2.4 mm, or about 6% strain, between the pre-transition (greater deformation) and post-transition (less deformation) states.

During data acquisition, the displacement encoding gradient pulse duration, τ, was 1.5 ms, and the amplitude, G_d, was 40 mT m^{-1} in the read-out (x_1) and phase-encode (x_2) directions, and 60 mT m^{-1} in the slice (x_3) direction. Here, the x_3 direction was along the bore's axis, and the x_1 and x_2 directions were perpendicular to x_3 in the horizontal and vertical directions respectively. By (9), the displacement sensitivity, Φ_d, was approximately 5.11 π mm^{-1} in the x_1 and x_2 directions, and about 7.66 π mm^{-1} in the x_3 direction. The displacement encoding direction was cycled each pulse repetition between the x_1, x_2 and x_3 directions. The pulse-to-pulse repetition time was approximately 0.98 s, the mixing time (T_M) was 270 ms, and the echo time (T_E) was 45 ms. Two averages were taken of a 256 × 256 × 32 matrix covering an 80 mm by 110 mm by 48 mm field of view. The phase reference data were collected using a 256 × 32 × 32 matrix while keeping all other parameters the same. All experiments were performed on a 2 T, 18 cm bore MRI system (Bruker, formerly GE NMR Instruments) using a 150 mm transmit/receive birdcage coil.

4.3. Data processing

All time-domain data were transferred off-line for processing. For phase correction, the phase reference data set was zero-filled to a 256 × 256 × 32 matrix. Then this and the displacement encoded data were 3D Fourier transformed and corrected as in (10). The resulting phase maps were then used to estimate the spatial derivatives to compute the strains, via (1), necessary for the elasticity reconstruction. Phase unwrapping of the displacement data was not strictly required since only phase derivatives were used in the strain calculations. The displacement

derivative at the ith point in the j direction was computed from the angle of the complex multiplication of the $i + 1$th point with the conjugate of the $i - 1$th point, then scaling by $1/2\Phi_d^j$, where Φ_d^j is the magnitude of the displacement sensitivity in the j direction. For convenience, the strain data were decimated to the x_2 step size in each x_3 plane in order to have equal resolution in both the x_1 and x_2 directions. The strain images were then median filtered with a 5×5 window, resulting in a slight decrease in spatial resolution. These strains were used as input for the elasticity reconstruction.

The 3D elasticity reconstruction was performed using the least-squares error minimization algorithm discussed in Skovoroda *et al* (1999), with a second-order, one-sided finite derivative approximation in the x_3 direction. The reconstruction of $\mu(r)$ is a boundary value problem, therefore a unique solution is obtained only with boundary conditions. So a square 35 mm by 35 mm region of interest, which contained the inclusion in several x_3 planes, was identified in the x_1 and x_2 directions. Along the boundaries of these regions, and in the two x_3 planes furthest from the centre of the inclusion (which did not contain the inclusion), the value of the shear modulus was set to 1, resulting in a relative shear modulus reconstruction.

5. Results

Representative magnitude and corrected phase images of the Semicosil phantom for a 1.5 mm thick plane centred about $x_3 = 0.75$ mm, or $x_3/R \approx 0.05$, are shown in figure 3. Knowing that $\Phi_d \approx 5.11 \pi$ mm^{-1} in the x_1 and x_2 directions, the number of 2π phase wraps in figure 3(c)
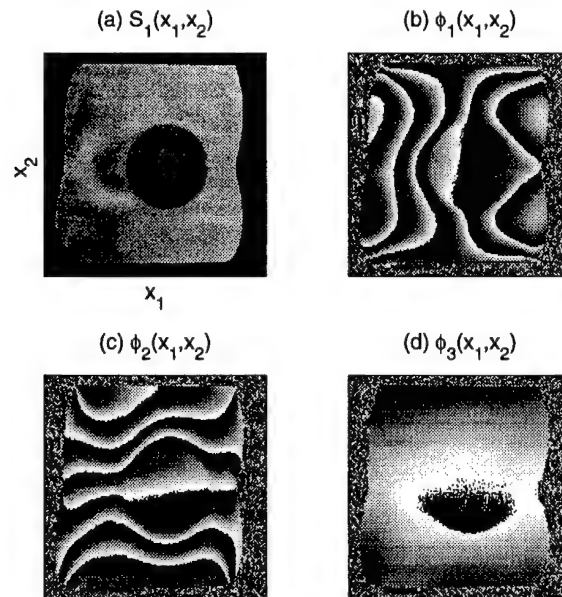

Figure 3. Representative magnitude and phase images from the $x_3/R \approx 0.05$ plane of the 3D displacement encoded data set from a phantom with a single, hard, spherical inclusion. S_1, (a), is the magnitude of the x_1-displacement encoded data, and ϕ_i, (b)–(d), are the phase images of the x_i-displacement encoded data.
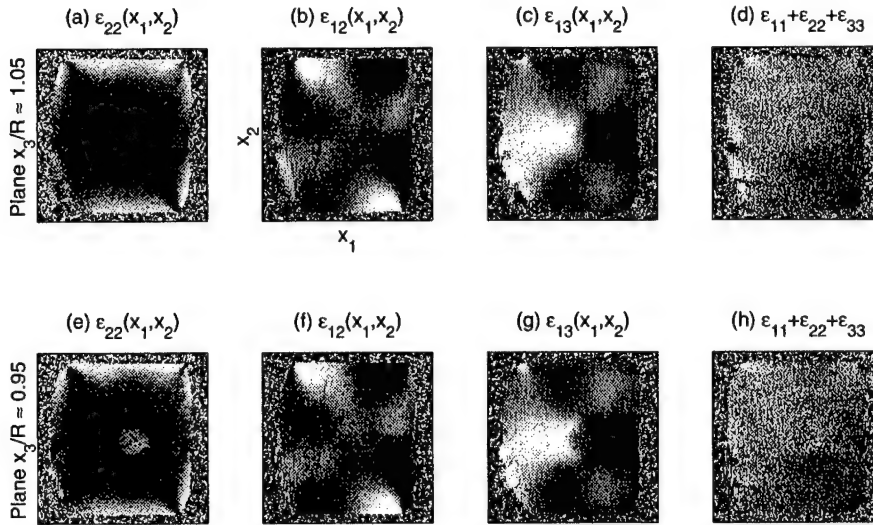
Figure 4. Representative strain images from the $x_3/R \approx 1.05$, (a)–(d), and $x_3/R \approx 0.95$, (e)–(h), planes from the 3D displacement encoded data of the phantom with a single, hard, spherical inclusion. One normal strain, ε_{22}, the in-plane shear strain, $\varepsilon_{12} = \varepsilon_{21}$, one through-plane shear strain, $\varepsilon_{13} = \varepsilon_{31}$, and the trace of the strain tensor, $\varepsilon_{11} + \varepsilon_{22} + \varepsilon_{33}$, are presented for each plane. The lack of features in (d) and (h) indicate that the phantom is nearly incompressible. Linear scales for each image are, from black to white: (a), (e): [−6%, 0%]; (b), (f): [−2.5%, 2.5%]; (c), (d), (g), (h): [−1.6%, 1.6%].

indicates a vertical deformation of approximately 2.3 mm, and those in figure 3(b) a horizontal deformation of about 2.0 mm. Reduced phase slope in the region of the hard inclusion is clearly visible in these figures as well. Due to the central location of this plane, there is little feature in ϕ_3 (part (d)).

Figure 4 shows representative strain maps from the planes centred around $x_3 = 15.75$ mm and $x_3 = 14.25$ mm. Due to the loaded state of the phantom during imaging, the sphere became prolate, therefore these planes correspond to the $x_3/R \approx 1.05$ and $x_3/R \approx 0.95$ locations respectively. One normal strain, ε_{22} (parts (a) and (e)), the in-plane shear strain, $\varepsilon_{12} = \varepsilon_{21}$ (parts (b) and (f)), and one through-plane shear strain, $\varepsilon_{13} = \varepsilon_{31}$ (parts (c) and (g)), are shown for each plane. These components are all required to perform the elasticity reconstruction in (8). Note that the presence of through-plane strains in (8) necessitates measurement of the full 3D displacement field. In addition, although elasticity-specific details are seen in the strain maps, features related to geometry and the applied deformation are also clearly present. This points to the need for a proper elasticity reconstruction to disentangle these factors. Also shown is the trace of the strain tensor, $\varepsilon_{11} + \varepsilon_{22} + \varepsilon_{33}$, for each plane (parts (d) and (h)). The relative lack of features in the trace of the strain tensor indicates that the phantom is nearly incompressible (like soft tissue).

Magnitude images of the 35 mm by 35 mm regions of interest in the same two planes, along with two different shear modulus reconstructions of these planes, are presented in figure 5. In the magnitude images, the hard inclusion is clearly present in the $x_3/R \approx 0.95$ plane, while it is essentially absent in the $x_3/R \approx 1.05$ plane. Note that the magnitude images only convey geometric information. Figures 5(b) and (f) show 2D elasticity reconstructions of these
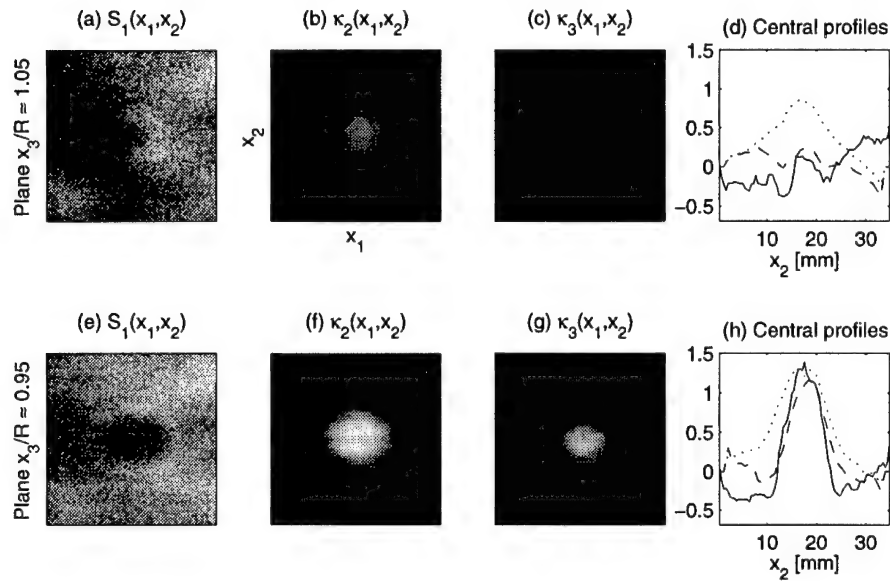
Figure 5. x_1-displacement encoded magnitude images, $S_1(x_1, x_2)$, and corresponding 2D, $\kappa_2(x_1, x_2)$, and 3D, $\kappa_3(x_1, x_2)$ elasticity reconstructions from the $x_3/R \approx 1.05$, (a)–(d), and $x_3/R \approx 0.95$, (e)–(h), planes of a phantom with a single hard, spherical inclusion. Also presented are the central vertical profiles of each distribution, where ($\cdots\cdots$) is κ_2, and (- - - -) is κ_3. All are presented on a log scale where black corresponds to a relative shear modulus of 0.5 and white to 4.5. The background has a relative shear modulus of 1, and the inclusion, 4, from independent measurements. For geometric reference purposes, parts (d) and (h) include plots of S_1^{-1} (filtered and normalized) as (———).

two planes, while figures 5(c) and (g) show the corresponding 3D elasticity reconstructions. As in figure 1, one sees an overestimate of the 3D spatial extent of the inclusion in the 2D reconstructions. This overestimate is corrected with the 3D reconstruction. For ease of comparison, vertical profiles through the centre of the inclusion from the 2D and 3D reconstructions are presented, along with plots of S_1^{-1} for geometric reference, in figures 5(d) and (h).

6. Discussion

The stimulated echo sequence presented here phase encodes internal displacements using gradient pulses. An externally applied deformation, synchronized with the pulse sequence, produces an internal displacement field. This deformation is actively driven with a pneumatic device, and the mechanical transition from pre- to post-deformation occurs during the sequence mixing time, T_M, while the relevant magnetization is longitudinal. Because longitudinal magnetization decays only as T_1, the mechanical transition period may be extended to allow potentially long-lived or ill-defined motions within the object to dampen. With a sufficiently long T_M, the encoded displacement will be approximately static. However, signal loss due to T_1 relaxation sets a practical limit on the length of T_M. To determine an appropriate mixing time, a series of 2D displacement encoded images was taken, varying T_M from 50–750 ms.

From the phase maps of these data, one could see that the top acrylic plate of the deformation device completed its excursion in under 200 ms, and the internal motion in the phantom became negligible by 250 ms. To ensure that (3) was reasonably satisfied, a 270 ms mixing time was chosen for subsequent data collection. Although the deformation device used here provides adequate transition speed, an even faster device would allow a shorter T_M, yielding more signal. While absent in the phantom used here, water diffusion in the presence of displacement encoding gradients will be another source of signal loss in *in vivo* experiments. This loss can be mitigated by reducing the displacement sensitivity, Φ_d, or by shortening T_M.

The quality of the shear modulus reconstruction ultimately depends on the local phase, as in (11), induced by the encoding gradients and the local displacement. More specifically, the quality depends on the spatial derivatives of the encoded phase. A study of the effects of displacement sensitivity, applied deformation, relative hardness and diffusion loss on the signal-to-noise ratio (SNR) of the elasticity reconstruction has been presented in Steele *et al* (1999). This study demonstrates that increased intra-voxel phase wrap will increase the reconstruction SNR, up to a π intra-voxel phase distribution. Note that the reconstruction SNR increases despite a reduction in the nuclear magnetic resonance (NMR) signal from the object. Assuming a linear phase distribution of θ radians across a voxel, the signal modulation from that voxel will be $|\mathrm{sinc}(\theta/2)| = |\sin(\theta/2)(\theta/2)^{-1}|$. However, the phase gradients (that is, the displacement derivatives) will be maximized without aliasing as the intra-voxel phase wrap approaches π, and this is the signal that is important in the reconstruction. A π phase wrap may be achieved through many combinations of applied deformation and displacement sensitivity. However, increasing Φ_d will increase signal loss due to diffusion, as discussed above. Hence, a smaller displacement sensitivity and increased deformation would appear to be optimal. Again, there is a trade-off: as deformation increases, the model of linear elasticity discussed in section 2.1 will become less and less valid. Elasticity reconstructions from finite displacement fields have been demonstrated in Skovoroda *et al* (1999), but these are obviously more computationally intensive than the linear reconstructions used here. In relation to the data presented here, the number of 2π phase bands across the phantom in figure 3 clearly indicate that these data were acquired with a suboptimal displacement sensitivity/applied deformation combination. Because neither the encoding nor the deformation used here were extreme, the elasticity reconstruction's SNR should be improved merely by optimizing the intra-voxel phase wrap.

Relative hardness, object geometry and deformation geometry also affect the displacement phase gradients. In general, the phase gradients increase near soft/hard interfaces and are higher in relatively soft regions of tissue. Excessive phase wrap (i.e. strain) can lead to regions of significant signal loss in a manner analogous to flow dephasing in conventional MRI. The resulting reconstructions would suffer from this signal loss. Hence, the applied deformation and displacement sensitivity should be optimized for the regions of highest strain in an object. Increased intra-voxel phase wrap in regions of lower strain may be obtained by integrating the signal from several voxels; in essence, applying an adaptive voxel size based upon local phase gradients. This increase in signal would come at the expense of spatial resolution. Additionally, signal loss due to intra-voxel phase wrap in the displacement encoded magnitude images may be useful for identifying regions of high strain in tissue.

Another factor affecting the displacement signal is the reproducibility of the applied deformation. For multistep acquisitions, such as those presented here, good deformation reproducibility is essential. Variations in the applied deformation will lead to phase instability, motion-like artefacts, and errors that will propagate through the elasticity reconstruction. Adequate reproducibility has been achieved with the current deformation system. However, irreproducible or asynchronous motions within the imaged object may be problematic.

These would include physiological cardiac and respiratory motion present in *in vivo* experiments. In some ways, the problems associated with undesired motion would be similar to those encountered in diffusion MRI. Because the applied deformation is external, though, the displacement encoding can be tailored to it, reducing the effect of undesired motion on the displacement data. Further complications arise because phase derivatives of the displacement data, approximated by finite differences, are required for reconstruction. In addition to choosing an appropriate deformation/encoding combination, methods should be devised to reduce the effects of undesired motion on the displacement derivatives.

Clearly several advantages justify performing a 3D elasticity reconstruction rather than a 2D reconstruction. As illustrated in figures 1 and 5, and as discussed in sections 2.2 and 5, a 3D reconstruction provides a more accurate representation of the elasticity distribution than a 2D reconstruction in the simple phantom used here. Complicated *in vivo* geometries will only increase the likelihood that neglecting out-of-plane strain components will result in an inaccurate elasticity estimate. This increased accuracy comes, though, at the expense of increased computational complexity and increased scan time. For instance, a single acquisition of the 3D data discussed in section 4.2 takes over 6 h! This far exceeds any clinically feasible scan times. The total experiment time may be lessened through the use of echo-planar imaging (Mansfield 1977) or fast spin-echoes (Hennig *et al* 1986) for spatial encoding (Chenevert *et al* 1999). A fast scan implementation has already been used to study cardiac motion (Aletras *et al* 1999a). The number of planes of data acquired may also be significantly reduced while still allowing a 3D reconstruction, shortening the scan time further. It should be mentioned that a classic 3D stimulated echo sequence was deliberately chosen in part due to SNR considerations, since a fast scan implementation of the method would generally have a lower SNR than one classically phase encoded. Being an inverse problem, the 3D reconstruction is sensitive to the SNR, and we wanted the initial test of the reconstruction to be done with the highest SNR data possible using this technique. Also, note that the reconstruction in (8) does not rely on the assumption of incompressibility, although making this assumption provides another means of regularizing the inverse problem.

Additionally, a reconstruction of static displacement data offers several advantages over a reconstruction of dynamic displacement data. A static reconstruction allows one to ignore viscoelastic effects as well as the longitudinal or shear nature of the applied deformation. Static methods also provide high SNR displacement and strain estimates. Dynamic methods, on the other hand, provide a potentially very simple reconstruction (Muthupillai *et al* 1995). However, this reconstruction may be compromised by interference from elastic inhomogeneities, attenuation of shear waves, mixing of longitudinal and shear waves, and resolution limits imposed by noise when determining the shear-wave wavelength. Reconstruction models that include viscoelastic effects allow a more accurate interpretation of dynamic data (Sinkus *et al* 1999, 2000, Van Houten *et al* 1999), but these are necessarily more complicated than static models (Skovoroda *et al* 1995a, 1999).

Choosing a contour of constant shear modulus for appropriate boundary conditions for (8), though, can in practice be a challenge. In the applications discussed here, *a priori* knowledge of phantom geometry was employed in the reconstructions. This may be possible *in vivo* as well, albeit more complicated. For instance, in breast elasticity imaging, such a contour may be defined in the subcutaneous fat surrounding the parenchyma using the boundary detection procedure described in Skovoroda *et al* (1995a). The elasticity reconstruction would then be relative to the shear modulus of the fat boundary, assuming that it is constant. Alternatively, a high signal cuff of known elastic modulus could be used to surround the breast. This would provide an absolute image of shear modulus variations if the boundary contour were chosen inside the cuff.

The 3D shear elasticity reconstructions presented above contain artefacts both inside and outside of the inclusion due to the finite SNR in the measured displacement strain components, and due to the step size used in the finite approximation to the derivatives in the reconstruction. In contrast to the 2D elasticity reconstruction, where the elasticity distribution is reconstructed independently in each plane, the 3D reconstruction uses the elasticity distribution in neighbouring planes. Therefore, in addition to in-plane error propagation problems discussed elsewhere (Skovoroda *et al* 1995a), error propagation in the through-plane direction may occur due to inaccurate elasticity reconstructions in the preceding planes. This is particularly true if the 3D elasticity reconstruction is performed, as in this paper, by solving an initial value problem in the through-plane direction. Even though the more stable integral based approach (Skovoroda *et al* 1999) was employed to solve for $\mu(r)$ in each plane, the results of the 3D elasticity reconstructions in subsequent planes exhibit significant error propagation in the x_3 direction. Given a particular spatial discretization of the displacement data, this error propagation can be reduced by several approaches. These include more appropriate data filtering and reducing the reconstruction's sensitivity to noise, but these considerations are beyond the scope of this paper.

7. Conclusions

The ultimate goal of quantitative elasticity imaging is to provide physicians with a method of remotely palpating soft tissue to detect disease. The three-dimensional elasticity imaging technique demonstrated here is a step toward extending the range and sensitivity of palpation, a powerful diagnostic tool. One possible application of this technique would be measuring the elasticity of breast tissue normally inaccessible to manual palpation. A large elastic modulus difference between normal and pathological breast tissue has been measured *in situ*. A previous study indicates that soft tissues in different physiological states display shear modulus variations of one to two orders of magnitude (Sarvazyan *et al* 1995). If these elastic changes pre-date calcification formation, elasticity imaging may increase sensitivity to and characterization of malignant breast masses, complementing existing diagnostic tools. The relatively high cost of MRI may hinder using this approach as a general screening technique. However, additional work to define the role of this modality as a primary or complementary diagnostic tool in diseases of soft tissues seems worthwhile indeed.

Acknowledgments

References

Adler R, Rubin J M, Bland P and Carson P 1989 Characterization of transmitted motion in fetal lung—quantitative analysis *Med. Phys.* **16** 333–7
Aletras A H, Balaban R S and Wen H 1999a High-resolution strain analysis of the human heart with fast-DENSE *J. Magn. Reson.* **140** 41–57
Aletras A H, Ding S J, Balaban R S and Wen H 1999b DENSE: Displacement encoding with stimulated echoes in cardiac functional MRI *J. Magn. Reson.* **137** 247–52
Axel L and Dougherty L 1989 MR imaging of motion with spatial modulation of magnetization *Radiology* **171** 59–63
Chenevert T L, Skovoroda A R, O'Donnell M and Emelianov S Y 1998 Elasticity reconstructive imaging by means of stimulated echo MRI *Magn. Reson. Med.* **39** 482–90

Chenevert T L, Steele D D, Emelianov S Y and O'Donnell M 1999 *Proc. ISMRM, 7th Scientific Meeting and Exhibition (Philadelphia)* p 263

Dickinson R J and Hill C R 1982 Measurement of soft-tissue motion using correlation between A-scans *Ultrasound Med. Biol.* **8** 263–71

Dresner M A, Rossman P J, Kruse S A and Ehman R L 1999 *Proc. ISMRM, 7th Scientific Meeting and Exhibition (Philadelphia)* p 526

Emelianov S Y, Lubinski M A, Weitzel W F, Wiggins R C, Skovoroda A R and O'Donnell M 1995 Elasticity imaging for the early detection of renal pathology *Ultrasound Med. Biol.* **21** 871–83

Erkamp R Q, Wiggins P, Skovoroda A R, Emelianov S Y and O'Donnell M 1998 Measuring the elastic modulus of small tissue samples *Ultrason. Imaging* **20** 17–28

Foster R S Jr 1996 *Diseases of the Breast* ed J R Harris *et al* (Philadelphia: Lippincott-Raven) pp 133–8

Fowlkes J B, Emelianov S Y, Pipe J G, Skovoroda A R, Adler R S and Carson P L 1995 Magnetic resonance imaging techniques for detection of elasticity variation *Med. Phys.* **22** 1771–8

Fung Y C 1993 *Biomechanics: Mechanical Properties of Living Tissue* (New York: Springer)

Garra B S, Cespedes E I, Ophir J, Spratt S R, Zuurbier R A, Magnant C M and Pennanen M F 1997 Elastography of breast lesions: Initial clincal results *Radiology* **202** 79–86

Goudier J 1933 Concentration of stress around spherical and cylindrical inclusions and flaws *Trans. ASME* **55** 39–44

Hennig J, Nauerth A and Friedburg H 1986 RARE imaging—a fast imaging method for clinical MR *Magn. Reson. Med.* **3** 823–33

Hill D, White V, Jolley D and Mapperson K 1988 Self examination of the breast—is it beneficial—meta-analysis of studies investigating breat self examination and extent of disease in patients with breast cancer *Br. J. Med.* **297** 271–5

Lawrence A J, Rossman P J, Mahowald J L, Manduca A, Hartmann L C and Ehman R L 1999 *Proc. ISMRM, 7th Scientific Meeting and Exhibition (Philadelphia)* p 525

Lerner R M, Huang S R and Parker K J 1990 Sonoelasticity images derived from ultrasound signals in mechanically vibrated tissues *Ultrasound Med. Biol.* **16** 231–9

Mansfield P 1977 Multi-planar image formation using NMR spin echoes *J. Phys. C: Solid State Phys.* **10** L55–L58

Muthupillai R, Lomas D J, Rossman P J, Greenleaf J F, Manduca A and Ehman R L 1995 Magnetic resonance elastography by direct visualization of propagating acoustic strain waves *Science* **269** 1854–7

Newcomb P A, Weiss S, Storer B E, Scholes D and Young B E 1991 Breast self-examination in relation to the occurence of advanced breast cancer *J. Natl. Cancer Inst.* **83** 260–5

O'Donnell M, Skovoroda A R, Shapo B M and Emelianov S Y 1994 Internal displacement and strain imaging using ultrasonic speckle tracking *IEEE Trans. Ultrason. Ferroelectr. Freq. Control* **42** 314–25

Ophir J, Cespedes E I, Ponnekanti H, Yazdi Y and Li X 1991 Elastography—a quantitative method for imaging the elasticity of biological tissues *Ultrason. Imaging* **13** 111–34

Parker K J, Huang S R, Musulin R A and Lerner R M 1990 Tissue response to mechanical vibrations for sonoelasticity *Ultrasound Med. Biol.* **16** 241–6

Parker K J and Lerner R M 1992 Sonoelasticity of organs—shear waves ring a bell *J. Ultrasound Med.* **11** 387–92

Pelc N J, Drangova M, Pelc L R, Zhu Y, Noll D C, Bowman B S and Herfkens R J 1995 Tracking of cyclic motion with phase-contrast cine MR velocity data *J. Magn. Reson. Imaging* **5** 339–45

Plewes D B, Betty I, Urchuk S N and Soutar I 1995 Visualizing tissue compliance with MR imaging *J. Magn. Reson. Imaging* **5** 733–8

Plewes D B, Poole G, Leitch M and Urchuk S N 1996 *Proc. ISMRM, 4th Scientific Meeting and Exhibition (New York)* p 476

Reese T G, Wedeen V J and Weisskoff R M 1996 Measuring diffusion in the presence of material strain *J. Magn. Reson. Ser.* B **112** 253–8

Sarvazyan A P, Skovoroda A R, Emelianov S Y, Fowlkes J B, Pipe J G, Adler R S, Buxton R B and Carson P L 1995 *Acoustical Imaging* vol 21 (New York: Plenum) pp 223–40

Sinkus R, Lorenzen J, Schrader D, Lorenzen M, Dargatz M and Holz D 1999 *Proc. ISMRM, 7th Scientific Meeting and Exhibition (Philadelphia)* p 259

——2000 High-resolution tensor MR elastography for breast tumour detection *Phys. Med. Biol.* **45** 1649–64

Skovoroda A R, Emelianov S Y, Lubinski M A, Sarvazyan A P and O'Donnell M 1994 Theoretical analysis and verification of ultrasound displacement and strain imaging *IEEE Trans. Ultrason. Ferroelectr. Freq. Control* **41** 302–13

Skovoroda A R, Emelianov S Y and O'Donnell M 1995a Tissue elasticity reconstruction based on ultrasonic displacement and strain images *IEEE Trans. Ultrason. Ferroelectr. Freq. Control* **42** 747–65

Skovoroda A R, Klishko A N, Gukasyan D A, Maevsky E I, Ermilova V D, Oranskaya G A and Sarvazyan A P 1995b Quantitative analysis of the mechanical characteristics of pathologically altered soft biological tissues *Biofizika* **40** 1335–40

Skovoroda A R, Lubinski M A, Emelianov S Y and O'Donnell M 1999 Reconstructive elasticity imaging for large deformations *IEEE Trans. Ultrason. Ferroelectr. Freq. Control* **46** 523–35

Steele D D, Chenevert T L, Emelianov S Y and O'Donnell M 1999 *Proc. ISMRM, 7th Scientific Meeting and Exhibition (Philadelphia)* p 1616

Tristam M, Barbosa D C, Cosgrove D O, Bamber J C and Hill C R 1988 Ultrasonic study of *in vivo* kinetic characteristics of human tissues *Ultrasound Med. Biol.* **14** 695–707

Tristam M, Barbosa D C, Cosgrove D O, Nassiri D K, Bamber J C and Hill C R 1986 Application of Fourier analysis to clinical study of patterns of tissue movement *Ultrasound Med. Biol.* **12** 927–37

Van Houten E, Miga M I, Kennedy F E, Weaver J B and Paulsen K D 1999 *Proc. ISMRM, 7th Scientific Meeting and Exhibition (Philadelphia)* p 260

Weaver J B, Van Houten E, Miga M I, Kennedy F E, Hartov A, Poplack S P, Nagy H M and Paulsen K D 1999 *Proc. ISMRM, 7th Scientific Meeting and Exhibition (Philadelphia)* p 1617

Zerhouni E A, Parish D M, Rogers W J, Yang A and Shapiro E P 1988 Human heart: tagging with MR imaging—a method for noninvasive assessment of myocardial motion *Radiology* **169** 164–72

Signal-to-noise considerations in static displacement, stimulated echo NMR elasticity imaging

D. D. Steele[1], T. L. Chenevert[1,2], S. Y. Emelianov[1], and M. O'Donnell[1,3]
Departments of Biomedical Engineering[1], Radiology[2], and Electrical Engineering and Computer Science[3],
The University of Michigan, Ann Arbor, MI

INTRODUCTION

Elasticity imaging may offer clinicians a non-invasive method of remotely palpating patients to detect diseased tissues. Tissue elasticity information may be obtained via NMR detection of shear waves[1] or of static tissue displacement.[2] Here we present simulation results elucidating the effects of displacement sensitivity and applied deformation on the signal-to-noise ratio (SNR) of elasticity images obtained using static displacement, stimulated echo NMRI (SDSEI).

PRINCIPLE

In SDSEI, the object is deformed during the stimulated echo mixing time, TM. Local displacements are encoded by means of a pulsed gradient applied before and after deformation. The sensitivity is given by

$$\vec{\Phi}_d = \gamma \vec{G}_d \tau$$

where the displacement sensitivity, Φ_d, is in radians/distance, G_d is the displacement encoding gradient strength, and τ is the displacement encoding gradient duration. The gradient of the displacement field yields the strain field, and the strain field is used as an input for a boundary value problem to extract the tissue elastic moduli.[3]

SIMULATION

A simple one-dimensional, 100-mm long object is used in all simulations. This object contains an inclusion whose shear modulus is five times larger than the surrounding material's. The pulse sequence assumed is that in the paper by Chenevert *et al.*,[2] with TM = 200 ms, τ = 4.5 ms, and 225 ms between displacement encoding gradients . The NMR resolution is 128 pixels. The base SNR of the material is set to 130, matching the SNR of a tissue-mimicking material measured using the SDSEI pulse sequence.

The variables used are G_d and the normalized applied surface deformation, ε_0. Since τ is assumed constant, Φ_d varies linearly with G_d. G_d ranges from 0 to 5 G/cm in 0.2 G/cm increments, and ε_0 from 1% to 20% in 1% steps. For each gradient-deformation combination, both the NMR image and the elasticity image are reconstructed. The reconstructed elastic moduli are normalized to the background reconstruction. Then the NMR image SNR, SNR_0, and the elasticity image SNR, SNR_E, are calculated. Four different noise instances are averaged for every point.

RESULTS

Figures 1a and 1b show the SNR_0 and the SNR_E, respectively, of the background. Here we see that the SNR_0 decreases with increasing G_d and ε_0 due to intrapixel dephasing. Note that signal loss due to diffusion increases as G_d increases. The SNR_E begins at 0 for $G_d = 0$, and then increases with both deformation and sensitivity until the intrapixel dephasing is π radians. Beyond this point it drops off quickly to zero. Again, diffusion signal loss is present.

Figures 2a and 2b show, respectively, the SNR_0 and the SNR_E of the inclusion. Here the major source of signal loss in SNR_0 is diffusion. Because the inclusion is harder than the background, it tends to displace rather than deform under the applied surface deformation; hence only the gradient contributes significantly to the intrapixel dephasing. The SNR_E simply seems to exhibit diffusion loss and does not peak as the SNR_E of the background does. Also note that the SNR_E of the inclusion is lower than that of the background.

This can be explained by noting that the elasticity reconstruction depends upon the strain field, and the strain is the gradient of the displacement field. As noted above, the hard inclusion tends to displace, not deform, under a certain surface deformation. Thus, not only does the intrapixel dephasing decrease, but the *inter*pixel dephasing (i.e., strain) decreases. Hence the combinations of Φ_d and ε_0 presented here do not approach the optimal strain fields for the inclusion reconstruction.

Fig. 1a: Background SNR_0
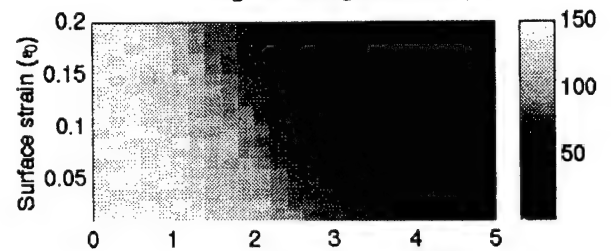
Fig. 1b: Background SNR_E
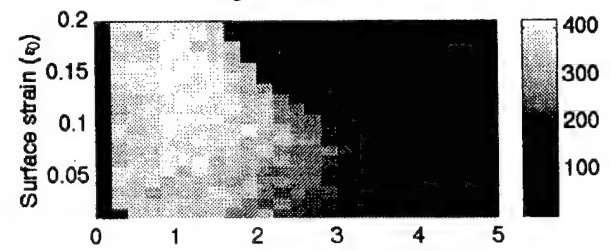
Fig. 2a: Inclusion SNR_0
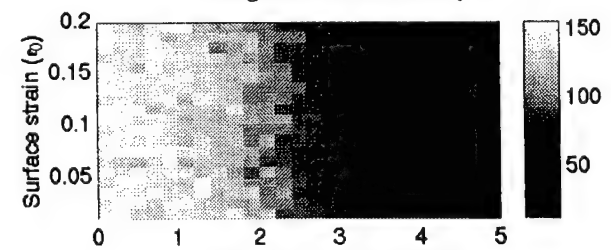
Fig. 2b: Inclusion SNR_E

Encoding gradient (G/cm)
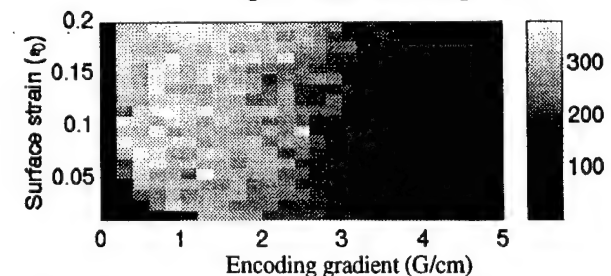
CONCLUSIONS

We have illustrated the effect of displacement sensitivity and applied deformation on static displacement NMR elasticity images and noted the differing optimal imaging parameters for tissues with different shear moduli. These results suggest a type of adaptive elasticity reconstruction wherein the voxel size for a given region of tissue varies inversely with the strain field in order to optimize the elasticity reconstruction's SNR.

REFERENCES

[1] R. Muthupillai *et al.*, *Science* **269,** 1854-1857 (1995).
[2] T. L. Chenevert *et al.*, *Mag. Res. Med.* **39,** 482-90 (1998).
[3] A. Skovoroda *et al.*, *IEEE UFFC* **42,** 747-65 (1995).

Reconstructive Elasticity Imaging for Large Deformations

Andrei R. Skovoroda, Mark A. Lubinski, *Student Member, IEEE*, Stanislav Y. Emelianov, *Member, IEEE*, and Matthew O'Donnell, *Fellow, IEEE*

Abstract—A method is presented to reconstruct the elastic modulus of soft tissue based on ultrasonic displacement and strain images for comparatively large deformations. If the average deformation is too large to be described with a linear elastic model, nonlinear displacement-strain relations must be used and the mechanical equilibrium equations must include high order spatial derivatives of the displacement. Numerical methods were developed to reduce error propagation in reconstruction algorithms, including these higher order derivatives. Problems arising with the methods, as well as results using ultrasound measurements on gel-based, tissue equivalent phantoms, are given. Comparison to reconstructions using a linear elastic model shows that equivalent image quality can be produced with algorithms appropriate for finite amplitude deformations.

I. INTRODUCTION

IMAGES of mechanical displacements and strains within soft tissue present information about the elasticity of internal structures [1]–[21]. Interpreting these images, however, can be difficult for complex mechanical objects such as soft tissue. To potentially simplify image interpretation and reduce artifacts due solely to object geometry, several investigators have explored elastic modulus reconstruction [9], [10], [17], [22]. Exact reconstruction is impossible without detailed knowledge of the mechanical boundary conditions (i.e., the Young's modulus needs to be specified along some boundary, as discussed later in this paper). Nevertheless, methods have been developed to produce relative reconstructions, even if detailed mechanical boundary conditions are unknown [9], [10].

Previous work from our laboratories has shown that the Young's (or equivalently the shear) modulus of soft tissue and tissue-like phantoms can be reconstructed from mechanical displacement and strain images acquired during static external deformation [5]–[10], [12], [18]–[21]. Different imaging systems (e.g., ultrasound and MRI), as well as different deformation procedures, were used to generate displacement and strain images. Consequently, effec-

tive numerical methods were developed for all systems to reconstruct the relative Young's modulus based on a linear elastic model. These techniques do not require any information about global boundary conditions (i.e., mechanical constraint of the body, its geometry, the types of external and internal forces, etc. [9]). In principle, however, they are limited to low magnitude external deformations in which a linear model is valid. Here we extend these methods to finite amplitude deformations.

Large external deformations increase the signal-to-noise ratio (SNR) of displacement and strain images [5]–[10], [23]. Unfortunately, large deformations of soft tissue and tissue-like materials cannot be described with a linear elastic model. A linear model can break down in two ways. First, for most soft tissues, the elastic modulus increases as a function of strain (i.e., strain hardening). This effect is often referred to as "material nonlinearity." Second, a more complete description of the equilibrium equation, including nonlinear strain-displacement relations, must be used for large deformations. This effect is often referred to as "geometric nonlinearity." Due to the high order displacement derivatives resulting from this description, error propagation must be minimized in any reconstruction algorithm using measured displacement data with a finite signal to noise ratio.

In this paper, we examine the second form of nonlinearity, namely, geometric nonlinearities arising from large amplitude deformations. These studies were conducted on gelatin phantoms with almost no material nonlinearities over the deformation range considered here (average strain up to 14%). Material nonlinearities in soft tissue are considered in [24], [25]. The specific purpose of the present study was to explore numerical methods minimizing the effects of higher order displacement derivatives needed to describe finite amplitude deformations on elasticity reconstruction.

Previous algorithms for elasticity reconstruction were formulated using the set of equations describing mechanical equilibrium in a statically deformed, linear elastic medium [5], [9], [10], [18]–[21], [24], [26]. Independent of the specific elastic model, however, these equations can be posed in either differential or integral form. An integral representation is more appropriate for a nonlinear model given realistic measurement noise. As discussed in Section II, numerical methods have been developed for both linear and nonlinear models exploiting an integral representation of the reconstruction equations. The specific approach assumes a plane strain state to approximate two-

dimensional displacement and strain images obtained with a real-time ultrasound scanner. The full three-dimensional problem is discussed in the Appendix.

Displacement data acquired with a real-time ultrasound scanner were used to test the numerical methods of Section II. Relative elastic modulus images were reconstructed within a gel-based, tissue equivalent phantom with prescribed mechanical properties using both linear and nonlinear models. Methods for displacement and strain image acquisition are presented in Section III. All results are presented in Section IV. The paper concludes with a discussion of the results in Section V.

II. Theory

Consider a three-dimensional (3-D) volume V of deformed media with the displacement vector $U = U(x_1, x_2, x_3) = (u_1, u_2, u_3)$ in Cartesian coordinates x_i, $i = 1, 2, 3$. The volume V can be either the entire mechanical body or a region of interest inside the object.

The most general nonlinear mechanical equilibrium equations are [27]–[31].

$$\sum_{j=1}^{2} \left\{ \sum_{n=1}^{3} [\sigma_{nj}(\delta_{in} + u_{i,n})] \right\}_{,j} = 0 \quad i = 1, 2, 3. \quad (1)$$

Here σ_{nj} is a component of the 2nd ranked stress tensor and δ_{in} is the Kronecker delta symbol. In (1), and the rest of this paper, the lower index after a comma means differentiation with respect to the corresponding spatial Lagrangian coordinate. Note that spatial coordinates and displacement components correspond to the initial, not deformed, configuration of the object under investigation. Similarly, all images are presented in the original object geometry (i.e., before deformation).

Equation (1) must be satisfied at every internal point of the body. If the magnitudes of the spatial derivatives of all displacement components are small, the last terms $u_{i,n}$ in (1) can be omitted, producing the familiar linear equilibrium equations [32], [33]:

$$\sum_{j=1}^{3} \sigma_{ij,j} = 0, \quad i = 1, 2, 3. \quad (2)$$

To complete the system of equations describing internal deformations, the relation between stress and strain tensors, as well as the relation between the strain tensor and the displacement vector, are needed. Here we assume that the standard linear relation between the stress tensor σ_{ij} and the strain tensor ε_{ij} for incompressible media is still valid [27]–[34]:

$$\sigma_{ij} = p\delta_{ij} + 2\mu\varepsilon_{ij}, \quad (3)$$

where p is the static, internal pressure and the shear elastic modulus μ is considered a constant independent of the strain magnitude. Computing the spatial distribution of

the shear elastic modulus is the goal of reconstruction. Note in an incompressible material, such as soft tissue, the shear and Young's moduli are simply proportional (i.e., $E = \mu/3$). Thus, shear modulus and Young's modulus reconstructions are equivalent.

In the following derivation we assume a plane strain state in which spatial derivatives of the out-of-plane displacement u_3 are either zero or small compared to the others, and the two in-plane components u_1 and u_2 do not vary significantly as functions of the out-of-plane coordinate [5], [6], [8], [10], [12], [18], [19], [21], [32]. Nonlinear elasticity reconstruction for a general three-dimensional strain state is considered and discussed in the Appendix.

Because the pressure p cannot be directly measured with an imaging system, it must be eliminated from the equations describing mechanical equilibrium [5], [9], [10], [18]–[22], [26]. For the linear case, eliminating p from (2) and (3) leads to a partial differential equation for the unknown shear elasticity distribution $\mu = \mu(x, y)$:

$$(\mu\varepsilon_{xy})_{,xx} - (\mu\varepsilon_{xy})_{,yy} + 2(\mu\varepsilon_{yy})_{,xy} = 0, \quad (4)$$

where the spatial coordinates x_1 and x_2 are denoted here by x and y. Note that the incompressibility condition, $\varepsilon_{11} + \varepsilon_{22} = 0$, is used to produce the specific form presented in (4). All strains in this equation are defined by the linear strain-displacement relation:

$$\varepsilon_{ij}^{\text{lin}} = \frac{1}{2}(u_{i,j} + u_{j,i}). \quad (5)$$

The reconstruction procedure assumes that all relevant displacements are known (i.e., measured), and solves for the shear elasticity distribution satisfying both (4) and the mechanical boundary conditions.

Except for the degenerate (i.e., parabolic) case corresponding to an in-plane translation with rotation of the volume as a rigid body, internal deformations are described by a hyperbolic, 2nd order differential equation [9], [26]. This means there is a unique shear modulus distribution satisfying (4) given appropriate mechanical boundary conditions. Rather than specifying displacement and stress values at the object boundary [17], a much simpler boundary value problem can be formulated using the method of characteristics in which the modulus, and/or spatial derivatives of the modulus are specified solely along a set of characteristic curves (see [35], Chapter 10). For the differential equation given in (4), these curves are defined by all points (x, y) satisfying the following relation:

$$\varepsilon_{xy}dy = \left(\varepsilon_{yy} \pm \sqrt{\varepsilon_{yy}^2 + \varepsilon_{xy}^2}\right) dx. \quad (6)$$

To illustrate how the characteristic curves of (4) help formulate elasticity reconstruction as a simplified boundary value problem, deformation data (i.e., all components of the strain tensor) from an inhomogeneous gel-based tissue equivalent phantom were analyzed. These data were collected using the methods described in Section III. The characteristic curves computed according to (6) over a 25-mm by 65-mm area within the phantom are presented in
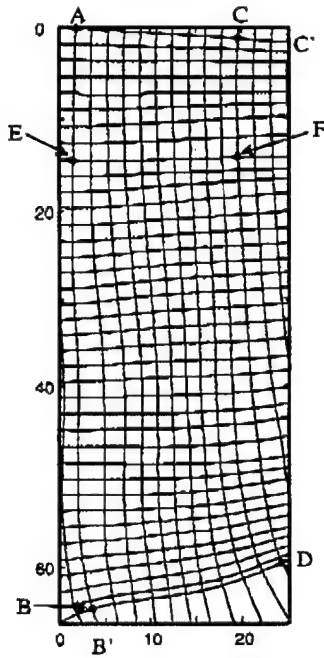
Fig. 1. Characteristic curves of (6) computed from ultrasound measurements on the inhomogeneous gel-based phantom.

Fig. 1. Displayed here are all characteristics starting at the bottom and left side of the region at equal (approximately 1.8 mm) intervals. If, for example, the distribution $\mu(x, y)$ is given along parts AB and AC of two intersecting characteristics AB' and AC', then the reconstruction for region $ABDC$ reduces to a classic Goursat boundary problem for (4). In contrast, to get the unique solution of (4) within the region CEF, the values of μ, $\partial\mu/\partial x$, and $\partial\mu/\partial y$ must be prescribed along the single line CE (see [35], Chapter 10).

In this paper we only consider reconstruction based on two intersecting characteristic curves defining a region of interest (ROI). If the exact value of the elastic modulus is not known along these two curves, reconstruction within the ROI is relative. That is, the reconstructed modulus is normalized to the value along the intersecting characteristics. Because the primary goal of reconstruction is artifact reduction rather than exact quantitation, a relative modulus image is sufficient. As discussed in [9], regions of nearly constant elastic modulus can be identified with edge detection operators acting on strain images.

Using the characteristic curves, numerical methods can be developed to solve (4) given displacement measurements. In practice, however, the problem of elasticity reconstruction is greatly complicated even in the linear case due to noisy displacement measurements (i.e., due to noisy coefficients in (4)) and propagation of this noise through numerical integration within the ROI. Therefore, a specific procedure to integrate (4) across the ROI must be used [5], [8]–[10], [12], [18]–[21].

To produce a more stable reconstruction procedure appropriate for noisy deformation data, substitute (3) into (2) and integrate rather than differentiate. After eliminat-

ing the unknown pressure, the system of equations reduces to an integral equation of the form:

$$\delta(x,y) \equiv 4\left[\varepsilon_{yy}\mu - (\varepsilon_{yy}\mu)|_{x_0} - (\varepsilon_{yy}\mu)|_{x_0,y_0}\right] +$$

$$\int_{y_0}^{y} \left[(\gamma\mu)_{,x} - \{(\gamma\mu)_{,x}\}|_{x_0}\right] dy$$

$$- \int_{x_0}^{x} \left[(\gamma\mu)_{,y} - \{(\gamma\mu)_{,y}\}|_{y_0}\right] dx = 0, \quad (7)$$

where $\gamma = 2\varepsilon_{xy}$ and the notations $f|_{x_0} = f(x_0, y)$ and $f|_{y_0} = f(x, y_0)$ are used in this equation and below.

The integral equation in (7) is expressed as a functional $\delta(x,y)$, as the goal of reconstruction with noisy data will be to force $\delta(x,y)$ to approach zero in some average sense across the ROI. In contrast with (4), this equation does not contain second order derivatives of the strain. Moreover, the shear strain, and spatial derivatives of the shear strain, only appear in the integral terms. Because noisy lateral displacement estimates only contribute to the shear strain, the effects of measurement error will be reduced by the smoothing action of the integral without sacrificing spatial resolution [36]. This type of processing is similar to incompressibility methods in which noisy lateral displacement measurements are smoothed by integrating higher SNR axial strains without losing spatial resolution [37], [38]. Therefore, elasticity reconstruction by (7) should be more stable.

For large deformations, a similar functional must be defined from the general equilibrium equations of (1) and the general Lagrangian strain-displacement relation. Denoting the displacement components u_1 and u_2 by u and v, the unwrapped form of (1) for the plane strain state is:

$$(\sigma_{xx,x} + \sigma_{xy,y})(1 + u_{,x}) + (\sigma_{xx}u_{,xx} + \sigma_{yy}u_{,yy})$$
$$+ (\sigma_{xy,x} + \sigma_{yy,y})u_{,y} + 2\sigma_{xy}u_{,xy} = 0$$
$$(\sigma_{xy,x} + \sigma_{yy,y})(1 + v_{,y}) + (\sigma_{xx}v_{,xx} + \sigma_{yy}v_{,yy})$$
$$+ (\sigma_{xx,x} + \sigma_{xy,y})v_{,x} + 2\sigma_{xy}v_{,xy} = 0. \quad (8)$$

By incorporating the stress-strain relation (3) into (8) and rearranging terms, the following linear system of equations for derivatives of the unknown static internal pressure, $p_{,x}$ and $p_{,y}$, results:

$$A\nabla(p) = -pB - F, \quad (9)$$

where

$$A(x,y) = \begin{pmatrix} 1 + u_{,x} & u_{,y} \\ v_{,x} & 1 + v_{,y} \end{pmatrix}, \quad B(x,y) = (b_i) = \nabla^2 U,$$

$$F = (f_i), \quad i = 1, 2;$$

$$\nabla = (\partial/\partial x, \partial/\partial y), \quad \nabla^2 = \partial^2/\partial x^2 + \partial^2/\partial y^2;$$

$$f_1 = 2[(1 + u_{,x})\psi_1 + u_{,y}\psi_2$$
$$+ (\varepsilon_{xx}u_{,xx} + \varepsilon_{yy}u_{,yy} + 2\varepsilon_{xy}u_{,xy})\mu],$$

$$f_2 = 2[v_{,x}\psi_1 + (1 + v_{,y})\psi_2$$
$$+ (\varepsilon_{xx}v_{,xx} + \varepsilon_{yy}v_{,yy} + 2\varepsilon_{xy}v_{,xy})\mu],$$

$$\psi_1 = (\mu\varepsilon_{xx})_{,x} + (\mu\varepsilon_{xy})_{,y} \quad \psi_2 = (\mu\varepsilon_{xy})_{,x} + (\mu\varepsilon_{yy})_{,y}.$$

These formulas contain the components of the nonlinear Lagrangian strain tensor [27]–[31]:

$$\varepsilon_{ij} = \frac{1}{2}\left(u_{i,j} + u_{j,i} + \sum_k u_{k,i} u_{k,j} \right). \tag{10}$$

For a plane strain state, the strain tensor components take the specific form:

$$\begin{aligned}
\varepsilon_{xx} &= u_{,x} + [(u_{,x})^2 + (v_{,x})^2]/2, \\
\varepsilon_{yy} &= v_{,y} + [(u_{,y})^2 + (v_{,y})^2]/2, \\
\varepsilon_{xy} &= [u_{,y} + v_{,x} + u_{,x}u_{,y} + v_{,x}v_{,y}]/2.
\end{aligned} \tag{11}$$

If the magnitudes of the spatial derivatives of all displacement components are small, the last (nonlinear) term in (10) can be omitted to produce the linear strain tensor of (5).

Again, the unknown pressure must be removed from (9). To do this, we solve (9) with respect to unknowns $p_{,x}$ and $p_{,y}$:

$$\nabla(p) = \alpha p + \beta, \tag{12}$$

where $\alpha(x,y) = (\alpha_i) = -A^{-1}B$, $\beta(x,y) = (\beta_i) = -A^{-1}F$, $i = 1, 2$. Then, integrating the first of these equations along x and the second along y, two simultaneous expressions for the unknown pressure are produced:

$$p(x,y) = \varphi_1\left[p(x_0, y) + \int_{x_0}^x \frac{\beta_1}{\varphi_1} dx \right] \tag{13.1}$$

$$p(x,y) = \varphi_2\left[p(x, y_0) + \int_{y_0}^y \frac{\beta_2}{\varphi_2} dy \right], \tag{13.2}$$

where $\varphi_1(x,y) = \exp\left\{ \int_{x_0}^x \alpha_1(x,y)dx \right\}$ and $\varphi_2(x,y) = \exp\left\{ \int_{y_0}^y \alpha_2(x,y)dy \right\}$ do not depend on $\mu(x,y)$. The term $p(x, y_0)$ in (13.2) can be obtained from (13.1). Similarly, the $p(x_0, y)$ in (13.1) can be obtained from (13.2). Consequently, the set of simultaneous equations describing the unknown pressure reduces to a single equation,

$$\varphi_1 \int_{x_0}^x \frac{\beta_1}{\varphi_1} dx - \varphi_2 \left[\varphi_1 \int_{x_0}^x \frac{\beta_1}{\varphi_1} dx \right]\bigg|_{y_0} - \varphi_2 \int_{y_0}^y \frac{\beta_2}{\varphi_2} dy$$
$$+ \varphi_1 \left[\varphi_2 \int_{y_0}^y \frac{\beta_2}{\varphi_2} dy \right]\bigg|_{x_0} - Gp_0 = 0, \quad (14)$$

where $G(x,y) = [\varphi_2(x,y)\varphi_1(x,y_0) - \varphi_1(x,y)\varphi_2(x_0,y)]$ does not depend on $\mu(x,y)$, and $p_0 = p(x_0, y_0)$.

The expression given in (14) can be used to reconstruct the shear modulus given large deformations. Before defining a functional similar to (7) for the nonlinear case, we consider a simplification of the matrix A^{-1} based on an assumption of incompressibility. The matrix A^{-1} is defined as:

$$A^{-1} = \frac{\begin{pmatrix} 1 + v_{,y} & -u_{,y} \\ -v_{,x} & 1 + u_{,x} \end{pmatrix}}{\det(A)}. \tag{15}$$

The determinant of A is simply related to the metric tensor:

$$\det(A) = 1 + (u_{,x} + v_{,y}) + (u_{,x}v_{,y} - v_{,x}u_{,y}) = \sqrt{g}, \tag{16}$$

where $g = \det(g_{ij})$ is the determinant of the 2nd ranked metric tensor g_{ij}.

The density ρ of a deformed medium is related to the density ρ_0 of the undeformed medium by [29], [37]:

$$\rho = \rho_0 / \sqrt{g}. \tag{17}$$

For incompressible materials $g = 1$, and $\det(A) = 1$. Therefore, (15) reduces to:

$$A^{-1} = \begin{pmatrix} 1 + v_{,y} & -u_{,y} \\ -v_{,x} & 1 + u_{,x} \end{pmatrix}. \tag{18}$$

Substituting (18) into (14) and integrating, we obtain an expression for the reconstruction functional in the nonlinear case, as seen in (19) (top of next page), where

$$\begin{aligned}
\varepsilon &= \varepsilon_{yy} - \varepsilon_{xx}, \quad \gamma = 2\varepsilon_{xy}, \\
g_1 &= 2\{\varepsilon[u_{,yy}(1 + v_{,y}) - v_{,yy}u_{,y}] \\
&\quad + \gamma[u_{,xy}(1 + v_{,y}) - v_{,xy}u_{,y}]\}, \\
g_2 &= 2\{-\varepsilon[v_{,xx}(1 + u_{,x}) - u_{,xx}v_{,x}] \\
&\quad + \gamma[v_{,xy}(1 + u_{,x}) - u_{,xy}v_{,x}]\}.
\end{aligned}$$

In the limit of small displacements, $\alpha = 0$, $\varphi_i = 1$, $i = 1, 2$, $G(x,y) \equiv 0$, and all second order terms in g_i can be ignored. For this case, (19) reduces to (7). Consequently, (19) can be used as the reconstruction functional over a wide range of internal deformations. In contrast to (4), the differential equation for the nonlinear case after eliminating p contains 4th order displacement derivatives. Therefore, an integral representation for the nonlinear case is also much more appropriate given realistic measurement noise.

To evaluate either (7) or (19), spatial derivatives of both the axial and lateral displacement components are needed. It is well known, however, that lateral displacement measurements are much noisier than axial ones if ultrasound is used to track internal deformations [7], [37], [38]. In addition to smoothing from the integral representation of the equilibrium equation, incompressibility processing can be used in both linear and nonlinear cases to further reduce the influence of noisy displacement measurements [37], [38]. All results presented in Section III used lateral displacement estimates obtained from incompressibility processing.

To solve for the unknown shear elasticity distribution $\mu(x,y)$ given all measured displacements and strains

$$\delta(x,y) \equiv 2\left\{\varepsilon\mu - [\varepsilon\mu + (\varepsilon_{xx}\mu)|_{x_0}\varphi_1]\big|_{y_0}\varphi_2 - [\varepsilon\mu - (\varepsilon_{yy}\mu)|_{y_0}\varphi_2]\big|_{x_0}\varphi_1\right\} +$$

$$\left\{\int_{y_0}^{y}[(\gamma\mu)_{,x} + \mu g_2]\varphi_2^{-1}dy\right\}\varphi_2 - \left\{\varphi_2\int_{y_0}^{y}[(\gamma\mu)_{,x} + \mu g_2]\varphi_2^{-1}dy\right\}\bigg|_{x_0}\varphi_1 -$$

$$\left\{\int_{x_0}^{x}[(\gamma\mu)_{,y} + \mu g_1]\varphi_1^{-1}dx\right\}\varphi_1 - \left\{\varphi_1\int_{x_0}^{x}[(\gamma\mu)_{,y} + \mu g_1]\varphi_1^{-1}dx\right\}\bigg|_{y_0}\varphi_2 - Gp_0 = 0, \quad (19)$$

within the ROI, a global minimization procedure was used [5], [8]–[10], [12], [18]–[21]. This numerical technique is general and applies both to linear (7) and nonlinear (19) functionals. For a given distribution $\mu(x,y)$ along the ROI boundaries, the error functional $\delta(x,y)$ must be minimized across the ROI in some general way. Here, the specific distribution $\mu_{ij} = \mu(x_i, y_j)$ is sought which minimizes the total error:

$$D = \left(\int_S \delta^2 ds\right), \qquad (20)$$

where (x_i, y_j), $0 \leq i \leq N$, $0 \leq j \leq M$ is a rectangular grid covering the ROI. The integral is approximated by summing $\delta(x_i, y_i)$ over all grid points.

In discrete form, when differential and integral operators are replaced by discrete-space equivalents, simultaneous minimization of D with respect to all undetermined μ_{ij} yields a set of linear algebraic equations. In theory, therefore, reconstruction is primarily a matrix inversion. In practice, however, the matrix is poorly conditioned; it is very difficult to produce a stable inverse using noisy, experimental data. Alternatively, error minimization can be performed with an iterative approach, as discussed below.

For the nonlinear case, the unknown scalar value $p_0 = p(x_0, y_0)$ in (19) must be estimated prior to general reconstruction. This term is estimated independently by minimizing the error:

$$D_* = \left(\int_{S_*} \delta^2 ds\right) \qquad (21)$$

within a thin region including the ROI boundaries, $x = x_0$ and $y = y_0$, $S_* = (x_0 \leq x \leq x_1, y_0 \leq y \leq y_M) \cup (x_0 \leq x \leq x_N, y_0 \leq y \leq y_1)$, in which the distribution of $\mu(x,y)$ is assumed known given the specified values along the boundaries themselves.

The specific iterative procedure used here to compute the distribution $\mu_{ij} = \mu(x_i, y_j)$ minimizing either (7) or (19) over the ROI is based on a gradient method

$$\mu_{ij}^{k+1} = \mu_{ij}^k - \lambda_{ij}^k \partial D/\partial \mu_{ij}, \qquad (22)$$

where k is the iteration index. It starts with a trial solution $\mu(i,j)$. Then, the error D is minimized by varying the unknown shear modulus μ at only one given grid point (i,j). This procedure is repeated for each (i,j) grid point ([35], Chapter 20). The iterative parameters λ_{ij}^k, which determine the step size of the gradient method, were chosen based on three estimates of D. That is, the minimum of D was locally predicted using a second order polynomial approximation of D as a function of μ_{ij}^k at each grid point under the restriction of a decreasing error [5], [8]–[10], [12], [18]–[21], [35]. Then, a global linear predictor was used to update all λ_{ij}^k simultaneously. This reduced the oscillatory nature of convergence. If the total error remained nearly constant at a given step k based on the global linear predictor values, then the iterative step sizes λ_{ij}^k were again selected separately using the local quadratic predictor as described above. By "ping-ponging" between local and global criteria in this way, large oscillations as a function of iteration index were greatly reduced, thus speeding convergence.

All spatial derivatives in the reconstruction equations were replaced with 2nd order finite differences over the same grid (x_i, y_j). Because 2nd order finite differences use only information from neighboring pixels, error computations were optimized so that for each $\mu_{i_0 j_0}$ update, the error $\delta_{ij} = \delta(x_i, y_j)$ was computed only for $|i - i_0| \leq 1$ or $|j - j_0| \leq 1$. Computations continued until the total error reached a stable plateau $|D^{k+1} - D^k|/D^k < \varepsilon_0$. For all results presented below, a value of $\varepsilon_0 = 10^{-6}$ was used, and a homogeneous medium was the trial solution. It was observed that, with different displacement fields and different grid sizes, the algorithm demonstrates approximately exponential convergence. By decreasing the grid size, the rate of convergence decreased almost linearly. Typical reconstruction times on a low-end SPARC 2 workstation for the results presented below were less than 5 minutes for the nonlinear functional (19), and even less for the linear functional (7). These algorithms, however, can be further optimized for time performance, but this is beyond the scope of this paper.

III. EXPERIMENTAL METHODS AND MATERIALS

All measurements were made with an ultrasound-based deformational imaging system similar to the one presented in [24]. A 38-mm wide, linear array transducer operating at 5 MHz was used for all studies. The array was driven with

an Ultramark-9 (ATL Corp., Bothell, WA) real-time ultrasound system operating in conventional B-scan mode. The digital radio frequency (RF) signal output by the beamformer was captured before subsequent processing and display by the Ultramark-9 back-end. By buffering RF data at the beamformer output for data capture with an external device, live images could be viewed during data capture. About 120 consecutive frames of real-time RF data were stored using a digital data capture system constructed in our lab. At a typical 35 Hz frame rate, this represents almost 4 seconds of phase sensitive ultrasound data that can be used for sensitive speckle tracking.

Measurements were made on two different gel-based phantoms. These phantoms were constructed using the procedures described in [5]–[10]. Both phantoms were 100 mm wide by 140 mm long, where all applied surface deformations were vertical, and the depth direction in the ultrasound imaging plane also was vertical. The first phantom was homogeneous and measured 117 mm in height. The second was 80 mm high and included a single cylindrical hard inclusion near the bottom of the phantom. This inclusion in the inhomogeneous phantom was 18 mm in diameter and was oriented so that the longitudinal axis of the cylinder was perpendicular to both the ultrasound image plane and the direction of the applied surface deformation. The inclusion was constructed from a higher concentration gel. This gel had a shear modulus about 2.5 times larger than the surrounding material as estimated from independent measurements of the elastic modulus using the system described in [25].

Both phantoms were vertically deformed with a 12.5 mm thick Plexiglas plate attached to a manually controlled, one-dimensional motion axis. The plate measured 125 mm by 70 mm in cross section, and almost completely covered the top surface of either phantom. Such a large plate ensured that a plane strain state was reasonably approximated for both phantoms. A hole was cut into the center to mount the imaging array. Once the array was properly secured, the bottom surface of the plate maintained continuous contact with the top surface of the phantom. Deformations were applied by smoothly turning the gear to move the plate vertically over a distance up to 30 mm during the 4 second data capture period. Consequently, very large vertical displacements could be applied during continuous ultrasound data capture.

To test both linear and nonlinear reconstruction procedures over a wide deformational range, two data sets were recorded for each phantom. Internal displacements and strains were imaged in the homogeneous phantom for applied surface displacements of 0.7 mm (0.6% average vertical strain), representing a small deformation, and 7.6 mm (6.5% average vertical strain), representing a fairly large deformation. For the phantom with a single hard inclusion, larger surface displacements were used to produce strains within the hard inclusion comparable to the average strains in the homogeneous phantom. The two data sets recorded on this phantom used a surface displacement of 2.7 mm (3.4% average vertical strain) for the small de-
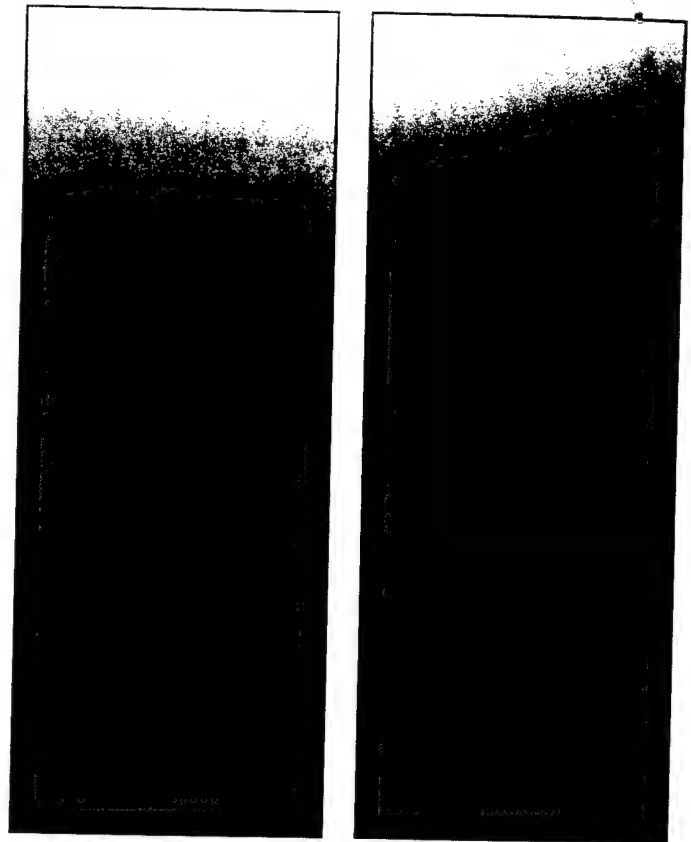

Fig. 2. Measured axial displacement images from the homogeneous phantom (left) and phantom with single hard inclusion at the bottom (right).

formation case, and 12.8 mm (16% average vertical strain) for the large deformation case.

All displacement and strain images were computed from RF ultrasound data using the speckle tracking procedures described in [39], [40]. Based on spatial autocorrelation analysis of the axial, vertical strain image in the homogeneous phantom [39], the spatial resolution of these images was estimated to be about 1.8 mm. Consequently, the grid used for all reconstructions had equal 1.8 mm spacing in both directions (i.e., $\Delta x = \Delta y = 1.8$ mm). The shear modulus was reconstructed in all cases within a 25.1 mm × 66.4 mm rectangular ROI located near the vertical center line of the ultrasound image.

For ultrasound speckle tracking using RF data, lateral displacement estimates exhibit significantly lower SNR than axial (vertical) estimates [38]. To overcome this limitation, incompressibility processing methods have been developed for linear and nonlinear cases [37], [38]. For large deformations, the incompressibility condition is:

$$(1 + v_{,y})u_{,x} - v_{,x}u_{,y} + v_{,y} = 0. \quad (23)$$

As demonstrated in [37], the measured lateral displacement image $u^{\exp}(x, y)$ is used as a reference during lateral displacement computation. For the images presented here, the reference area was a rectangle 10.5-mm wide located near the vertical central line of the ultrasound image. In contrast with [37], where a polynomial approximation of
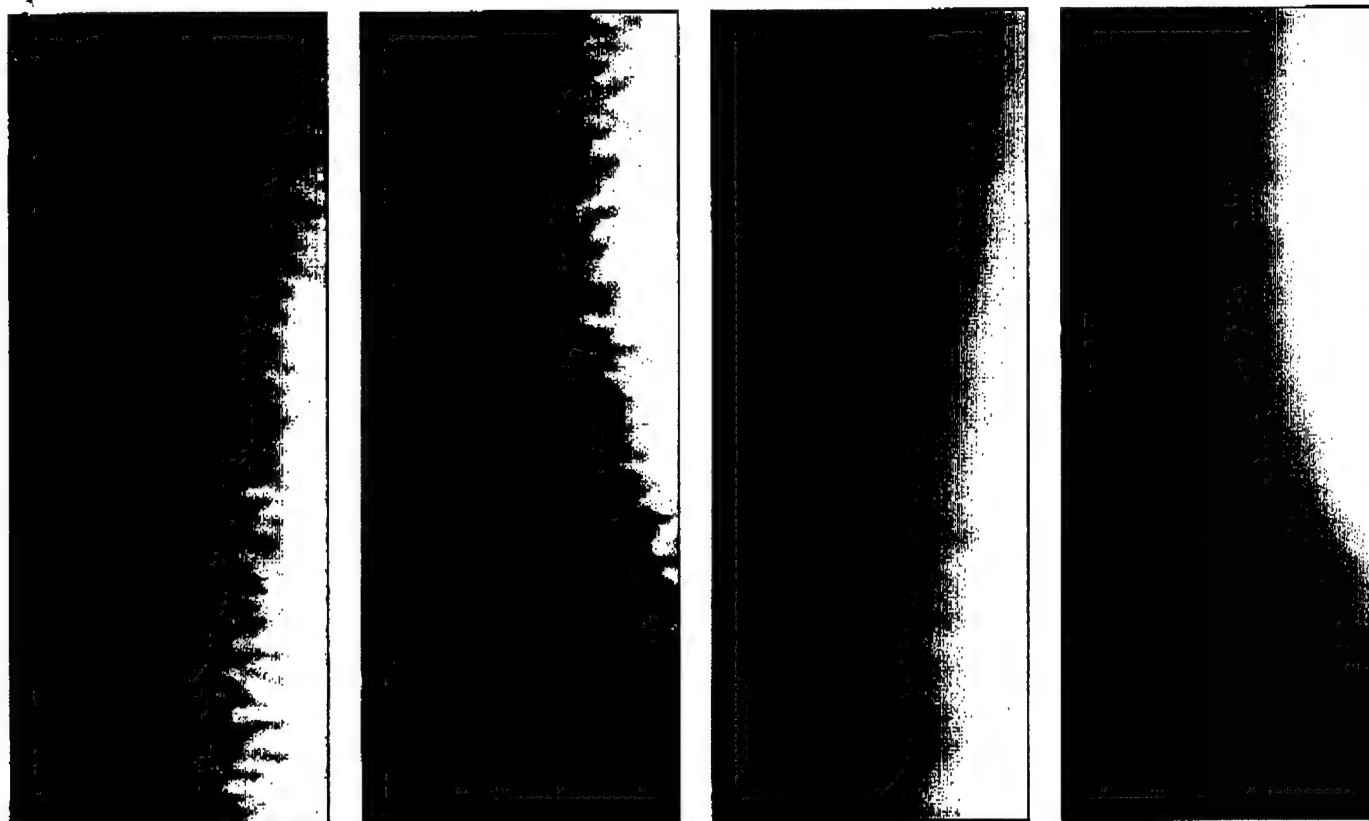
Fig. 3. Measured lateral displacements images for the homogeneous phantom (far left) and the phantom with a single hard inclusion (second from left). Incompressibility processed lateral displacement images for the homogeneous phantom (second from right) and the phantom with a single hard inclusion (far right).

the unknown lateral displacement along an entire single line yielded a solution of (23), a more flexible approach was used here; (23) was solved for a set of particular solutions of the form $u_p(x_0, y) = y^p$, $p = 1, 2, 3$ (i.e., 3rd order) within the region $y_0 - \Delta < y < y_0 + \Delta$ for every interior point (x_0, y_0). Therefore, a set of particular solutions of (23) was obtained within this region, in which the lateral displacement $u(x, y)$ is a linear combination of these particular solutions. The three unknown coefficients defining the linear combination of particular solutions were found by minimizing the total error:

$$\int_{S_R} (u - u^{\mathrm{exp}})^2 ds \qquad (24)$$

across the corresponding area $S_R = (x_s \leq x \leq x_f, y_0 - \Delta < y < y_0 + \Delta)$ of the referenced region.

Prior to reconstruction, both measured axial displacements and incompressibility processed lateral displacements were filtered with a two-dimensional Hamming function, further reducing the spatial resolution of displacement images and subsequent elasticity reconstructions to about 2.5 mm.

IV. RESULTS

Measured vertical (axial) displacement images over the ROI for the large deformation case are presented in Fig. 2

for the homogeneous phantom [Fig. 2(a)] and the inhomogeneous phantom [Fig. 2(b)]. In all these images the transducer, and hence the reference for all displacement measurements, is at the top. Consequently vertical displacements are zero at the top, and motion is toward the transducer (i.e., negative vertical motion). The display dynamic range for Fig. 2(a) is −5.6 mm to −0.4 mm, and for Fig. 2(b) it is −12.6 mm to −1.0 mm. Images of the measured lateral displacement are presented in Fig. 3 under the same conditions for the homogeneous phantom [Fig. 3(a)] and the inhomogeneous phantom [Fig. 3(b)]. The display dynamic range for the homogeneous phantom is −1 mm to 1 mm, and for the inhomogeneous phantom is −1 mm to 4 mm, in which black represents motion to the left and white is motion to the right. (The bottom of the phantom shifted to the right for the inhomogeneous case, and consequently an asymmetric display dynamic range is used.) Using the measured vertical displacements of Fig. 2, the same lateral displacement images after incompressibility processing are presented in Fig. 3(c) for the homogeneous phantom, and Fig. 3(d) for the inhomogeneous phantom.

Images of the shear modulus reconstructed using (7) and (19) are presented in Fig. 4 for the homogeneous phantom. Fig. 4(a) represents the linear reconstruction for the small deformation case, whereas Fig. 4(b) represents the nonlinear reconstruction. Reconstructions for the large deformation case are presented in the lower two panels,
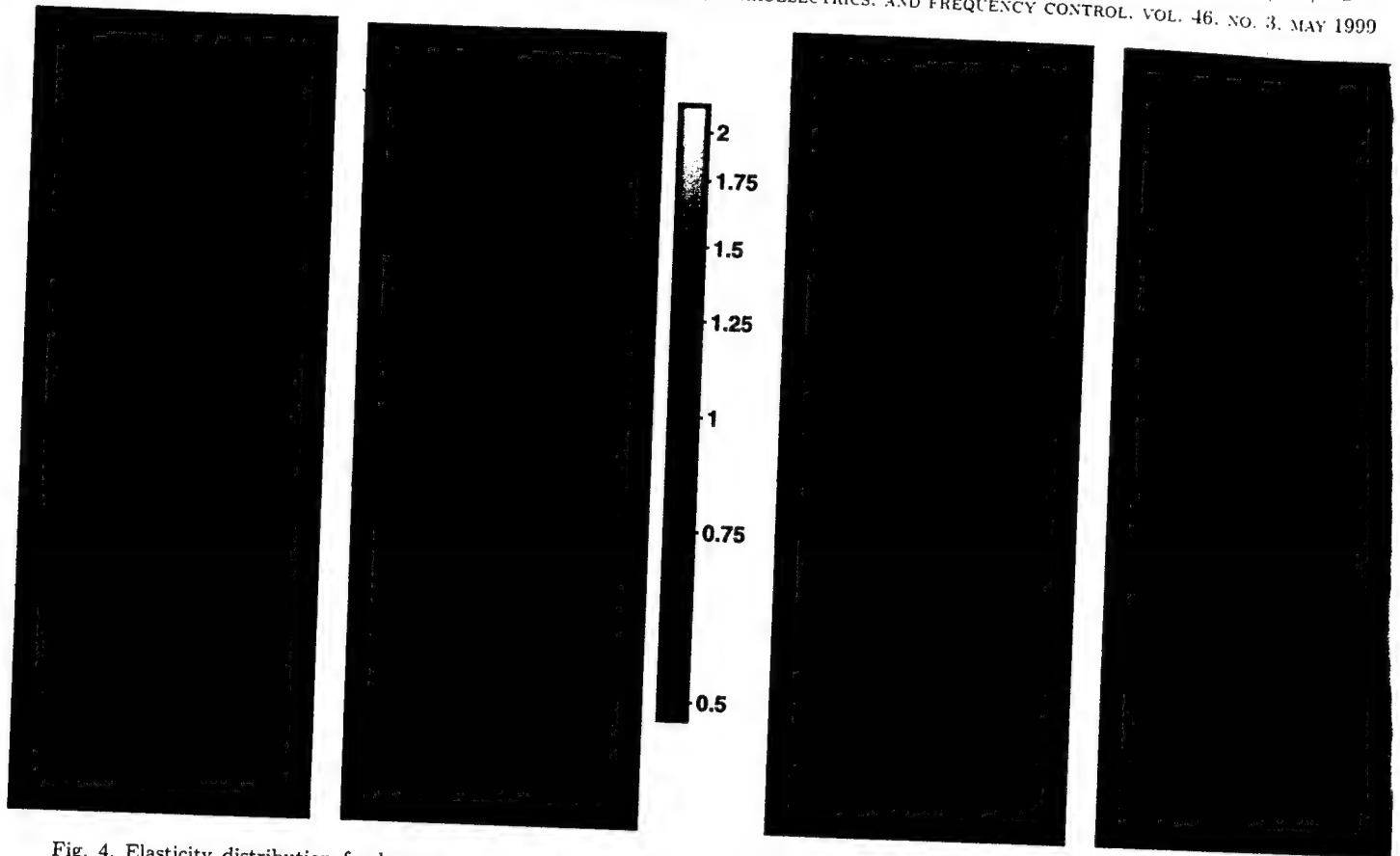
Fig. 4. Elasticity distribution for homogeneous phantom reconstructed by linear processing (far left) and (second from right), and by nonlinear processing (second from left) and (far right). Data from a 0.6% mean vertical deformation were used in (far left) and (second from left). Data from a 6.5% mean vertical deformation were used in (second from right) and (far right).

where Fig. 4(c) is the linear reconstruction and Fig. 4(d) is the nonlinear one. These relative modulus images are presented over a logarithmic gray scale (0.47 to 2.12), as illustrated on the right. The mean value of the normalized (i.e., normalized to the average elastic modulus along the boundaries of the ROI) reconstructed elasticity distribution within the ROI is 1.032 for Fig. 4(a), 1.022 for Fig. 4(c), 0.991 for Fig. 4(b) and 0.996 for Fig. 4(d). The standard deviation is 0.048 and 0.023 for Figs. 4(a) and (c), and 0.033, and 0.019 for Figs. 4(b) and (d), respectively. Artifacts in the nonlinear reconstructions are no greater than those in the linear reconstructions even for small deformations. Horizontal artifacts, created by low SNR lateral displacement measurements, are present in both linear and nonlinear reconstructions. With depth, these artifacts have more energy at lower spatial frequencies (i.e., are broader at the bottom of the image) as the lateral point spread function of the ultrasound system broadens.

Images of the shear modulus reconstructed using (7) and (19) are presented in Fig. 5 for the inhomogeneous phantom. Fig. 5(a) represents the linear reconstruction for the small deformation case, whereas Fig. 5(b) represents the nonlinear reconstruction. Reconstructions for the large deformation case are presented in the lower two panels, where Fig. 5(c) is the linear reconstruction and Fig. 5(d) is the nonlinear one. Exactly the same logarithmic gray scale as Fig. 4 was used here. Again, horizontal artifacts

broaden with depth, becoming especially noticeable at the bottom of these images.

In all reconstructions, the uniform mechanical boundary condition $\mu(x, y) = 1$ was assumed along the edge of the ROI. Because the equilibrium equation is hyperbolic, any errors in this assumption produce noise across the entire reconstruction, where the relative magnitude of this noise (i.e., $|\tilde{\mu} - \mu|/\mu$ with $\tilde{\mu}$ the reconstructed image and μ the true image) is about the same as the magnitude of the boundary condition error. This analysis was confirmed by simulating numerous elasticity reconstructions of a single hard inclusion in an otherwise homogeneous medium, where boundary errors were modeled by a 10-term Fourier series with random coefficients.

The results presented in Figs. 4 and 5 demonstrate that the quality of the image reconstructed with the "geometric" nonlinear model rivals that of the reconstruction based on a linear model, even though high order displacement derivatives are used. Moreover, nonlinear processing provides more consistent elasticity reconstructions even if horizontal streak artifacts are slightly elevated compared to linear processing. To illustrate this, the elasticity distribution reconstructed along the central vertical line of the inhomogeneous phantom is presented in Fig. 6 for linear [Fig. 6(a)] and nonlinear [Fig. 6(b)] models. Clearly, nonlinear processing produces more consistent reconstructions independent of the magnitude of the external deforma-
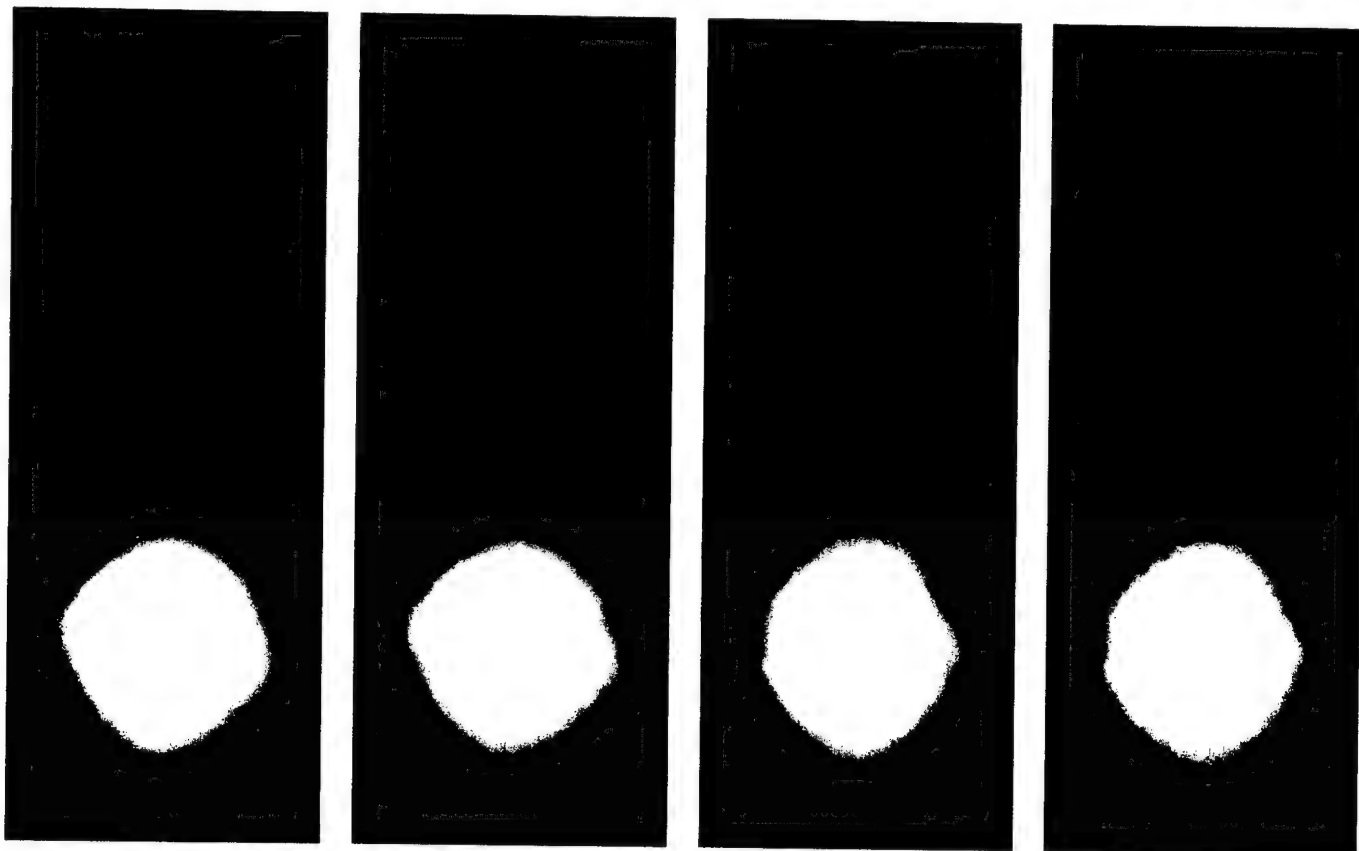
Fig. 5. Elasticity distribution for the phantom with a cylindrical hard inclusion at the bottom reconstructed by linear processing (far left) and (second from right), and nonlinear processing (second from left) and (far right). Displacement images from a 3.4% mean vertical deformation were used in (far left) and (second from left). Displacement images from a 16% mean vertical deformation were used in (second from right) and (far right).

tion. This property holds not only for single line profiles. For the homogeneous phantom, the mean squared difference between small and large deformation images computed over the entire ROI is 0.115 for the linear reconstruction [Figs. 4(a) and (c)] and 0.076 for the nonlinear reconstruction [Figs. 4(b) and (d)]. Similarly, for the inclusion phantom, the mean squared difference between small and large deformation images computed over the top half of the ROI is 0.086, and over the bottom half of the phantom it is 0.181 for the linear reconstruction [Figs. 5(a) and (c)], and 0.071 for the top half of the phantom and 0.152 for the bottom half of the nonlinear reconstruction [Figs. 5(b) and (d)].

V. DISCUSSION

The results of elasticity reconstructions presented above show that a nonlinear (geometric) model can be used to reconstruct the shear (or Young's) elastic modulus based on internal displacement and strain fields computed from real-time ultrasound data. Despite the high order spatial derivatives of both displacement components required for this processing, the image quality of reconstructions based on a nonlinear model rival those based on a simpler, linear model. Moreover, nonlinear processing provides more

consistent results so that elasticity reconstruction can be performed over a wide range of external loading.

The specific numerical methods developed here exploit an integral rather than differential representation of the elasticity equations. Given noisy displacement and strain estimates, this approach is more robust and leads to more stable reconstructions. Moreover, coupled with an iterative procedure using both local and global error predictors to accelerate convergence, it can produce shear modulus images within a few minutes on a low-end, general purpose computer. Future work will optimize software running on more powerful workstations to reduce reconstruction times to a few tens of seconds. Such times are appropriate for clinical applications using real-time ultrasound data capture and specially constructed hardware for speckle tracking.

The fundamental hypothesis of this study is that reconstruction can greatly reduce artifacts in displacement and strain images due to global boundary conditions. To illustrate this point for the specific example discussed here, the results of a simple 1-D elasticity reconstruction are presented in Fig. 7. Fig. 7 shows the normalized distribution of $1/v_{,y}$ for the homogeneous phantom [Fig. 7(a)], and the inhomogeneous phantom [Fig. 7(b)] over precisely the same display dynamic range used in Figs. 4 and 5. Because the homogeneous phantom was constructed to yield a nearly
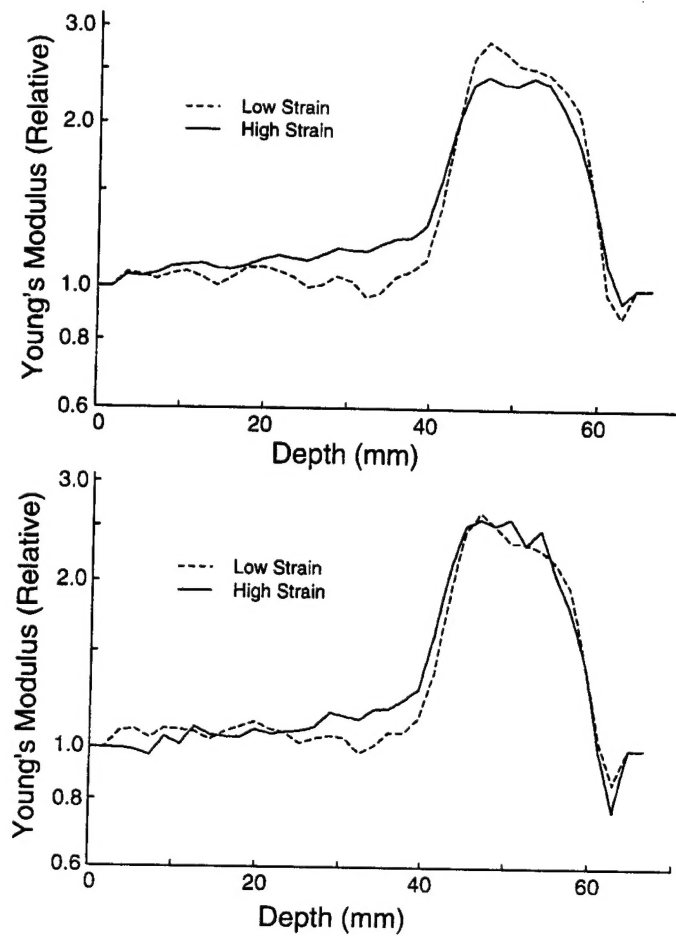
Fig. 6. Elasticity distribution along central vertical line of the inhomogeneous phantom images, reconstructed by linear (left) and nonlinear (right) processing.

Fig. 7. Normalized distribution of $1/v_{,y}$ for the homogeneous phantom (left), and the phantom with a single hard inclusion (right).

uniform strain distribution over the ROI, the 1-D reconstruction is almost perfect. That is, measurement noise is not amplified for this type of processing, leading to a clean reconstruction. In contrast, this simple approach produces significant artifacts in images of an inhomogeneous object. Clearly, as the object becomes more complex, more accurate reconstruction is required even when uniform, one-dimensional loading is used.

All the results presented in this paper were computed assuming a linear stress-strain relation (3). This assumption is almost perfect over a wide deformation range for the gel-based, tissue-like phantoms used here [41]. Real tissue, however, exhibits nonlinear behavior (i.e., material nonlinearity) even for simple types of external loading if the deformation is significant [25], [34], [42]. Because ultrasound data can be acquired over a wide deformation range, there is the possibility that the shear modulus can be reconstructed at different strain magnitudes. Over a limited deformation range, the stress-strain curve can be considered linear, but with an elastic modulus that depends on the instantaneous strain magnitude. Displacement and strain data for an ex vivo model of kidney transplant rejection acquired over a large deformation range have been analyzed with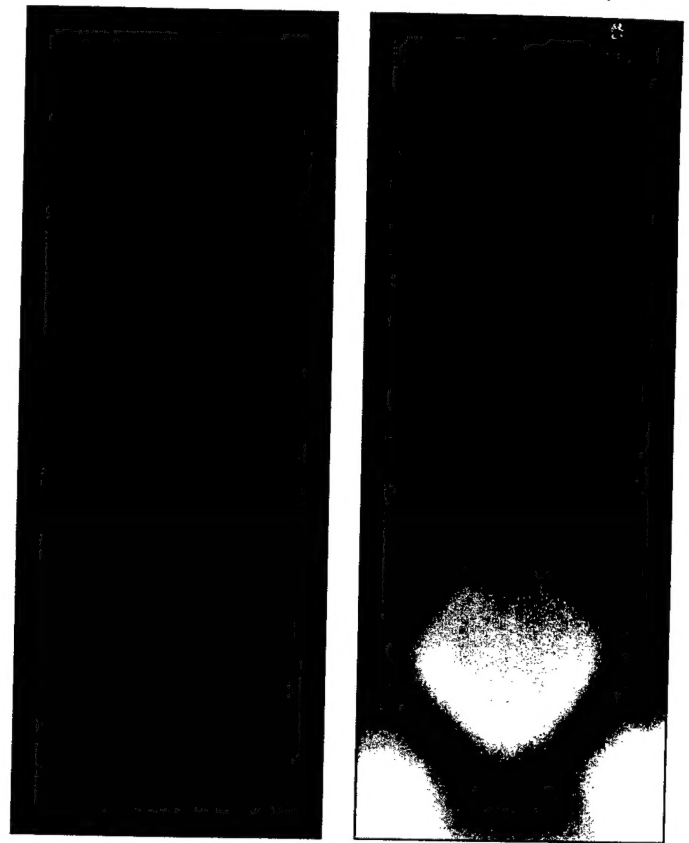 a piecewise linear approximation to produce images related to the material nonlinearity of the kidney [24]. Future work will combine such measurements with the methods developed here to image the nonlinear elastic properties of tissue.

ACKNOWLEDGMENTS

REFERENCES

[1] T. A. Krouskop, D. R. Dougherty, and S. F. Levinson, "A pulsed Doppler ultrasonic system for making non-invasive measurements of the mechanical properties of soft tissue," *J. Rehabil. Res. Dev.*, vol. 24, no. 2, pp. 1–8, 1987.

[2] R. M. Lerner, K. J. Parker, J. Holen, R. Gramiak, and R. C. Waag, "Sono-elasticity: Medical elasticity images derived from ultrasound signals in mechanically vibrated targets," *Acoust. Imaging*, vol. 16, pp. 317–327, 1988.

[3] M. Bertrand, J. Meunier, M. Doucet, and G. Ferland, "Ultrasonic biomechanical strain gauge based on speckle tracking," *Proc. IEEE Ultrason. Symp.*, 1989, pp. 859–864.

[4] J. Ophir, I. Cespedes, H. Ponnekanti, Y. Yazdi, and X. Li, "Elastography: A quantitative method for imaging the elasticity of biological tissues," *Ultrason. Imaging*, vol. 13, pp. 111–134, 1991.

[5] M. O'Donnell, S. Y. Emelianov, A. R. Skovoroda, M. A. Lubinski, W. F. Weitzel, and R. C. Wiggins, "Quantitative elasticity imaging," *Proc. IEEE Ultrason. Symp.*, 1993, pp. 893–903.

[6] A. R. Skovoroda, S. Y. Emelianov, M. A. Lubinski, A. P. Sarvazyan, and M. O'Donnell, "Theoretical analysis and verification of ultrasound displacement and strain imaging," *IEEE Trans. Ultrason., Ferroelect., Freq. Contr.*, vol. 41, pp. 302–313, May 1994.

[7] M. O'Donnell A. R. Skovoroda, B. M. Shapo, and S. Y. Emelianov, "Internal displacement and strain imaging using ultrasonic speckle tracking," *IEEE Trans. Ultrason., Ferroelect., Freq. Contr.*, vol. 41, pp. 314–325, May 1994.

[8] S. Y. Emelianov, M. A. Lubinski, W. F. Weitzel, R. C. Wiggins, A. R. Skovoroda, and M. O'Donnell, "Elasticity imaging for early detection of renal pathologies," *Ultrason. Med. Biol.*, vol. 21, no. 7, pp. 871–883, 1995.

[9] A. R. Skovoroda, S. Y. Emelianov, and M. O'Donnell, "Tissue elasticity reconstruction based on ultrasonic displacement and strain images," *IEEE Trans. Ultrason., Ferroelect., Freq. Contr.*, vol. 42, pp. 747–765, July 1995.

[10] S. Y. Emelianov, A. R. Skovoroda, M. A. Lubinski, and M. O'Donnell, "Reconstructive elasticity imaging," *Acoust. Imaging*, vol. 21, New York: Plenum, 1995, pp. 241–252.

[11] E. I. Cespedes, Y. Huang, J. Ophir, and S. Spratt, "Method for the estimation of subsample time-delays of digitized echo signals," *Ultrason. Imaging*, vol. 17, pp. 142–171, 1995.

[12] J. B. Fowlkes, S. Y. Emelianov, J. G. Pipe, A. R. Skovoroda, R. S. Adler, P. L. Carson, and A. P. Sarvazyan, "Magnetic resonance imaging for detection of elasticity variation," *Med. Phys.*, vol. 22, no. 11, pp. 1771–1778, 1995.

[13] R. Muthupillai, D. J. Lomas, P. J. Rossman, J. F. Greenleaf, A. Manduca, and R. L. Ehman, "Magnetic resonance elastography by direct visualization of propagating acoustic strain waves," *Science*, vol. 269, pp. 1854–1857, 1995.

[14] D. B. Plewes, I. Betty, S. N. Urchuk, and I. Soutar, "Visualizing tissue compliance with MR imaging," *J. Magnetic Resonance Imaging*, vol. 5, pp. 733–738, 1995.

[15] L. Gao, K. J. Parker, R. M. Lerner, and S. F. Levinson, "Imaging of the elastic properties of tissue—A review," *Ultrason. Med. Biol.*, vol. 22, pp. 959–977, 1996.

[16] J. Ophir, I. Cespedes, B. Garra, H. Ponnekanti, Y. Huang, and N. Maklad, "Elastography: Ultrasonic imaging of tissue strain and elastic modulus in vivo," *Eur. J. Ultrasound*, vol. 3, pp. 49–70, 1996.

[17] F. Kallel and M. Bertrand, "Tissue elasticity reconstruction using linear perturbation method," *IEEE Trans. Instrum. Meas.*, vol. 15, no. 3, pp. 299–313, 1996.

[18] T. L. Chenevert, S. Y. Emelianov, and A. R. Skovoroda, "Elasticity reconstructive imaging using static displacement and strain estimation," in *Proc. Int. Soc. Magnetic Resonance in Med.*, pp. 461–462, 1997.

[19] A. R. Skovoroda, M. A. Lubinski, S. Y. Emelianov, and M. O'Donnell, "Nonlinear reconstructive elasticity imaging," *Ultrason. Imaging Tissue Characterization*, June 2–4, 1997, Arlington, VA.

[20] S. Y. Emelianov, T. L. Chenevert, A. R. Skovoroda, M. A. Lubinski, and M. O'Donnell, "Reconstructive elasticity imaging using ultrasound and NMR scanners," *Ultrason. Imaging*, vol. 19, p. 61, 1997.

[21] T. L. Chenevert, A. R. Skovoroda, M. O'Donnell, and S. Y. Emelianov, "Elasticity reconstructive imaging via stimulated echo MRI," *Magnetic Resonance Med.*, vol. 39, no. 3, pp. 482–490, 1998.

[22] C. Sumi, A. Suzuki and K. Nakayama, "Estimation of shear modulus distribution of soft tissue from strain distribution," *IEEE Trans. Biomed. Eng.*, vol. 42, no. 2, pp. 193–202, 1995.

[23] T. Varghese, J. Ophir, and E. I. Cespedes, "Noise reduction in elastography using temporal stretching with multicompression averaging," *Ultrason. Med. Biol.*, vol. 22, pp. 1043–1052, 1996.

[24] S. Y. Emelianov, M. A. Lubinski, A. R. Skovoroda, R. Q. Erkamp, S. F. Leavey, R. C. Wiggins, and M. O'Donnell, "Reconstructive ultrasound elasticity imaging for renal pathology detection," *Proc. IEEE Ultrason. Symp.*, 1997, pp. 1123–1126, Toronto, Canada, Oct. 1997.

[25] R. Q. Erkamp, P. A. Wiggins, A. R. Skovoroda, S. Y. Emelianov, and M. O'Donnell, "Measuring the elastic modulus of small tissue samples," *Ultrason. Imaging*, vol. 20, pp. 17–28, 1998.

[26] A. R. Skovoroda. *Inverse Problems of the Theory of Elasticity in the Diagnostics of Soft Tissue Pathologies*. Pushchino, Russia: Pushchino Research Center of Russian Academy of Sciences, 1992.

[27] J. E. Adkins, "Finite deformation of materials exhibiting curvilinear aeolotropy," *Proc. R. Soc. Lond. Ser. A*, vol. 229, pp. 119–134, 1955.

[28] M. A. Biot, *Mechanics of Incremental Deformations*. New York: Wiley, 1965.

[29] A. A. Ilyushin, *Mechanics of Solid Structures*. Moscow: Moscow State University Press, 1978.

[30] Y. N. Rabotnov, *Mechanics of Solid Structures*. Moscow: Nauka, 1979.

[31] M. E. Gurtin, *An Introduction to Continuum Mechanics*. New York: Academic, 1981.

[32] S. Timoshenko and J. Goodier, *Theory of Elasticity*. New York: McGraw-Hill, 1951.

[33] L. D. Landau and E. M. Lifshitz, *Theory of Elasticity*. Moscow: Nauka, 1965.

[34] F. A. Duck, *Physical Properties of Tissues*. London, England: Harcourt Brace Jovanovich, 1990.

[35] G. A. Korn and M. S. Korn, *Mathematical Handbook for Scientists and Engineers*. New York: McGraw-Hill, 1968.

[36] A. A. Samarskii and E. S. Nikolaev, *Methods of the Solution of the Net Equations*. Moscow: Nauka, 1978.

[37] A. R. Skovoroda, M. A. Lubinski, S. Y. Emelianov, and M. O'Donnell, "Nonlinear estimation of the lateral displacement using tissue incompressibility," *IEEE Trans. Ultrason., Ferroelect., Freq. Contr.*, vol. 45, no. 2, pp. 491–503, 1998.

[38] M. A. Lubinski, S. Y. Emelianov, K. R. Raghavan, A. E. Yagle, A. R. Skovoroda, and M. O'Donnell, "Lateral displacement estimation using tissue incompressibility," *IEEE Trans. Ultrason., Ferroelect., Freq. Contr.*, vol. 43, pp. 247–256, 1996.

[39] N. A. Cohn, S. Y. Emelianov, M. A. Lubinski, and M. O'Donnell, "An elasticity microscope. Part I: Methods," *IEEE Trans. Ultrason., Ferroelect., Freq. Contr.*, vol. 44, pp. 1304–1319, 1997.

[40] M. A. Lubinski, S. Y. Emelianov, and M. O'Donnell, "Speckle tracking methods for ultrasonic elasticity imaging using short time correlation," *IEEE Trans. Ultrason., Ferroelect., Freq. Contr.*, vol. 46, no. 1, pp. 82–96, 1999.

[41] T. J. Hall, M. Bilgen, M. F. Insana, and P. Chaturvedi, "Phantoms for elastography," *Proc. IEEE Ultrason. Symp.*, 1996, pp. 1193–1196.

[42] H. Demiray, "Large deformation analysis of some basic problems in biophysics," *Bull. Mathematical Biol.*, vol. 38, pp. 701–712, 1976.

APPENDIX

Assume that two displacement components are measured with high precision within the volume; also, assume that the third component is estimated less accurately, as, for example, in elasticity measurements using MRI [18], [21].

For a general three-dimensional strain state described by (1) and (3), the following system of equations analogous to (9) is produced:

$$A\nabla(p) = -pB - F, \qquad (A1)$$

where

$$A(x,y) = \begin{pmatrix} 1+u_{1,1} & u_{1,2} & u_{1,3} \\ u_{2,1} & 1+u_{2,2} & u_{2,3} \\ u_{3,1} & u_{3,2} & 1+u_{3,3} \end{pmatrix},$$

$$B(x,y) = (b_i) = \nabla^2 U,$$

$$F = (f_i)$$
$$= 2\left\{ A\Psi + \mu \left[\sum_{i=1}^{3} \varepsilon_{ii} U_{,ii} + \sum_{i,j=1}^{3} (1-\delta_{ij})\varepsilon_{ij} U_{,ij} \right] \right\},$$

$$\Psi = (\psi_i) = (\mu\varepsilon_{1i})_{,1} + (\mu\varepsilon_{2i})_{,2} + (\mu\varepsilon_{3i})_{,3}, \quad i=1,2,3;$$
$$\nabla = (\partial/\partial x_1, \partial/\partial x_2, \partial/\partial x_3),$$
$$\nabla^2 = \partial^2/\partial x_1^2 + \partial^2/\partial x_2^2 + \partial^2/\partial x_3^2.$$

Note that the nonlinear form of the strain tensor (10) must be used.

To solve (A1) with respect to unknowns $\partial p/\partial x_1$, $\partial p/\partial x_2$, and $\partial p/\partial x_3$, we first compute the determinant of matrix A, which is

$$\det(A) = 1 + DivU + \det\begin{pmatrix} u_{,x} & u_{,y} \\ v_{,x} & v_{,y} \end{pmatrix} + \det\begin{pmatrix} v_{,y} & v_{,z} \\ w_{,y} & w_{,z} \end{pmatrix}$$
$$+ \det\begin{pmatrix} u_{,x} & u_{,z} \\ w_{,x} & w_{,z} \end{pmatrix} + \det\begin{pmatrix} u_{,x} & u_{,y} & u_{,z} \\ v_{,x} & v_{,y} & v_{,z} \\ w_{,x} & w_{,y} & w_{,z} \end{pmatrix} = \sqrt{g},$$

where $g = \det(g_{ij})$ is the determinant of the 2nd ranked metric tensor g_{ij}.

Note that for incompressible materials $g = 1$, and, $\det(A) = 1$ which greatly simplifies the inversion of (A1):

$$\nabla(p) = \alpha p + \beta, \tag{A2}$$

where $\alpha(x,y) = (\alpha_i) = -A^{-1}B$, $\beta(x,y) = (\beta_i) = -A^{-1}F$, $i = 1,2,3$.

By integrating each component equation of (A2) along its corresponding coordinate, we obtain:

$$p(x_1,x_2,x_3) = \varphi_1 p(x_1^0, x_2, x_3) + F_1$$
$$= \varphi_2 p(x_1, x_2^0, x_3) + F_2 \tag{A3}$$
$$= \varphi_3 p(x_1, x_2, x_3^0) + F_3$$

where

$$\varphi_i(x_1,x_2,x_3) = \exp\left[\int_{x_i^0}^{x_i} \alpha_i(x_1,x_2,x_3) dx_i \right],$$

$$F_i(x_1,x_2,x_3) = \left(\int_{x_i^0}^{x_i} \frac{\beta_i}{\varphi_i} dx_i \right)\varphi_i, \quad i=1,2,3.$$

Using a procedure paralleling that used to produce (14),

the three-dimensional case reduces to:

$$[(\varphi_2\varphi_3|_{x_2^0} + \varphi_3\varphi_2|_{x_3^0})p_0 + (\varphi_2 F_3|_{x_2^0} + \varphi_3 F_2|_{x_3^0})$$
$$+ (F_2 + F_3)]|_{x_1^0}\varphi_1 + 2F_1 =$$
$$[(\varphi_1\varphi_3|_{x_1^0} + \varphi_3\varphi_1|_{x_3^0})p_0 + (\varphi_1 F_3|_{x_1^0} + \varphi_3 F_1|_{x_3^0})$$
$$+ (F_1 + F_3)]|_{x_2^0}\varphi_2 + 2F_2 = \tag{A4}$$
$$[(\varphi_1\varphi_2|_{x_1^0} + \varphi_2\varphi_1|_{x_2^0})p_0 + (\varphi_1 F_2|_{x_1^0} + \varphi_2 F_1|_{x_2^0})$$
$$+ (F_1 + F_2)]|_{x_3^0}\varphi_3 + 2F_3,$$

where $p_0 = p(x_1^0, x_2^0, x_3^0)$. For a plane strain state (A4) reduces to (14).

Again, in the limit of small displacements, $\alpha = 0$, $\varphi_i = 1$, $i = 1,2,3$, (A4) can be greatly simplified:

$$(F_3|_{x_2^0} + F_2|_{x_3^0} + F_2 + F_3)|_{x_1^0} + 2F_1 =$$
$$(F_3|_{x_1^0} + F_1|_{x_3^0} + F_1 + F_3)|_{x_2^0} + 2F_2 =$$
$$(F_2|_{x_1^0} + F_1|_{x_2^0} + F_1 + F_2)|_{x_3^0} + 2F_3, \tag{A5}$$

where

$$F_1 = 2\left\{ (\mu\varepsilon_{11})|_{x_1^0} - \mu\varepsilon_{11} - \int_{x_1^0}^{x_1} [(\mu\varepsilon_{12})_{,2} - (\mu\varepsilon_{13})_{,3}]dx_1 \right\},$$

$$F_2 = 2\left\{ (\mu\varepsilon_{22})|_{x_2^0} - \mu\varepsilon_{22} - \int_{x_2^0}^{x_2} [(\mu\varepsilon_{12})_{,1} - (\mu\varepsilon_{23})_{,3}]dx_2 \right\},$$

$$F_3 = 2\left\{ (\mu\varepsilon_{33})|_{x_3^0} - \mu\varepsilon_{33} - \int_{x_3^0}^{x_3} [(\mu\varepsilon_{13})_{,1} - (\mu\varepsilon_{23})_{,2}]dx_3 \right\}.$$

Equations (A4) and (A5) do not contain high order spatial displacement derivatives, compared with their equivalent differential equations, and therefore, elasticity reconstruction by (A4) and (A5) should be more stable. Again, (A4) and (A5) show that spatial derivatives of all displacement components are needed in general for elasticity reconstruction in both linear and nonlinear cases, but any one of the three displacement components can be reconstructed using incompressibility processing based on the relation $(\det(A) = 1)$ [37].

Andrei R. Skovoroda received the B.S. and M.S. degrees in mathematics and mechanics in 1973 and 1975, respectively, from the Novosibirsk State University, USSR, and the Ph.D. degree in 1985 from the Moscow State University, USSR.

From 1975 to 1977 he was a lecturer in theoretical mechanics at the College of Textile Technology, Barnaul, USSR. From 1977 to 1980 he was a Ph.D. researcher at the subfaculty of Plasticity of the Moscow State University, where he worked on the dynamic behavior of plates under blast-type loading. In 1981 he held an appointment as a junior research associate at the Laboratory of Mathematical Modeling of the Research Computing Center of the USSR Academy

of Sciences (the present name: Institute of Mathematical Problems of Biology, Russian Academy of Sciences), where he developed efficient mathematical methods to solve the differential equations of the theory of elasticity. In 1986 he became a senior research associate and was scientific secretary at the same institute from 1988 to 1993. He is currently head of the Laboratory of Mathematical Problems in Biomechanics and works on the biomechanics of soft tissue.

Dr. Skovoroda has authored and co-authored more than 80 articles for archival publications and papers presented at all-union and international meetings.

Mark A. Lubinski (S'94) received the B.S. degree in electrical engineering (with biomedical engineering option) in 1990 from Carnegie Mellon University and the M.S. in bioengineering and electrical engineering (systems) in 1993 and 1994, respectively, from the University of Michigan, Ann Arbor.

Before beginning his graduate work, he worked as a computer engineer in the Department of Neurophysiology at the Children's Hospital of Pittsburgh. While at the University of Michigan he was a National Science Foundation Graduate Fellow in Bioengineering and a GAANN Fellow. He is currently a graduate student research assistant at the University of Michigan, working in the Biomedical Ultrasonics Laboratory, pursuing a Ph.D. in biomedical engineering, and researching ultrasonic elasticity imaging. He is a member of Tau Beta Pi and Eta Kappa Nu. His research interests include signal processing, medical imaging, and motion estimation.

Stanislav Y. Emelianov (M'94) was born in May 1966. He received the B.S. and M.S. degrees in physics in 1986 and 1989, respectively, from Moscow State University, and the Institute of Mathematical Problems of Biology of the Russian Academy of Sciences, Russia.

In 1989, he joined the Institute of Mathematical Problems of Biology, where he was engaged in both mathematical modeling of soft tissue biomechanics and experimental studies of noninvasive methods in medical diagnostics based on tissue elasticity variations. Following his graduate work, he moved to the University of Michigan, Ann Arbor, as a post-doctoral fellow in the Electrical Engineering and Computer Science Department working on applications of imaging systems for medical diagnosis and nondestructive testing. Dr. Emelianov is currently a research scientist in the Biomedical Ultrasonics Laboratory at the University of Michigan and involved primarily in the theoretical and practical aspects of ultrasound elasticity imaging. He is the author of several scientific papers. His research interests are in the areas of tissue biomechanics, medical imaging systems, and nondestructive material testing.

Matthew O'Donnell (M'79–SM'84–F'93) received the B.S. and Ph.D. degrees in physics from the University of Notre Dame, Notre Dame, IN, 1972 and 1976, respectively.

Following his graduate work, he moved to Washington University in St. Louis as a postdoctoral fellow in the Physics Department working on applications of ultrasonics to medicine and non-destructive testing. He subsequently held a joint appointment as a Senior Research Associate in the Physics Department and a Research Instructor of Medicine in the Department of Medicine at Washington University. In 1980 he moved to General Electric Corporate Research and Development in Schenectady, New York, where he continued to work on medical electronics, including NMR and ultrasound imaging systems. During the 1984–1985 academic year, he was a visiting fellow in the Department of Electrical Engineering at Yale University investigating automated image analysis systems. Most recently, he has worked on the application of advanced VLSI circuits to medical imaging systems, including catheter arrays. In a bold move during 1990, Dr. O'Donnell moved to the Electrical Engineering & Computer Science Department at the University of Michigan in Ann Arbor, Michigan, where he is currently a Professor.

Dr. O'Donnell is a member of Sigma Xi, the American Physical Society, and is a fellow of both the IEEE and the AIMBE. He has authored or coauthored over 100 archival publications, including 2 receiving best paper awards, numerous presentations at national meetings, and 40 patents.